

APPLIED
COMPUTATIONAL
ELECTROMAGNETICS
SOCIETY
JOURNAL

March 1998
Vol. 13 No. 1

ISSN 1054-4887

DISTRIBUTION STATEMENT A

Approved for public release;
Distribution Unlimited

19980709 083

GENERAL PURPOSE AND SCOPE. The Applied Computational Electromagnetics Society Journal hereinafter known as the **ACES Journal** is devoted to the exchange of information in computational electromagnetics, to the advancement of the state-of-the-art, and to the promotion of related technical activities. A primary objective of the information exchange is the elimination of the need to "re-invent the wheel" to solve a previously-solved computational problem in electrical engineering, physics, or related fields of study. The technical activities promoted by this publication include code validation, performance analysis, and input/output standardization; code or technique optimization and error minimization; innovations in solution technique or in data input/output; identification of new applications for electromagnetics modeling codes and techniques; integration of computational electromagnetics techniques with new computer architectures; and correlation of computational parameters with physical mechanisms.

SUBMISSIONS. The **ACES Journal** welcomes original, previously unpublished papers, relating to **applied computational electromagnetics**.

Typical papers will represent the computational electromagnetics aspects of research in electrical engineering, physics, or related disciplines. However, papers which represent research in **applied computational electromagnetics** itself are equally acceptable.

Contributions may be sent to the Editors in Chief, Dr. Ahmed Kishk or Dr. Allen Glisson
Department of EE
University of Mississippi
University, MS, 38677 USA
Phone: 601-232-5385 (Ahmed)
Phone: 601-232-5353 (Allen)
Fax: 601-232-7231
email:ahmed@olemiss.edu
email:aglisson@mail.olemiss.edu. See "Information for Authors" on the back cover.

SUBSCRIPTIONS. All members of the Applied Computational Electromagnetics Society (**ACES**) who have paid their subscription fees are entitled to receive the **ACES Journal** with a minimum of three issues per calendar year.

Visit us on line at: www.emclab.umn.edu/aces

Back issues, when available, are \$15.00 each. Subscriptions to **ACES**, orders for back issues of the **ACES Journal** and changes of addresses should be sent to:

Dr. Richard W. Adler
ACES Executive Officer
ECE Department, Code ECAB
Naval Postgraduate School
833 Dyer Road, Room 437
Monterey, CA 93943-5121 USA

Allow four week's advance notice for change of address. Claims for missing issues will not be honored because of insufficient notice or address change or loss in mail unless the secretary is notified within 60 days for USA and Canadian subscribers or 90 days for subscribers in other countries, from the last day of the month of publication. For information regarding reprints of individual papers or other materials, see "Information for Authors".

LIABILITY. Neither ACES or the **ACES Journal** editors are responsible for any consequence of misinformation or claims, express or implied, in any published material in an **ACES Journal** issue. This also applies to advertising, for which only camera-ready copies are accepted. Authors are responsible for information contained in their papers. If any material submitted for publication includes material which has already been published elsewhere, it is the author's responsibility to obtain written permission to reproduce such material.

APPLIED
COMPUTATIONAL
ELECTROMAGNETICS
SOCIETY
Journal

March 1998
Vol. 13 No. 1

ISSN 1054-4887

The ACES Journal is abstracted in INSPEC, in Engineering Index, and in DTIC.

The second, third, fourth, and fifth illustrations on the front cover have been obtained from Lawrence Livermore National laboratory.

The first illustration on the front cover has been obtained from FLUX2D software, CEDRAT S.S. France, MAGSOFT Corporation, New York.

THE APPLIED COMPUTATIONAL ELECTROMAGNETICS SOCIETY

JOURNAL EDITORS

EDITOR-IN-CHIEF/ACES

W. Perry Wheless, Jr.
University of Alabama, EE Dept.
PO Box 870286
Tuscaloosa, AL 35487-0286 USA

ASSOC. EDITOR-IN-CHIEF/JOURNAL

Adalbert Konrad
University of Toronto
Toronto, ON, CANADA M5S 1A4

Ruediger Anders
Applied EM Engineering
Roswell, GA, USA

Brian A. Austin
University of Liverpool
Liverpool, UK

Joao Bastos
University Fed De Santa Catarina
Florianopolis, BRAZIL

John Beggs
Mississippi State University
Mississippi State, MS, USA

Fulvio Bessi
Ingegneria dei Sistemi S.p.A.
Pisa, ITALY

Robert Bevensee
Box 812
Alamo, CA, USA

John R. Bowler
University of Surrey
Surrey, UK

John Brauer
Ansoft Corporation
Milwaukee, WI, USA

Tony Fleming
Telecom Australia.
Clayton, Victoria, AUSTRALIA

Pat Foster
Microwave & Antenna Systems
Gt. Malvern, Worc. UK

Allen Glisson
University of Mississippi
University, MS, USA

Gregory R. Haack
DSTO
Salisbury, SA, AUSTRALIA

EDITOR-IN-CHIEF/JOURNAL

Duncan C. Baker
EE Dept. University of Pretoria
0002 Pretoria, SOUTH AFRICA

EDITOR-IN-CHIEF, EMERITUS

Robert M. Bevensee
Box 812
Alamo, CA, 94507-0516 USA

Christian Hafner
Swiss Federal Inst. of Technology
Zurich, SWITZERLAND

Kueichien C. Hill
Wright Laboratory
Wright-Patterson AFB, OH, USA

Todd H. Hubing
University of Missouri-Rolla
Rolla, MO, USA

Nathan Ida
The University of Akron
Akron, OH, USA

Ahmed Kishk
University of Mississippi
University, MS, USA

Andrzej Krawczyk
Institute of Electrical Engineering
Warszawa, POLAND

Peter Krylstedt
National Defence Research Est.
Sundbyberg, SWEDEN

Stanley Kubina
Concordia University
Montreal, Quebec, CANADA

Ronald Marhefka
Ohio State University
Columbus, OH, USA

Gerard Meunier
NPG/ENSIEG
St. Martin-d'Heres Cedex, FRANCE

Edmund K. Miller
LASL
Santa Fe, NM, USA

Giorgio Molinari
University of Genova
Genova, ITALY

MANAGING EDITOR

Richard W. Adler
833 Dyer Rd. Room 437
Naval Postgraduate School Code EC/AB
Monterey, CA 93943-5121 USA

EDITOR-IN-CHIEF, EMERITUS

David E. Stein
USAF Scientific Advisory Board
Washington, DC 20330 USA

Frederic A. Molinet
Societe Mothesim
Plessis-Robinson, FRANCE

Gerrit Mur
Technische Universiteit Delft
Delft, NETHERLANDS

Krishna Naishadham
Wright State University
Dayton, OH, USA

Antonio Orlandi
University of L'Aquila
L'Aquila, ITALY

Giuseppe Pelosi
University of Florence
Florence, ITALY

Andrew F. Peterson
Georgia Institute of Technology
Atlanta, GA, USA

Kurt Richter
Technical University of Graz, IGTE
Graz, AUSTRIA

Harold A. Sabbagh
Sabbagh Associates
Bloomington, IN, USA

Neil R.S. Simons
Communications Research Center
Ottawa, Ontario, CANADA

Norio Takahashi
Okayama University
Tsushima, JAPAN

Yoshiki Uchikawa
Nagoya University
Nagoya, JAPAN

Jean-Claude Verite
Electricite de France
Clamart, Cedex, FRANCE

THE APPLIED COMPUTATIONAL ELECTROMAGNETICS SOCIETY

JOURNAL

Vol. 13 No. 1

March 1998

TABLE OF CONTENTS

"Iterative Solution of Multiple Right Hand Side Matrix Equations for Frequency Domain Monostatic Radar Cross Section Calculations"	
M.D. Pocock and S.P. Walker	4
"A FDTD Surface Impedance Boundary Condition Using Z-Transforms"	
J.H. Beggs	14
"Shipboard HFDF System Simulation"	
J.B. Knorr	25
"Hybrid MoM/SBR Method to Compute Scattering from a Slot Array Antenna in a Complex Geometry"	
A.D. Greenwood and J-M. Jin	43
"Effects of Gaps Among Panels in Radio Astronomy Reflector Antennas"	
G. Pelosi, R. Coccioli and A. Gaggelli	52
"Some Experiences in Using NEC2 to Simulate Radiation from Slots on Cylinders"	
S.H.H. Lim, H.E. Green and C.E. Brander	58
"A Kirchhoff Integral Approach for Decimetric Radiowave Propagation in Urban Areas"	
L. Pisani, F. Rapetti and C. Vittoli	63
"On the Bounded Part of the Kernel in the Cylindrical Antenna Integral Equation"	
M.P. Ramachandran	71
Letter from the Editor: Duncan Baker	78
Announcements:	
Institutional Membership	81
Copyright Form	83
Application for ACES Membership and Newsletter and Journal Subscription	85
Advertising Rates	86
Copy Information - Deadline for Submission of Articles	86

© 1998, The Applied Computational Electromagnetics Society

Iterative solution of multiple right hand side matrix equations for frequency domain monostatic radar cross section calculations

M D Pocock, S P Walker

Computational Mechanics, Imperial College of Science Technology and Medicine, London SW7 2BX
s.p.walker@ic.ac.uk

Abstract

Monostatic rcs characterisation using integral equation methods in the frequency domain requires the solution of very large matrix equations with multiple right hand sides. Although costly for a single right hand side, direct methods are attractive in that subsequent right hand sides are very cheap. Iterative methods are much cheaper for a single right hand side, but if the whole solution must be repeated for each, they become much more expensive. We investigate here the performance of a simple modification to the GCR algorithm, which allows solutions for an essentially unlimited number of right hand sides to be obtained for a modest multiple of the cost of the first. For the cases investigated, with up to 360 right hand sides on bodies up to 15 wavelengths long, with matrices up to 20,440 by 20,440 in size, this multiple was below ~ 10 . Costs seem to rise with the number of right hand sides till the surface field is in some sense characterised, and thereafter subsequent illumination angles are essentially free. An investigation of cost scaling on a set of spheres, ranging from ~ 1 to 7 wavelengths in diameter, seems to indicate the cost of full monostatic characterisation to scale with about the fifth power of frequency.

1. Introduction

There are two main cost components in the solution of large scattering problems, such as rcs evaluation, via frequency domain integral equation methods. The first¹, scaling with frequency f to the fourth power, is the cost of formation of the dense matrix describing interactions between parts of the scatterer. The second is the cost of solving the resulting matrix equation.

For the direct solution schemes most usually employed, this solution cost scales with N^3 , where N is the order of the matrix equation, or equivalently with f^6 . For all but small problems matrix solution is thus the dominant cost. Because of this large cost, there has been increasing attention paid of late to the use of iterative methods for

matrix solution²⁻⁸. It is generally concluded from such studies that iterative schemes require much less time to compute, often by an order of magnitude or more, than would be taken to solve the same system by direct methods. Cost reduction by a large multiple is obviously welcome; even more so would be if that multiple itself increased with problem size, corresponding to a reduction in cost scaling below the f^6 of the direct approach. This has indeed been suggested⁷, but the evidence is as yet inconclusive⁸.

For practical radar cross section analyses, it is necessary to determine the scattered field caused by fields incident from a (large) number of directions. Direct solution methods are then attractive. Once the f^6 cost of matrix factorisation has been paid, solutions for large numbers of incident waves (right hand side vectors in matrix equation terms) can each be found at a cost scaling with f^4 . Even if the required number of right hand sides scales with the second power of frequency, the overall cost of a full monostatic evaluation still only(!) scales with frequency to the sixth power.

This interest in multiple illumination angles is a discouragement to the use of iterative methods. One approach using them is simply to start the solution afresh for each right hand side. Naturally, if more than a few right hand sides are required, any cost saving over the direct approach is lost. If the required number of right hand sides scales with the second power of frequency, the overall cost then scales with something approaching f^8 .

We present here methods which seem able to provide iterative solutions for additional monostatic illumination angles (right hand sides) at essentially no cost, once sufficient right hand sides have been analysed to characterise, in some sense, the surface field.

There have been a few attempts to address this multiple right hand side issue for iterative solutions, which we will discuss prior to describing the present approach.

In general the quality of the initial guess has only a modest affect on the number of iterations required for convergence of an iterative method^{2,4,7}. Consequently, the approach of using the solution from one incident wave as the starting point for the next offers little benefit.

For the sparse matrices resulting from a finite element discretisation, Smith and colleagues⁶ effectively expanded several solutions in terms of a single set of search vectors, with some success.

In a very recent paper⁹ Boyse and Seidl use the GMRES algorithm (and see references cited in Boyse for more details of the block GMRES and the multiple right hand side variant thereof). In essence the problem is first solved simultaneously for a modest number of right hand sides, distributed uniformly over the span of right hand sides of eventual interest, using a block GMRES approach. Whilst this costs more than for a single right hand side, it is not a large multiple of the cost. Intermediate values are then found, using the orthonormal basis for the Krylov sub-space which was found during the solution for the initial right hand sides. It was found necessary to ensure that the number of right hand sides solved for initially was carefully chosen. This number of right hand sides was noted as needing to be sufficient to represent in some sense the RCS distribution sought. An angular separation such as to allow rather more than two samples per wavelength was suggested. If this is not observed, intermediate solutions found subsequently tended to have significant errors. Too many initial right hand sides, however, caused slow convergence of the block GMRES solution. Overall, significant reduction in time relative to a direct solution was observed.

The GCR (generalised conjugate residual) algorithm¹⁰ was used by Soudais⁵ for solving the matrix equations resulting from analysis of scattering from a ~ 1 wavelength mixed dielectric-perfect conductor target. A finite element and symmetric Stratton-Chu treatment were combined, giving a matrix system which was symmetric, and sparse in the finite element regions. Multiple right hand sides were tackled by what seemed to be a very effective, and attractively simple, modification to the normal GCR algorithm. As with most iterative methods, the solution is changed at each iteration by moving a particular distance (the step length) in some direction (the search direction). The computationally expensive part of the algorithm is the finding of this search

direction. In the modified algorithm, the search direction is found for only that right hand side currently exhibiting the largest residual. The solutions to all right hand sides are advanced in this direction, but for a different (and optimal) step length in that direction for each.

In the sections which follow we will extend the application of this approach, to the dense and unsymmetric matrices which result from a normal integral equation discretisation, and to analysing scattering from multi-wavelength 'stealthy' targets. A major aspect of interest will be the interaction of the number of iterations required (a measure of the computational work), with the number of right hand sides analysed, and the body size in wavelengths. It is this latter which determines the 'jaggedness' with angle of the monostatic radar cross section, and consequently the number of illumination angles required to characterise it. If the number of iterations continues to rise in proportion to the number of illumination angles, till the point that the response is fully characterised, there may be no reduction in cost scaling; if otherwise, there could be.

In the next section we will summarise the integral equation formulation, and outline the normal GCR algorithm, and the modification to handle multiple right hand sides. Section three will present results from its application to a number of rcs problems.

2. Formulation

The formulation is well known, and only a brief description will be given here. The MFIE for scattering from a smooth, closed perfect conductor is

$$\frac{1}{2} \mathbf{H}(\mathbf{r}) = \mathbf{H}^{inc}(\mathbf{r}) + \frac{1}{4\pi} \int_{\partial\Omega} [\mathbf{n}' \times \mathbf{H}(\mathbf{r}')] \times \mathbf{R} \left(jk - \frac{1}{R} \right) \frac{e^{jkR}}{R^2} ds' \quad (1)$$

where the integrations to obtain the field at surface location \mathbf{r} are over the rest of the surface of the scatterer s' and \mathbf{r}' , with \mathbf{n} the unit normal, and \mathbf{R} the vector $\mathbf{r} - \mathbf{r}'$. The incident wave is \mathbf{H}^{inc} . We employ a curvilinear, isoparametric discretisation, with Gaussian quadrature. Fuller details are given elsewhere¹¹; the result is a (complex) matrix equation of the form:

$$[\mathbf{A}]\mathbf{H} = \mathbf{H}^{inc} \quad (2)$$

This is to be solved with tens or possibly hundreds of incident wave vectors \mathbf{H}^{inc} .

We use the unpreconditioned GCR algorithm, which we first outline in its normal 'single right hand side' form.

To solve

$$\mathbf{Ax} = \mathbf{b} \quad (3)$$

Initialise:

$$\mathbf{x}^{(0)} = \mathbf{0}$$

$$\mathbf{r}^{(0)} = -\mathbf{b} \quad (4)$$

$$\mathbf{p}^{(0)} = -\mathbf{r}^{(0)}$$

For each iteration k , for $k = 0, \dots$:

Calculate the step length α :

$$\alpha^{(k)} = -\frac{\langle \mathbf{r}^{(k)}, \mathbf{Ap}^{(k)} \rangle}{\|\mathbf{Ap}^{(k)}\|^2} \quad (5)$$

Increment the solution vector

$$\mathbf{x}^{(k+1)} = \mathbf{x}^{(k)} + \alpha^{(k)} \mathbf{p}^{(k)} \quad (6)$$

and residual vector:

$$\mathbf{r}^{(k+1)} = \mathbf{r}^{(k)} + \alpha^{(k)} \mathbf{Ap}^{(k)} \quad (7)$$

Check if converged sufficiently: stop if

$$\frac{\|\mathbf{r}^{(k+1)}\|}{\|\mathbf{r}^{(k)}\|} \leq 10^{-m} \quad (8)$$

with m typically in the range 2 to 8.

If not, calculate search direction vector and matrix vector product for the next iteration:

$$\sigma_i^{(k+1)} = \frac{\langle \mathbf{Ar}^{(k+1)}, \mathbf{Ap}^{(i)} \rangle}{\|\mathbf{Ap}^{(i)}\|^2} \text{ for } i = 1, \dots, k \quad (9)$$

$$\mathbf{p}^{(k+1)} = -\mathbf{r}^{(k+1)} + \sum_{i=1}^k \sigma_i^{(k+1)} \mathbf{p}^{(i)} \quad (10)$$

$$\mathbf{Ap}^{(k+1)} = -\mathbf{Ar}^{(k+1)} + \sum_{i=1}^k \sigma_i^{(k+1)} \mathbf{Ap}^{(i)} \quad (11)$$

As well as the main system matrix, we see that the sets of vectors $\mathbf{p}^{(k)}$ and $\mathbf{Ap}^{(k)}$ must be stored.

The modifications required to solve for multiple right hand sides are very simple. In the initialisation stage a residual and initial search direction is obtained for each right hand side.

At equation (5) a step length is calculated for each right hand side, and the solution and residual vectors incremented. Between (7) and (8) the largest (normalised) residual is found, by searching through the residuals associated with all right hand sides.

Assuming it fails the test (8), a single search direction is calculated in (9) and (10), to suit that right hand side found to have the largest residual. This step, involving matrix vector multiplication, is the one where the principal computation lies. A different step length for each right hand side is then calculated in (5), which is used with the common search direction to increment each solution in (6). We see that at each iteration the parameters selected most suit that right hand side currently furthest from solution. As a result that right hand side improves rapidly, with some other right hand side then taking its place as the current worst. Thus are all right hand sides shepherded to solution more or less in step.

Each right hand side is seen to increase by one the number of vector-vector manipulations required at each iteration (multiplications in equation (5)), and vector-vector additions in equations (6), (7) and (8)). Storage is increased by the need to store the evolving solution and residual for each right hand side. For problems of practical interest, these increases are a modest fraction of the requirements for a single right hand side. As the solutions are attained, it would be possible to continue to iterate only for those whose residual is not yet below the specified tolerance. Although this would save some cost, the saving would be small, and the refinement has not been implemented.

3. Demonstrations

In the sections which follow we present results of the analysis of targets illuminated by many different incident waves. Of particular interest will be the variation of the total number of iterations with the number of illumination angles, and, for practical purposes, the variation of the rcs over that range of illumination angles. Does the

number of iterations rise with illumination angles as long as 'new' information is being gained?

3.1 Equatorial scans

We consider first a monostatic equatorial scan of the NASA almond¹², illuminated at 7 GHz, making it ~ 6 wavelengths long. Discretisation employed an average nodal separation of about $1/9$ of a wavelength, and throughout a termination residual of 10^{-4} was employed. This is a value recently suggested¹³ as appropriate for this discretisation, for the curvilinear isoparametric modelling employed.

Figure 1 shows the variation in the number of iterations required with the number of illumination angles. The monostatic scan was computed as a single run, with respectively 1, 5, 10, ... up to 180 illumination angles (right hand sides) in turn. Cases were studied with these illumination angles distributed uniformly over 180° , 90° , 45° and 15° , forming the lines shown on the figure.

We see that in each case the number of iterations required initially rises with the number of illumination angles examined. For the 180° case, this rise is essentially complete some time before ~ 30 illumination angles, by when about six times as many iterations are required as are required for a single illumination angle. By this point we are gaining ~ 30 solutions for a multiple of ~ 6 in the work required. From then on solutions for additional angles are obtained without further iterations; the maximum 180 considered are similarly gained with this same multiple of ~ 6 over the cost of one. (As discussed in section 2 above, there is still some modest angle-dependent cost, in the vector manipulations of (5) - (8). This is very small in practice, and will be neglected in subsequent discussion.) Similar comments can be made about cases with the illumination angles distributed over a smaller range. As the extent is reduced, in each case the 'plateau' in iterations occurs at a lower number of iterations, and after fewer illumination angles. For example, for a 15° degree range, the plateau in number of iterations is reached after about 10 illumination angles compared to the ~ 30 of the 180° case. This is consistent with the number of iterations being a function of the amount of information being sought; reducing the range reduces the amount.

There is an interesting parallel here with the observations of Boyes and Seidl⁹. Using their very different approach, they found costs to rise

essentially linearly with number of illumination angles till the response was partially characterised, and that subsequent illumination angles were essentially free.

However, the response in that reference was considered primarily in terms of rcs, although the actual unknown for which we are solving a set of equations is the surface field. The monostatic rcs, the quantity actually sought, and the surface field at any particular surface location, are very different functions of incident illumination angle. The (monostatic) rcs generally is a much less smooth a function of incident illumination angle than is the surface field. (For simple geometries it can of course be much more smooth, as the case of the monostatic rcs of a multi-wavelength sphere attests.)

We find some empirical evidence that the plateau is reached when the density of illumination angles is such as to represent reasonably the variation of surface field with illumination angle. In figure 2 is shown an indication of the variation of surface field with illumination angle for the six wavelength almond, by selecting a node (at -4.1° , 0, 0) and component (the real part of the y component) at random. The locations of 30 uniformly spaced illumination angles are marked on this figure, and it could be argued that results from only this many illumination angles provide a reasonably good representation of the surface field variation.

The corresponding rcs is shown in figure 3, with the solid line obtained by illumination from 180 angles, and the 30 locations again marked. (This present paper is not concerned with characterisation of an rcs code, but for completeness this figure also shows the measured rcs¹², albeit with the measured values obtained from an enlarged photocopy of the published measurements. As is seen, agreement of the computed values with this is good.) We see that much of the detailed structure of the rcs is not revealed by using only these 30 angles; lobes on the RCS plot are generally seen to be significantly narrower than on that of the surface field. However, with the 30 illumination angles corresponding to the start of the plateau, this detail is obtained essentially free. (We have not investigated the point, but this might be interesting to consider in the context of the 'monostatic - bistatic approximation'¹⁴. Here relatively widely separated illumination angles can be used to provide a good approximation to the finely sampled monostatic response. It may indeed be that similar criteria apply.)

Timings may be of interest. On a Dec Alpha 600 workstation, the matrix took about 16 minutes to form, and 25 minutes to solve for each illumination, giving a total time of 75 hours for a 180 illumination angle characterisation. Using the multiple right hand side approach, these same 180 solutions were obtained in about 3 hours.

As a further example, figure 4 (inset) shows the monostatic rcs of a 11:1 cylindrical dipole, with hemispherical end caps, discretised with 3026 nodes, and illuminated such as to make it ~ 15 wavelengths long. This figure was drawn from results evaluated with 360 illumination angles 0.5° apart, and shows approximately 60 distinct peaks over the 180° . It is not shown, but the variation of surface field with illumination angle is not surprisingly very much smoother than the rcs on this 15 wavelength body; indeed it is very smooth for many surface locations, with ~ 15 peaks being the maximum found. Figure 4 shows the variation of the number of iterations with the number of illumination angles. Again, we see a distinct plateau occurring, here after ~ 90 illumination angles. This is sufficient to represent reasonably the surface field variation, but not to characterise the equatorial rcs variation. Here the full equatorial monostatic result, employing 360 illumination angles, is obtained for ~ 4 times the cost of a single iterative solution. For this size of matrix, 6052 by 6052 (complex), we generally find a single iterative solution to cost rather more than an order of magnitude less than a single direct solution.

3.2 Near head-on rcs

Whilst it is conventional to analyse equatorial sweeps as above, practical interest may probably be concentrated on a relatively small solid angle centred around head-on, possibly biased towards illumination from slightly below. We have analysed this same 6 wavelength almond, with illumination in the range 0 to 16° vertically and 0 to 16° horizontally from head-on (where symmetry naturally makes only this one quadrant necessary). A uniform increment in each angular coordinate was used, with computations made with 16 by 16 (256) illumination angles, 8 by 8, 4 by 4, 3 by 3 and 1 (head on) illumination angle. The inset in figure 5 shows a representation of the rcs, plotted from the 256 illumination angle result. Figure 5 shows the variation in the number of iterations with the number of illumination angles, again exhibiting the characteristic 'plateau', here at about 7 times the

number of iterations required for a single illumination angle.

3.3 Cost scaling

As noted earlier, there is no clear evidence regarding cost scaling for single illumination angle (single right hand side) solutions via iterative methods. The position is naturally made more complicated once multiple illumination angles are included. We can present here some empirical evidence, but only tentative observations and conclusions can be drawn.

As discussed elsewhere⁸, fineness of discretisation (expressed in terms of degrees of freedom per incident wavelength) itself can influence the number of iterations required. We will here employ spherical scatterers of a range of sizes, as uniform discretisation is difficult to ensure on (say) the almond.

Whilst obviously it is machine dependant, some actual times might be helpful. All jobs were run on a 96Mb SGI Indy R5000. The matrix for the biggest mesh, 20440 (single precision complex) \times 20440 in size, occupied 3.2 Gb. This was formed once, and read in for each iteration. Each such iteration took ~ 10 minutes, of which almost half was reading from disk. At the plateau of figure 6, mentioned below, some 680 iterations were required, corresponding to a time of 110 hours for the full characterisation.

We plot in figure 6 the number of iterations required versus illumination angles for a 180° scan of a series of spheres. These range in size from 1.6 wavelengths in diameter (1060 by 1060 matrix) to 7.12 wavelengths (20440 by 20440 matrix). They display behaviour qualitatively identical to that of the almond, with a flat plateau in number of iterations required being reached after only a modest number of illumination angles. Here, though, the monostatic rcs is of course characterised fully by a single illumination, whereas the computed surface field distribution is dependant on the illumination angle, lending further evidence to the observation that it is the latter which is the determinant of computational work.

In figure 7 we plot the variation of the number of iterations required at this plateau versus the diameter of the sphere in wavelengths. This number of iterations for full characterisation seems to rise roughly linearly with problem size. As the matrix size varies with the square of the body size or frequency, the cost of each iteration scales with

the fourth power of frequency, giving a total cost scaling in this particular case with about the fifth power of frequency.

4. Discussion and Conclusions

A very simple modification of the GCR approach has been shown to be effective for analysis of multiple right hand sides for the large, dense and unsymmetric matrices of multi-wavelength monostatic rcs calculations.

It seems possible to obtain solutions for a large number of different illumination angles for a modest multiple of the cost for a single right hand side. Typically, for the cases examined, this multiple is $\sim < 10$ for an essentially unlimited number of illumination angles.

As noted, the cost scaling of iterative solutions for single look angles is unclear. Starting from this point, we conclude from the present study:

- Costs for multiple look angles are independent of the number of look angles once more than some threshold number of look angles is considered.
- This threshold seems to be related to the number required to characterise the surface field, not the number required to characterise the rcs.
- How the number required to characterise the surface field varies with frequency is obviously geometry-dependant.
- On many geometries (eg the almond studied) the surface field needs far fewer angles to characterise it than does the rcs.
- The net result is that, for a body where this is true, monostatic rcs characterisation can be obtained for a small fraction of the cost of repeated *ab initio* iterative solution of the matrix equation.

References

1. Miller, E.K. A selective survey of computational electromagnetics. *IEEE Transactions on Antennas and Propagation* 36:pp1281-1305, (1988).
2. Peterson, A.F. and Mittra, R. Method of Conjugate Gradients for the Numerical Solution of Large-body Electromagnetic Scattering problems. *J.Opt.Soc.Am.* 2:pp971-977, (1985).
3. Peterson, A.F. and Mittra, R. Convergence of the Conjugate Gradient Method when Applied to Matrix Equations Representing Electromagnetic Scattering Problems. *IEEE Transactions on Antennas and Propagation* 34:pp1447-1453, (1986).
4. Smith, C.F., Peterson, A.F. and Mittra, R. The Biconjugate Gradient Method for Electromagnetic Scattering. *IEEE Transactions on Antennas and Propagation* 38:pp938-940, (1990).
5. Soudais, P. Iterative solution of a 3-D scattering problem from arbitrary shaped multielectric and multiconducting bodies. *IEEE Transactions on Antennas and Propagation* 42:pp954-959, (1994).
6. Smith, C.F., Peterson, A.F. and Mittra, R. The Treatment of Multiple excitations by Iterative methods for problems of Electromagnetic Scattering. *IEEE A-P Soc, Proc Int Symp Dig Blackburg, VA* pp530-533, (1987).
7. Woodworth, M.B. and Yaghjian, A.D. Multiwavelength three dimensional scattering with dual surface integral equations. *Journal of the Optical Society of America A* 11:pp1399-1413, (1994).
8. Pocock, M.D. and Walker, S.P. The complex biconjugate gradient solver applied to large electromagnetic scattering problems; computational costs, and cost scalings. *IEEE Transactions on Antennas and Propagation* 45:pp140-146, (1997).
9. Boyse, W.E. and Seidl, A.A. Mono-Static RCS Computation with a Block GMRES Iterative Solver. *Applied Computational Electromagnetics Society Journal* 11:pp63-69, (1996).
10. Eisenstat, S.C., Elman, H.C. and Schultz, M.H. Variational iteration methods for non symmetric systems of linear equations. *SIAM Journal of Numerical Analysis* 20:pp345-357, (1983).
11. Pocock, M.D. and Walker, S.P. Radar cross section prediction using boundary integral equation methods with isoparametric quadratic surface modelling and iterative solvers. *Electromagnetics* 16:pp651-669, (1996).
12. Woo, A.C., Wang, H.T.G. and Schuh, M.J. Benchmark radar targets for the validation of computational electromagnetics programs. *IEEE Antennas and Propagation Magazine* 35:pp84-89, (1993).
13. Walker, S.P. and Lee, B.H. Termination criteria in iterative solution of large scattering problems using integral equation methods. *Comm in Numerical Methods in Engng* 13:pp199-206, (1997).
14. Schuh, A. and Woo, A. The Monostatic - bistatic rcs approximation. *IEEE Antennas and Propagation Magazine* 36:pp76-80, (1994).

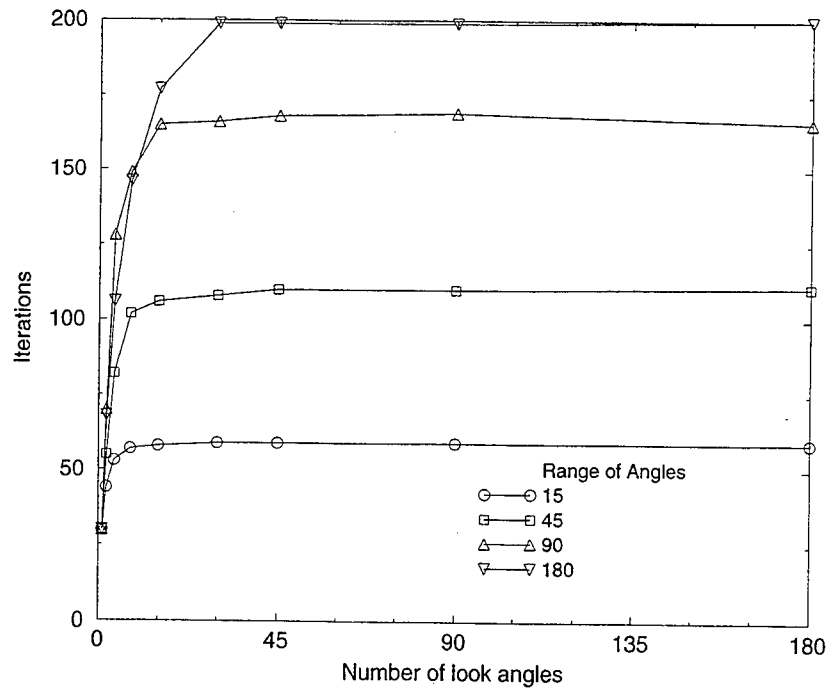


Figure 1

NASA almond, 7 GHz (6 wavelengths long); Iterations required versus number of illumination angles, with angular range spanned by the illumination angles, measured from head-on, as a parameter.

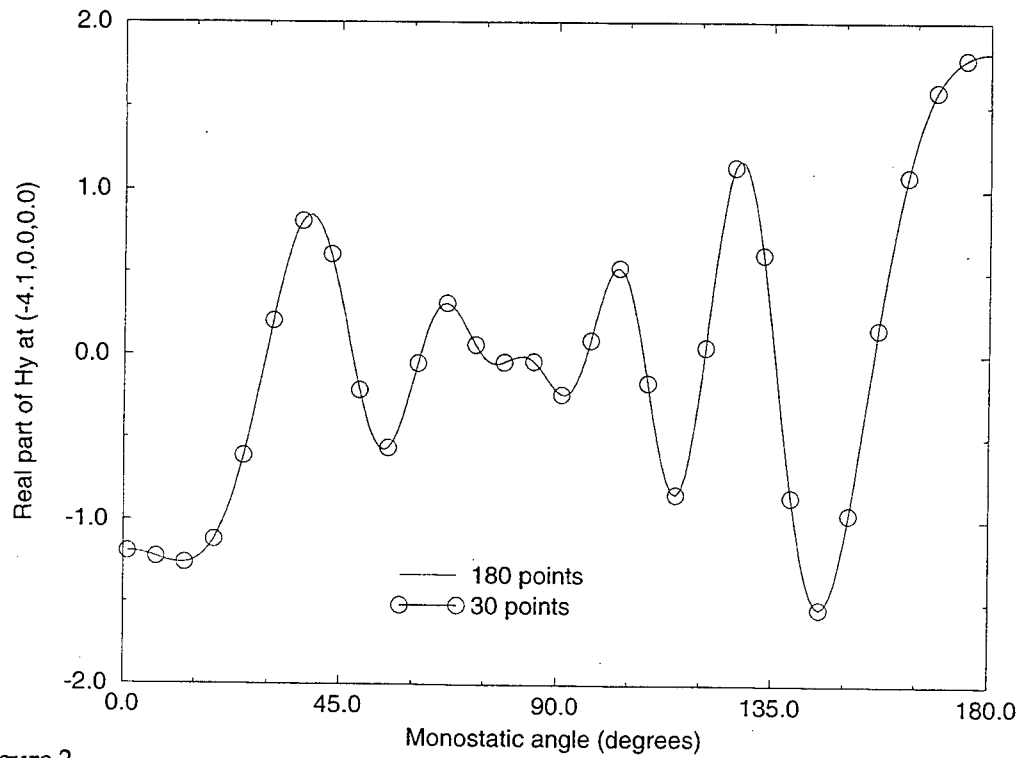


Figure 2

NASA almond (7 GHz, 6 wavelengths long): Real part of y -component of surface \mathbf{H} field at surface location $(-4.1'', 0, 0)$ as a function of monostatic incident illumination angle. The illumination ranges from 0 to 180° in the equatorial (VV) plane (solid line), with results every 6 degrees (30 uniformly spaced illumination angles) additionally marked by circles.

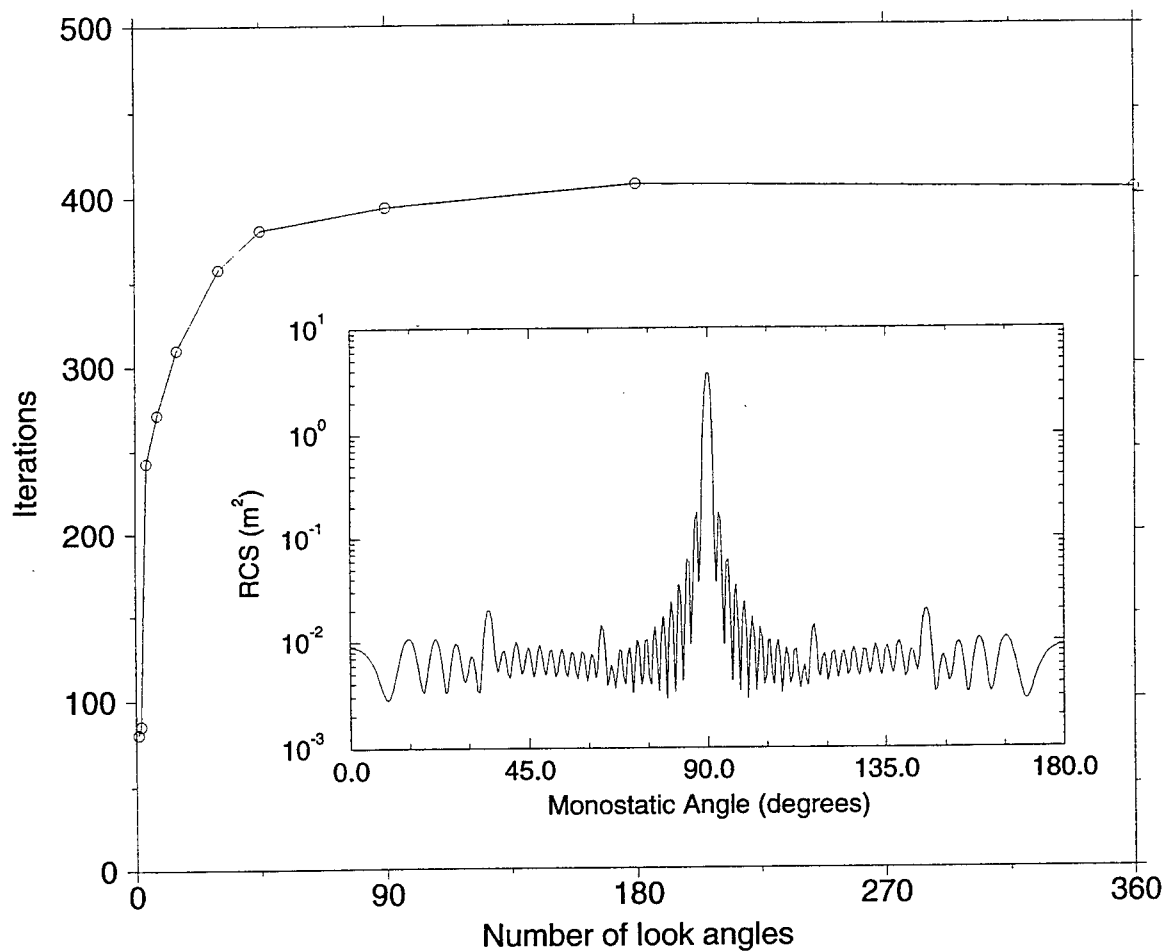


Figure 3

NASA almond (7 GHz, 6 wavelengths long): Monostatic rcs as a function of monostatic incident illumination angle. The illumination ranges from 0 to 180° in the equatorial (VV) plane (solid line), with results every 6 degrees (30 uniformly spaced illumination angles) additionally marked by solid circles. (Also shown are measured results, marked by open circles.)

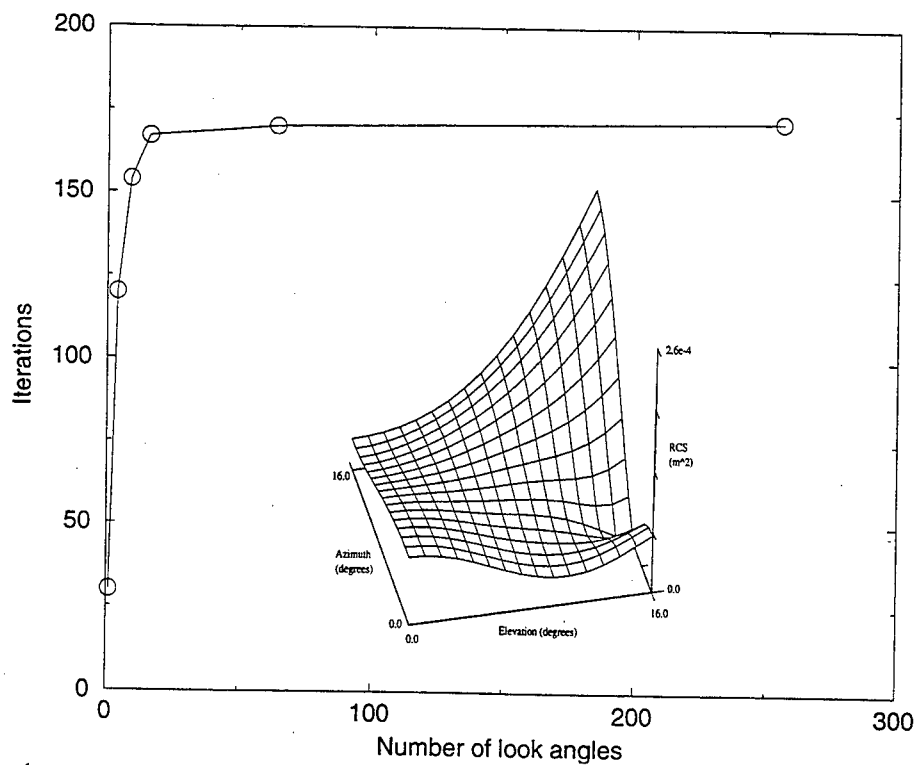


Figure 4

15 wavelength dipole: Iterations required versus number of illumination angles (distributed over 180° in all cases). Inset; Monostatic rcs.

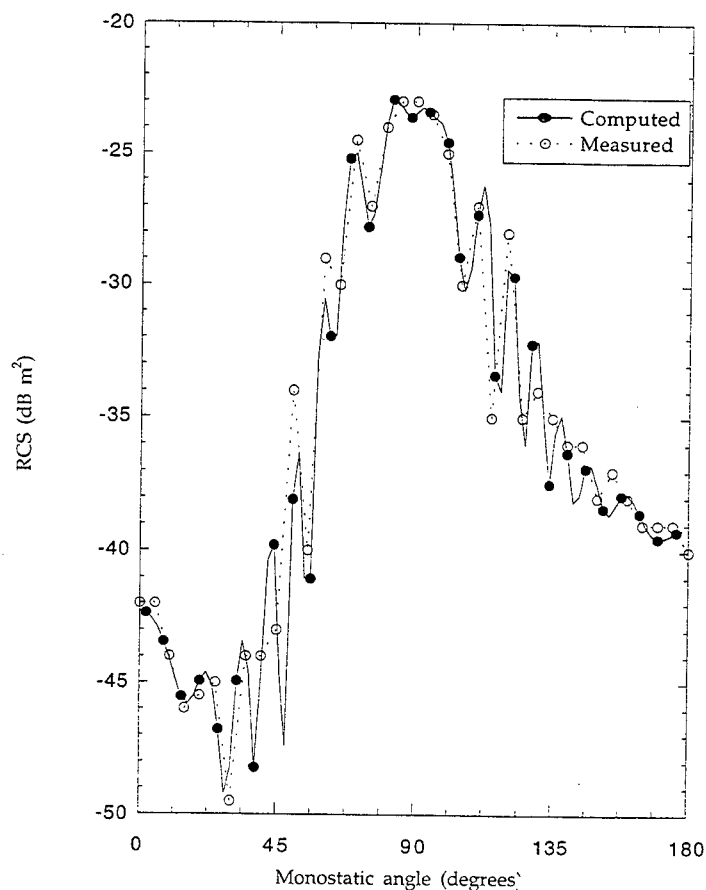


Figure 5

NASA almond (7 GHz, 6 wavelengths long): Iterations required versus number of illumination angles, with uniformly spaced illumination angles over the range $0 - 16^\circ$ horizontally and vertically from head-on. Inset: Monostatic (VV) rcs.

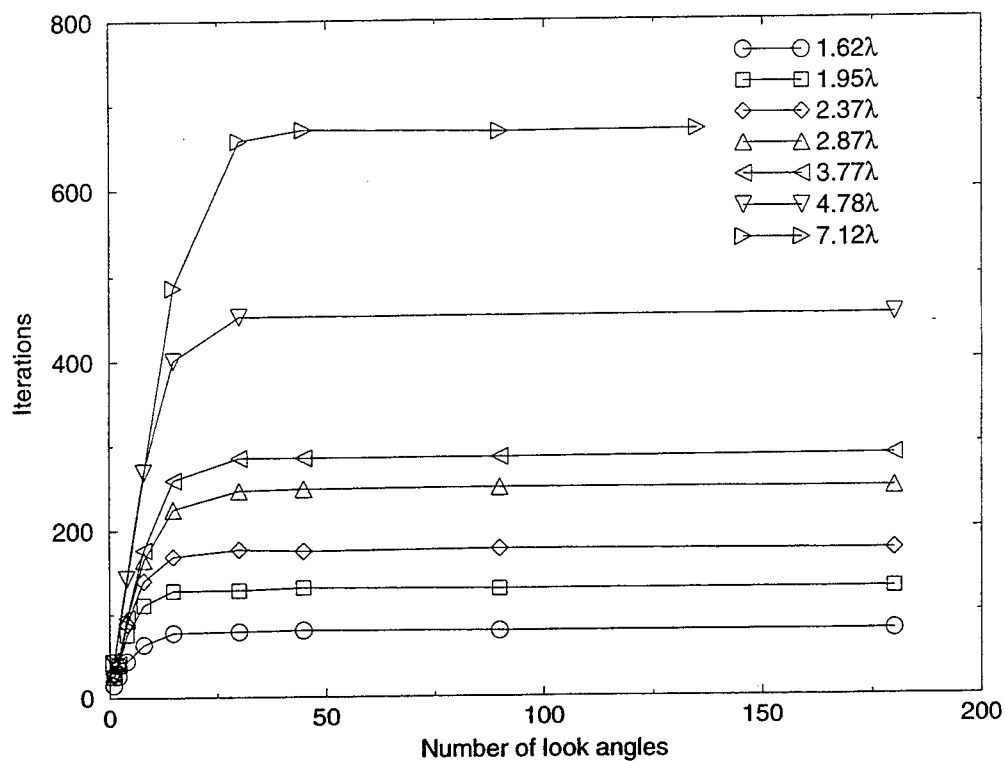


Figure 6

Iterations required versus number of illumination angles for a 180° scan of a series of spheres of diameters (in wavelengths) indicated.

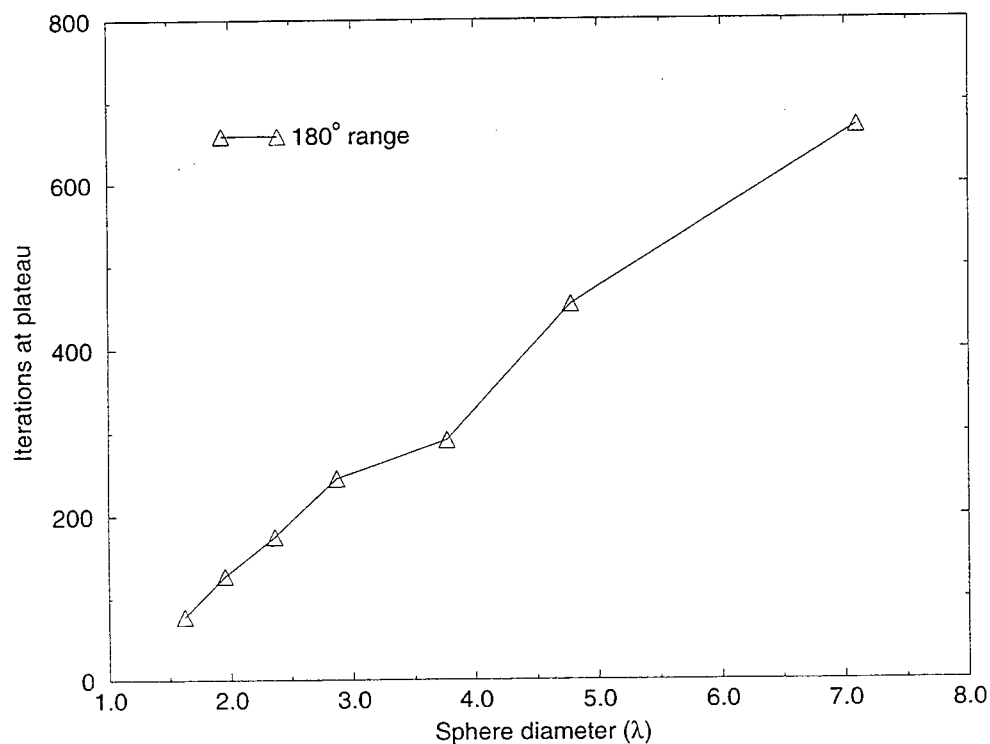


Figure 7

The 'plateau' number of iterations for full 180 degree characterisation, versus sphere diameter in wavelengths.

A FDTD Surface Impedance Boundary Condition Using Z-Transforms

John H. Beggs
Mississippi State University
Department of Electrical and Computer Engineering
Box 9571
Mississippi State, MS 39762

Abstract

The surface-impedance boundary condition for the Finite-Difference, Time-Domain (FDTD) method is reformulated using digital filtering theory and Z transforms. The approach expands upon recent work in developing an efficient surface-impedance boundary condition for FDTD. The present work involves formulating the surface-impedance boundary condition in the frequency domain for a lossy dielectric half-space and for a thin lossy dielectric layer backed by a perfect conductor. The impedance function of the lossy medium is approximated with a series of low-pass filters. This approximation is independent of material properties and these low-pass filters are converted to corresponding digital filters using Z-transform theory. The FDTD surface-impedance boundary condition is reformulated in the Z domain, and the corresponding time-domain electric field sequence updating equation involves a recursive formula. Results are presented for both one and two-dimensional test problems.

1 Introduction

The surface-impedance boundary condition (SIBC) is a frequency-domain concept that is used to simplify scattering calculations by eliminating the internal volume of lossy dielectric objects. The SIBC relates tangential electric and magnetic field components at the surface of the object through an impedance which is a function of the object's material parameters. Thus, the material properties of the object are accounted for, and if exterior fields are only of interest, the SIBC eliminates the need to calculate fields inside the scatterer. This results in a savings in computational resources by reducing the computational storage requirements and/or computation time.

To analyze electromagnetic field interaction with lossy dielectric objects, the Finite-Difference, Time-Domain (FDTD) method requires that the interior of the object be

modeled in order for fields to penetrate the body. Since the wavelength inside a lossy dielectric material is much less than the free space wavelength, accurate modeling often requires a fine spatial grid resulting in a relatively large number of cells for moderately sized objects. For calculations where only exterior response is of interest, a conducting dielectric object can be replaced by a SIBC over the surface of the object. Thus, this boundary condition eliminates the spatial quantization of the object and reduces the overall size of the solution space by eliminating cells within the object and by allowing larger cells to be used in the exterior region. The larger cells reduce the storage requirements since fewer cells are required to model the same physical dimensions of the object. The computation time for the reduced solution space is also decreased because fields in cells within the object are not updated.

Most applications of the SIBC have traditionally been in the frequency domain [1]–[18]. Recently, time-domain surface-impedance concepts have received considerable attention in the literature [19]. There have been several FDTD implementations of the surface-impedance boundary condition introduced by various authors [20]–[38]. Each implementation has certain advantages and disadvantages, but all strive to obtain the most efficient and accurate method. These FDTD surface-impedance boundary conditions are reviewed in a separate article [39].

It has been demonstrated recently that dispersive and nonlinear optical media can be modeled in FDTD using digital filtering and Z-transform theory [40]. Materials with Debye or Lorentz dispersion have rational functions of frequency for the dielectric permittivity. These functions that define relative permittivities as a function of frequency have direct Z-transforms, thus allowing the relationship between electric flux density and field intensity to be formulated directly in the Z-domain. The resulting time-domain updating equations for the sequences involve recursive formulas and are computationally identical to the time-domain, differential-equation based meth-

ods. Excellent results have been obtained in modeling Debye, Lorentz and nonlinear optical media. The difficulty in applying Z-transform theory to the surface-impedance boundary condition is that the frequency-domain, surface-impedance function is irrational. With the recent work of Oh *et al.* [37], the normalized irrational surface-impedance function is approximated with a series of first-order, rational functions. This approximation is independent of material properties, and the first-order, rational functions can be transformed into an equivalent Z-domain form. This paper extends the work in [37] by providing the technical approach for reformulating the surface-impedance boundary condition using digital filtering and Z-transform theory. The surface-impedance boundary condition is converted to the Z-domain by two methods and the resulting recursive updating formulas for the electric field intensity sequence are almost computationally identical to that in [37]. There are several advantages of using the Z-transform approach to implement the SIBC for the FDTD method. The Z-transform approach provides a more accurate, intuitive and consistent method to implement the SIBC based upon the discrete nature of the FDTD method. In the traditional recursive convolution approach, the SIBC is implemented by convolving analog time-domain impedance and magnetic field signals that have been discretized in time. However, the discrete nature of the FDTD method results in discrete impedance and magnetic field sequences which are manipulated easily and accurately using Z-transforms. The Z-domain SIBC system functions are digital filters that operate on the discrete FDTD magnetic field sequences which provides a more accurate implementation and a more intuitive and cohesive theoretical formulation.

In this paper, Section 2 develops the surface impedance boundary condition in the Z-domain and provides the recursive updating equations for the electric field intensity sequence for both a lossy dielectric half-space and a thin lossy dielectric layer backed by a perfect electrical conductor (PEC). Section 3 presents one- and two-dimensional results, and Section 4 provides concluding remarks.

2 Z Transform Approach

This section develops the Z-transform approach for both a lossy dielectric half-space and a thin, PEC-backed, lossy-dielectric layer. The planar first-order, frequency-domain SIBC is used and then an efficient implementation of the corresponding time-domain SIBC is developed using digital filtering and Z-transform theory. This approach is an extension of previous work by Oh *et al.* [37] in developing an efficient time-domain SIBC using recursion. The notation presented in that paper [37] has been pre-

served as much as possible in the present work.

2.1 Lossy Dielectric Half-Space

The first-order (or Leontovich) impedance boundary condition relates tangential total field components and is given in the frequency domain as [4]

$$\vec{E}(\omega) - \hat{n} [\hat{n} \cdot \vec{E}(\omega)] = Z_s(\omega) [\hat{n} \times \vec{H}(\omega)] \quad (1)$$

where ω is the radian frequency, \hat{n} is the unit outward normal from the surface and $Z_s(\omega)$ is the frequency-domain surface-impedance of the material. An $e^{j\omega t}$ time dependence is assumed and suppressed. This frequency-domain SIBC is for a planar material interface and does not account for the surface curvature of an object. Since the present formulation uses the planar SIBC, it is limited to those geometries where the smallest radius of curvature is relatively large compared to the wavelength. The frequency-domain surface-impedance is given by

$$Z_s(\omega) = \sqrt{\frac{j\omega\mu}{\sigma + j\omega\epsilon}} \quad (2)$$

When the impedance boundary is between free space and the dielectric, it is assumed that the complex refractive index, N , obeys the restriction

$$|N| \gg 1 \quad (3)$$

where $N = \sqrt{\mu_r \epsilon_r(\omega)}$. This restriction is imposed so that the wave impedance in the material is independent of the incidence angle and will be equal for both polarizations. This restriction limits the applicability of the present formulation to those media with large conductivity or permittivity, but this restriction is feasible for most practical simulations where a SIBC would be applicable. For cases of low $|N|$, the approach developed by Kellali *et al.* [29] includes the incidence angle in the SIBC. That formulation may be beneficial in cases of lower $|N|$ to avoid gridding and updating fields within a large object. Since the restriction of (3) holds, then (2) is applicable for both polarizations in the two- and three-dimensional cases. This implies that the transmitted fields inside the object will propagate almost normal to the object surface; hence the wave impedance will be equal for both polarizations.

The frequency-domain surface-impedance function of (2) can be rewritten using the complex frequency variable $s = j\omega$ as

$$Z_s(s) = Z_i \sqrt{\frac{s}{s+a}} \quad (4)$$

where $a = \sigma/\epsilon$ and Z_i is the intrinsic wave impedance of the material given by $Z_i = \sqrt{\mu/\epsilon}$. Following the procedure in [37], equation (4) can be rewritten as a normalized

impedance function given by

$$Z_n(s') = \frac{Z_s(s')}{Z_i} = \sqrt{\frac{s'}{s' + 1}} \quad (5)$$

where $s' = s/a$. The normalized surface-impedance function is approximated in the frequency domain by a series of first order rational functions of the form

$$Z_n(s') \approx 1 - \sum_{l=1}^L \frac{C_l}{s' + \omega_l} \quad (6)$$

This approximation is over the real axis interval $s' = [0, 3]$, which will accommodate most materials up to several tens of Gigahertz. The residues C_l and poles ω_l are given for sixth, seventh and eighth-order approximations in [37]. Figure 1 shows the percentage error for the eighth-order approximation, which will be used throughout this paper. Using the approximation in (6),

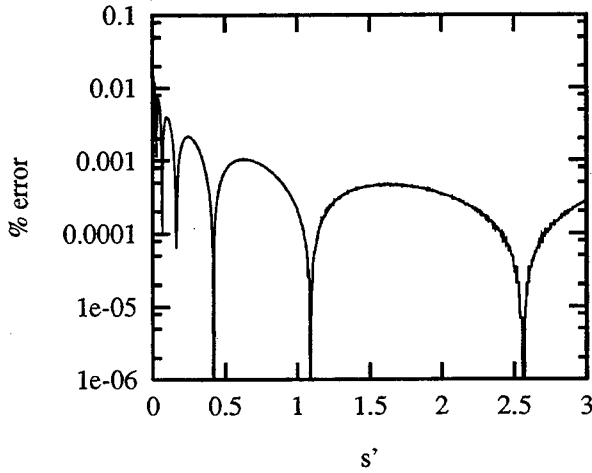


Figure 1: Percent error versus complex frequency (s') in eighth-order approximation to surface impedance function.

the frequency-domain, surface-impedance function can be written as

$$Z_s(s) \approx Z_i - \sum_{l=1}^8 \frac{aZ_i C_l}{s + a\omega_l} \quad (7)$$

The time-domain, surface-impedance boundary condition is obtained by applying the Convolution Theorem to (1) which results in

$$\vec{e}_t(t) = z_s(t) \otimes [\hat{n} \times \vec{h}(t)] \quad (8)$$

where the \otimes is the convolution operator, $\vec{e}(t)$ and $\vec{h}(t)$ are the time-domain electric and magnetic field intensities at the impedance boundary and the subscript 't' denotes tangential field. From (7), it is clear that the time-domain

representation of each first-order rational function is a decaying exponential. As a result, the convolution with the tangential magnetic field can be updated using recursion to avoid storing the complete time history of the magnetic field at the material interface. This recursive approach was first proposed in [22]-[23] and has been expanded upon by several authors [29]-[31], [34]-[38]. Sullivan [41] has shown the multiplication theorem for convolution involving FDTD discrete field sequences includes the sampling factor T . Thus the Z-domain surface-impedance boundary condition is given by

$$\vec{E}_t(z) = Z_s(z) [\hat{n} \times \vec{H}(z)] T \quad (9)$$

Each of the first-order rational functions in (7) is a low-pass filter. When an analog filter function is known, digital filters can be obtained directly using three different approaches [42]. These approaches are discussed in the following sections.

2.1.1 Impulse Invariance Method

The first approach to obtaining a digital filter from an analog filter is to use the impulse-invariance procedure which involves choosing the unit sample response of the digital filter as equally spaced samples of the impulse response of the analog filter. The time-domain, surface-impedance impulse response is found via an inverse Laplace transform of the frequency-domain expression in (7) to be

$$z_s(t) = Z_i \delta(t) - \sum_{l=1}^8 aC_l e^{-a\omega_l t} \quad (10)$$

where $\delta(t)$ is the Dirac delta function. If this time-domain impulse response is now sampled with interval T , the discrete surface-impedance impulse response is

$$z_s(n) = z_s(nT) = Z_i \delta(nT) - \sum_{l=1}^8 aC_l e^{-a\omega_l nT} \quad (11)$$

Taking the Z-transform of both sides of this equation gives the Z-domain, surface-impedance function of

$$Z_s(z) = \frac{Z_i}{T} - \sum_{l=1}^8 \frac{aC_l}{1 - z^{-1}e^{-a\omega_l T}} \quad (12)$$

The Z-domain surface-impedance boundary condition of (9) is then

$$\vec{E}_t(z) = \left[Z_i - \sum_{l=1}^8 \frac{aC_l T}{1 - z^{-1}e^{-a\omega_l T}} \right] [\hat{n} \times \vec{H}(z)] \quad (13)$$

This equation can be rewritten after some algebra as

$$\vec{E}_t(z) = Z_i \left[\hat{n} \times \vec{H}(z) \right] - \sum_{l=1}^8 \vec{F}_l(z) \quad (14)$$

where

$$\vec{F}_l(z) = e^{-a\omega_l T} z^{-1} \vec{F}_l(z) + aC_l Z_i \left[\hat{n} \times \vec{H}(z) \right] \quad (15)$$

is the recursive updating equation in the Z-domain. Recall that the z^{-1} term is a delay operator, and in the time domain, these equations become

$$\vec{e}_t^n(k) = Z_i \left[\hat{n} \times \vec{h}^{n-1/2}(k-1/2) \right] - \sum_{l=1}^8 \vec{f}_l^n(k) \quad (16)$$

with

$$\begin{aligned} \vec{f}_l^n(k) &= e^{-a\omega_l T} \vec{f}_l^{n-1}(k) \\ &+ aC_l Z_i \left[\hat{n} \times \vec{h}^{n-1/2}(k-1/2) \right] \end{aligned} \quad (17)$$

as the recursive updating equation suitable for FDTD implementation. Note that equation (16) is identical to equation (8a) in [37] with a minor change in notation. By using the impulse invariance procedure, it is assumed that the field sequences are piecewise constant in time. This will result in only a first-order accurate boundary condition, similar to the recursive convolution approach for dispersive media involving piecewise constant field components. When implemented and tested, the impulse invariance procedure led to instabilities because of the aliasing problems in the digital filter frequency response, and because the time step chosen for the FDTD calculations was not small enough to resolve the characteristic time constants of some of the exponential terms in the unit impulse response. It is interesting to note that the impulse-invariance design approach was shown to be unstable for FDTD modeling of dispersive media for certain materials exhibiting Lorentz dispersion [43]. Therefore, no results are shown using the impulse-invariance procedure, but this section was included for completeness and for comparison to the other Z-domain methods.

2.1.2 Backward Difference Method

With the frequency-domain surface-impedance of (7), the surface-impedance boundary condition can be rewritten to be

$$\vec{E}_t(s) \approx \left[Z_i - \sum_{l=1}^8 \frac{aC_l Z_l}{s + a\omega_l} \right] \left[\hat{n} \times \vec{H}(s) \right] \quad (18)$$

The backward difference method is a digital filter design technique based upon the numerical solution of a differential equation. Each of the first-order rational terms above

can be thought of as the analog system function for a first-order time-domain differential equation. By approximating the time derivatives in the differential equation by a backward difference, the digital system function is obtained from the analog system function by a substitution of variables

$$s = \frac{1 - z^{-1}}{T} \quad (19)$$

Substituting this into (18) and after some manipulation gives the Z-domain surface-impedance boundary condition

$$\vec{E}_t(z) \approx \left[Z_i - \sum_{l=1}^8 \frac{aC_l Z_l T}{(1 - z^{-1}) + a\omega_l T} \right] \left[\hat{n} \times \vec{H}(z) \right] \quad (20)$$

Note that an extra T term does not appear above because this transformation does not involve the convolution theorem, hence the T factor is not present. After some algebra, equation (20) can be written in the form

$$\vec{E}_t(z) = Z_i \left[\hat{n} \times \vec{H}(z) \right] - \sum_{l=1}^8 \vec{F}_l(z) \quad (21)$$

where

$$\vec{F}_l(z) = \frac{z^{-1}}{1 + a\omega_l T} \vec{F}_l(z) + \frac{aC_l Z_l T}{1 + a\omega_l T} \left[\hat{n} \times \vec{H}(z) \right] \quad (22)$$

is the recursive updating equation in the Z-domain. The time-domain SIBC is the same as that given in (16) with

$$\begin{aligned} \vec{f}_l^n(k) &= \frac{1}{1 + a\omega_l T} \vec{f}_l^{n-1}(k) \\ &+ \frac{aC_l Z_l T}{1 + a\omega_l T} \left[\hat{n} \times \vec{h}^{n-1/2}(k-1/2) \right] \end{aligned} \quad (23)$$

as the recursive updating equation suitable for FDTD implementation.

2.1.3 Bilinear Transformation Method

If the time-domain differential equation used for the backward difference method for each of the first-order rational functions in (18) is integrated, and then this integral is approximated by the trapezoidal rule, the corresponding Z-domain system function can be obtained from the analog function by a different substitution of variables. This is the bilinear transformation method, and the substitution of variables is

$$s = \frac{2}{T} \frac{1 - z^{-1}}{1 + z^{-1}} \quad (24)$$

Performing this substitution of variables in (18) and after some algebra gives the Z-domain surface-impedance

boundary condition to be

$$\vec{E}_t(z) \approx [Z_i - \sum_{l=1}^8 \frac{a C_l Z_i T (1 + z^{-1})}{(2 + a\omega_l T) - (2 - a\omega_l T) z^{-1}}] [\hat{n} \times \vec{H}(z)] \quad (25)$$

Note that an extra T term does not appear above because the bilinear transformation does not involve the convolution theorem, hence the T factor is not required. Equation (25) can be written in the same form as (14) where

$$\vec{F}_l(z) = \left(\frac{2 - a\omega_l T}{2 + a\omega_l T} \right) z^{-1} \vec{F}_l(z) + \left(\frac{a C_l Z_i T}{2 + a\omega_l T} \right) (1 + z^{-1}) [\hat{n} \times \vec{H}(z)] \quad (26)$$

is the recursive updating equation in the Z-domain. The corresponding time-domain SIBC update equation is the same as (16) and the recursive time-domain update equation is given by

$$\begin{aligned} \vec{f}_l^n(k) = & \left(\frac{2 - a\omega_l T}{2 + a\omega_l T} \right) \vec{f}_l^{n-1}(k) \\ & + \left(\frac{a C_l Z_i T}{2 + a\omega_l T} \right) [\hat{n} \times (\vec{h}^{n-1/2}(k - 1/2) \\ & + \vec{h}^{n-3/2}(k - 1/2))] \end{aligned} \quad (27)$$

and is suitable for FDTD implementation. In the paper by Oh *et al.*, the recursive updating equation is given by equation (8b) of that paper [37] (with a slight change of notation) as

$$\vec{e}_i^n(k) = Z_i [\hat{n} \times \vec{h}^{n-1/2}(k - 1/2)] - \sum_{l=1}^8 \vec{A}_i^n(k) \quad (28)$$

where $\vec{A}_i^n(k)$ is the recursive updating variable given by

$$\begin{aligned} \vec{A}_i^n(k) = & \frac{Z_i C_i}{\omega_i} [1 + (e^{-a\omega_i T} - 1)/(a\omega_i T)] \cdot \\ & [\hat{n} \times \vec{h}^{n-1/2}(k - 1/2)] + \\ & \frac{Z_i C_i}{\omega_i} [1/(a\omega_i T) - e^{-a\omega_i T}(1 + 1/(a\omega_i T))] \cdot \\ & [\hat{n} \times \vec{h}^{n-3/2}(k - 1/2)] + e^{-a\omega_i T} \vec{A}_i^{n-1}(k) \end{aligned} \quad (29)$$

The coefficients of this recursive updating equation were obtained by *directly* evaluating the convolution integral of the time-domain surface-impedance function with the tangential magnetic field next to the impedance boundary. The coefficients in (17), (23) and (27) were obtained by manipulating the surface-impedance function in the Z-domain. All of the coefficients in the recursive updating equations of (17), (23), (27) and (29) can be precomputed

and stored to maximize efficiency. Comparing the coefficients in (17), (23) with (29), it is clear that the former two equations are first-order accurate since they only involve one past time level of the tangential magnetic field. Note that the bilinear transformation recursion equation in (27) requires one less multiply and one less coefficient storage location per recursive updating variable than the equation in (29). This makes the bilinear transformation approach slightly more efficient than (29). The bilinear transformation maps the entire left half of the complex plane inside the unit circle and the imaginary axis in the complex plane becomes the unit circle. As a result, frequency warping will take place when transferring from the analog system to the digital system. The bilinear transformation is most useful when this distortion can be tolerated or compensated. When designing a digital filter using the bilinear transformation, the analog cutoff frequencies can be pre-warped so that the digital cutoff frequencies will fall at the correct design cutoff frequencies. However, in this application, this distortion in the frequency axis can be tolerated and no compensation is required.

2.2 PEC-Backed Thin Lossy Dielectric Layer

Following the notation in [37], this section develops a Z-transform SIBC implementation for a PEC-backed, thin, lossy dielectric layer. The geometry is one-dimensional and the lossy dielectric layer has thickness, d , and parameters ϵ_l , μ_l and $\sigma_l \neq 0$. It is assumed that the intrinsic impedance of the dielectric layer, $Z_i(\omega)$, (equation (2)) obeys the restriction given in (3) and that d is less than one-half the cell size. Since the dielectric layer is backed by a PEC, the surface impedance looking into the layer is

$$Z_s(\omega) = Z_i(\omega) \tan(\gamma(\omega)d) \quad (30)$$

where $\gamma(\omega)$ is the propagation constant. If d is small, then the approximation

$$\tan(\gamma(\omega)d) \approx \gamma(\omega)d \quad (31)$$

is applied to (30) to give

$$Z_s(\omega) = Z_i(\omega)\gamma(\omega)d = j\omega\mu_l d \quad (32)$$

Using the Laplace transform variable $s = j\omega$ gives

$$Z_s(s) = \mu_l ds \quad (33)$$

Now that the thin-layer surface-impedance is expressed in terms of s , the Z-transform methods can be applied directly to obtain the corresponding update equations.

2.2.1 Backward Difference Method

For the backward difference method, the substitution of variables given in (19) is used in (33) to give

$$Z_s(z) = \mu_l d \left(\frac{1 - z^{-1}}{T} \right) \quad (34)$$

in the Z-domain. Now the Z-domain SIBC can be written as

$$\vec{E}_t(z) = \frac{\mu_l d}{T} \left[(1 - z^{-1}) (\hat{n} \times \vec{H}(z)) \right] \quad (35)$$

and the time-domain SIBC is given by

$$\vec{e}_t^n(k) = \frac{\mu_l d}{T} \left[\hat{n} \times \left(\vec{h}^{n-1/2}(k - 1/2) - \vec{h}^{n-3/2}(k - 1/2) \right) \right] \quad (36)$$

which is suitable for FDTD implementation. Note that this update equation is identical to (12) in [37]. The backward difference method is the only stable Z-transform method for the PEC-backed, lossy dielectric layer. The bilinear transformation method was unstable because the resulting Z-domain surface-impedance function has a pole at $\Omega = \pi$ where Ω is the digital filter frequency variable.

3 Demonstration

3.1 Lossy Dielectric Half-Space

To demonstrate these different approaches, equation (16), along with the recursive updating equations, (23) and (27) were implemented in a one-dimensional total field FDTD code for the geometry shown in Figure 2. The

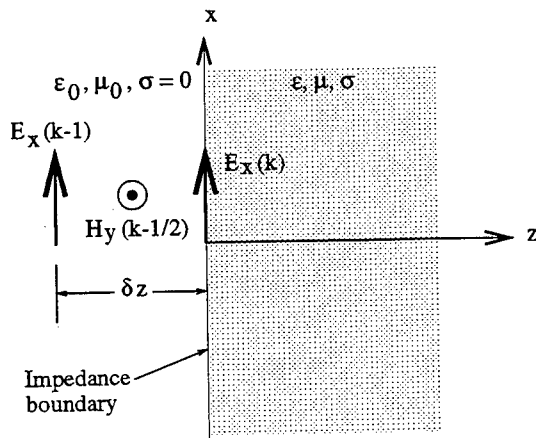


Figure 2: Problem geometry for FDTD SIBC with one-dimensional FDTD grid and the placement of the impedance boundary.

problem was to calculate the reflection coefficient versus

frequency for a pulse normally incident on a lossy dielectric half space. The problem space size was 100 cells, the impedance boundary was located at cell 100 and the electric field was sampled at cell 100. The maximum frequency of interest was 10 GHz and the incident electric field was a Gaussian pulse with unity amplitude of the form

$$E_x^i(t) = e^{-((t-t_0)/\tau)^2} u(t) \quad (37)$$

with $t_0 = 80$ ps and $\tau = 20$ ps. The pulse was windowed in time at approximately -80 dB with a rectangular window width of 64 time steps. The frequency response of the pulse contained significant energy to 12 GHz. Two computations were made with $\sigma = 2.0$ S/m and $\sigma = 200.0$ S/m corresponding to loss tangents at 10 GHz of 3.6 and 360, respectively. The permittivity and permeability of the lossy dielectric half space were taken as those of free space. The cell size and time step were $750 \mu\text{m}$ (40 cells/ λ_0 at 10 GHz) and 2.5 ps respectively, and a total of 8192 time steps were evaluated. For each FDTD computation, a reflection coefficient versus frequency was obtained by dividing the Fourier transform of the scattered field by the Fourier transform of the incident field at cell 100. The incident field was obtained by running the FDTD code with free space only and recording the electric field at cell 100. The scattered field is then obtained by subtracting the time-domain incident field from the time-domain total field. The results are compared with the analytic surface-impedance reflection coefficient computed from

$$|R| = \left| \frac{1 - \sqrt{1 - j\sigma/\omega\epsilon_0}}{1 + \sqrt{1 - j\sigma/\omega\epsilon_0}} \right| \quad (38)$$

where σ is the conductivity of the dielectric half-space. The Z-transform results are also compared with the direct recursive convolution approach of Oh *et al.* [37] using the eighth order approximation and with a conventional FDTD calculation for a simulated lossy half-space. In all figures, the following abbreviations apply: recursive convolution, RC; backward difference, BD; bilinear transformation, BLT. Figures 3 and 4 show the SIBC reflection coefficient results for all methods compared with the analytic SIBC result for $\sigma = 2.0$ S/m and $\sigma = 200.0$ S/m, respectively. Notice the agreement is excellent for the $\sigma = 2.0$ case and is less at higher frequencies in the $\sigma = 200.0$ case. This discrepancy is due to discretization error. In Figure 4, note that the SIBC implementations have approximately the same absolute accuracy as the FDTD result and the SIBC cannot be expected to perform any better than the FDTD calculation. Therefore, these results are encouraging. Comparing Figure 4 to Figure 3c in [37], it is clear that Figure 3c exhibits better agreement at higher frequencies. However, this is because the reflection coefficient shown in that graph was computed

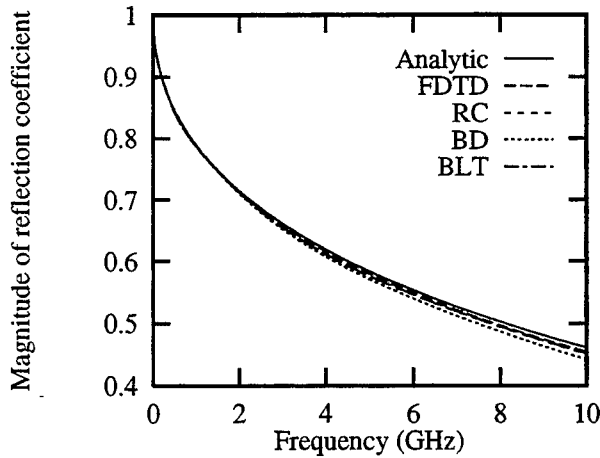


Figure 3: Reflection coefficient magnitude versus frequency for normal incidence plane wave reflection from a lossy dielectric half space with $\sigma = 2.0$ S/m using the analytic and FDTD SIBC methods.

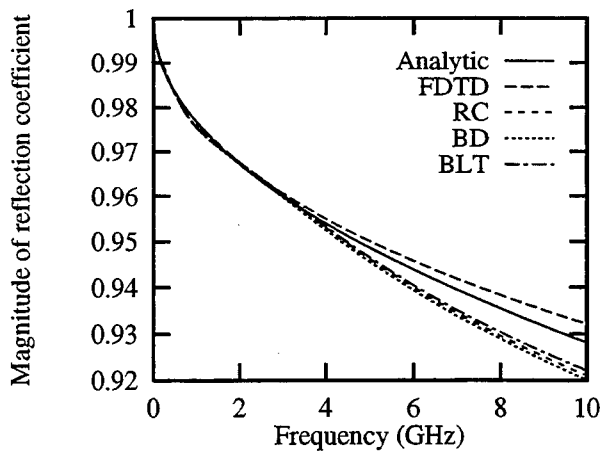


Figure 4: Reflection coefficient magnitude versus frequency for normal incidence plane wave reflection from a lossy dielectric half space with $\sigma = 200.0$ S/m using the analytic and FDTD SIBC methods.

from a closed form representation for the rational function approximation. Note in Figure 4 from [37] that the results for the case of $\sigma = 2.0$ S/m with a six-term rational function approximation exhibit the same type of high frequency behavior as the results presented in Figure 3 and Figure 4. Thus, the results presented here are consistent with those presented in [37]. The Z-transform SIBCs are only first-order accurate overall because the magnetic field at the impedance boundary is approximated by the magnetic field one-half cell in front of the impedance boundary. Although it was anticipated that the bilinear transformation method was second-order accurate in time, when applied in practice, it is only first-order accurate. This is illustrated in Figure 5 where the BLT method is used at a cell spacing of $325 \mu\text{m}$ ($1/2$ the previous cell size) with a conductivity of $\sigma = 200.0$ S/m. Note that

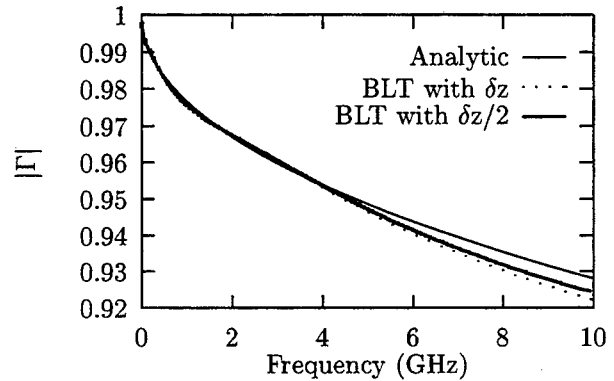


Figure 5: Reflection coefficient magnitude versus frequency for normal incidence plane wave reflection from a lossy dielectric half space with $\sigma = 200.0$ S/m using the FDTD BLT SIBC at grid resolutions of δz and $\delta z/2$.

the new result is approximately 50% closer to the analytical solution. Similar behavior was observed with the BD method.

3.2 PEC-Backed Thin Lossy Dielectric Layer

The calculation parameters for the thin layer example are the same as for the previous example except the material parameters have the following values:

$$\begin{aligned}\epsilon_l &= 2\epsilon_0 \\ \mu_l &= 2\mu_0 \\ \sigma_l &= 2.0 \text{ S/m}\end{aligned}\quad (39)$$

and $d = 0.1\delta z$. In this example, the impedance is calculated at the thin-layer interface by calculating the ratio of the electric and magnetic fields computed via the SIBC.

This is then compared with the exact impedance value computed from (30). Excellent agreement is obtained for the BD Z-transform method as shown in Figure 6.

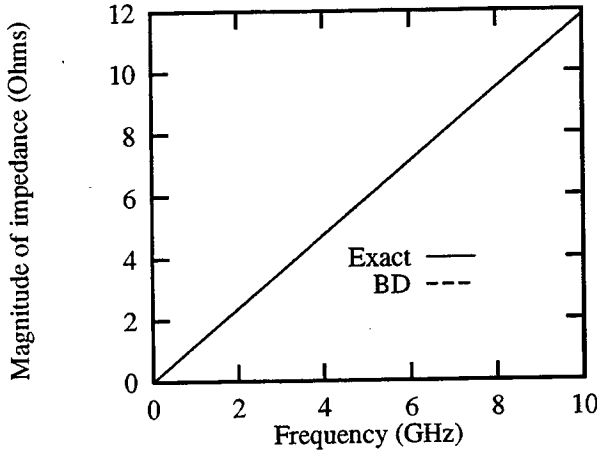


Figure 6: Magnitude of complex impedance for a thin, PEC-backed lossy dielectric layer with $\epsilon = 2\epsilon_0$, $\mu = 2\mu_0$, $\sigma = 2.0$ S/m and $d = 0.1\delta z$.

3.3 Two-Dimensional Scattering Example

In this example, a two-dimensional TM FDTD code was adapted to use the recursive convolution and Z-transform SIBCs. Figure 7 shows the two-dimensional geometry for both the plane wave and point source excitations. A plane wave is incident from the $-x$ axis

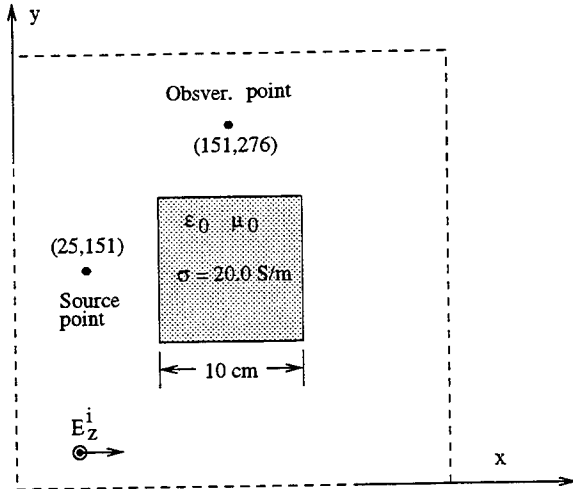


Figure 7: Problem geometry for two-dimensional TM scattering calculations showing square cylinder, incident plane wave, point source and field sampling points.

and a two-dimensional scattering width is calculated for a square cylinder. The cylinder is 10 cm square and has

the following parameters: $\epsilon_r = 1$, $\mu_r = 1$ and $\sigma = 20.0$ S/m. The problem space size was 300 by 300 cells, the cell size is $500 \mu\text{m}$ and the time step is 1.2 ps. Scattering angles of $\phi = 180, 90$ and 0 degrees were used, where ϕ is measured from the $+x$ axis. The incident pulse was of the same form as (37) with $t_0 = 37.7$ ps and $\tau = 9.45$ ps and a second-order Liao absorbing boundary condition was used [44]. Since an analytical solution is not available, each Z-transform approach is compared with a conventional FDTD calculation for the same geometry. Figure 8 shows the monostatic scattering width at $\phi = 180^\circ$ and Figures 9 and 10 show the bistatic scattering width at $\phi = 90^\circ$ and $\phi = 0^\circ$, respectively. Note the agree-

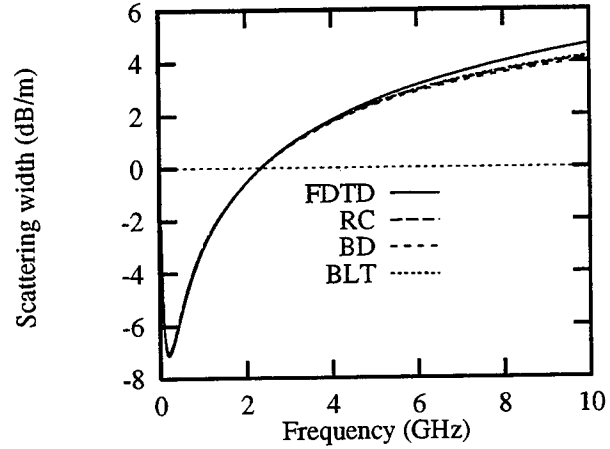


Figure 8: Monostatic scattering width at $\phi = 180^\circ$ for lossy square cylinder using conventional FDTD and the various SIBC implementations.

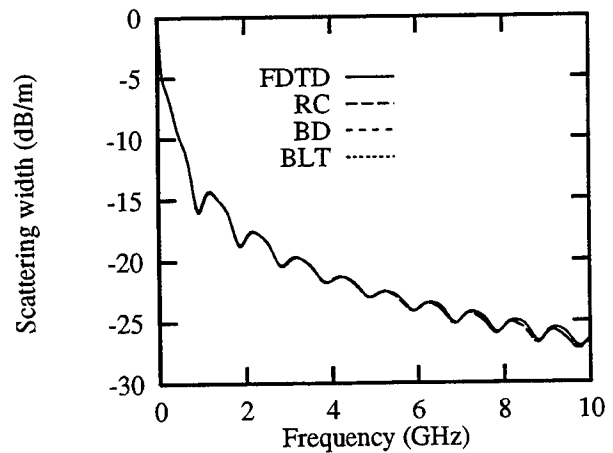


Figure 9: Bistatic scattering width at $\phi = 90^\circ$ for lossy square cylinder using conventional FDTD and the various SIBC implementations.

ment is good in all three cases. It is interesting to note

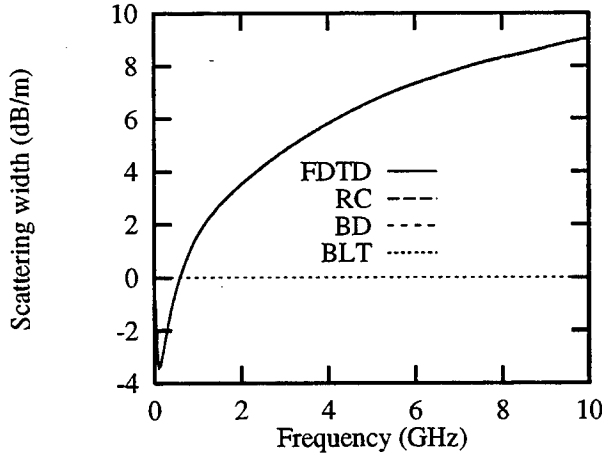


Figure 10: Bistatic scattering width at $\phi = 0^\circ$ for lossy square cylinder using conventional FDTD and the various SIBC implementations.

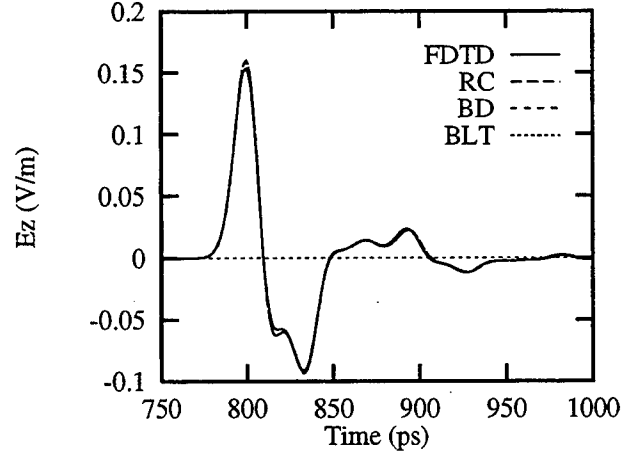


Figure 11: Near zone scattered electric field at a point 25 cells above a 10 cm lossy square cylinder with a point source excitation.

that the half-cell spacing error between electric and magnetic fields in the SIBC seems to manifest itself more in the monostatic scattering width of Figure 7 than in the bistatic scattering width patterns. This is most likely due to cancellation of the SIBC error sources from all four sides of the square cylinder in the bistatic directions. A nonplanar wave example was also used with the excitation point located at grid point i_0, j_0 (see Fig. 7) and a soft excitation source of the form

$$E_z^{total}(i_0, j_0) = E_z^{fdd}(i_0, j_0) + E_z^{inc}(i_0, j_0) \quad (40)$$

where $E_z^{fdd}(i_0, j_0)$ is the free-space electric field updated using FDTD and $E_z^{inc}(i_0, j_0)$ is the source term of the same form as (37). The source point was located at $i_0 = 25, j_0 = 151$ and the pulse parameters were $t_0 = 37.7$ ps and $\tau = 9.45$ ps with the amplitude of the source at 1000 V/m. The results are shown in Figure 11 for a near-field sampling point located at grid point (151, 276). Note the agreement is excellent for the recursive convolution method and for both Z-transform methods.

4 Conclusion

An efficient implementation of the frequency-dependent SIBC for the FDTD method based upon Z-transforms has been presented. Both the backward difference and bilinear transformation Z-transform methods were implemented and tested for a lossy dielectric half-space and the backward difference method was implemented and tested for a thin PEC-backed lossy dielectric layer. Excellent agreement was obtained on one- and two-dimensional TM problems using both

plane and nonplanar wave excitations. Although only a square geometry was considered in the two-dimensional example in this paper, scattering from circular cylinders was demonstrated using a similar SIBC in [27]. The extension to the two-dimensional TE case and the three-dimensional case is straightforward.

Acknowledgements

The author would like to thank the anonymous reviewers for their comments and suggested improvements for this paper.

References

- [1] M. A. Leontovich, "On the approximate boundary conditions for electromagnetic fields on the surface of well conducting bodies", in *Investigations of propagation of radio waves*, B. Vvedensky, Ed., pp. 5–20. Moscow: Academy of Sciences USSR, 1948.
- [2] M. A. Leontovich, "Approximate boundary conditions for the electromagnetic field on the surface of a good conductor", in *Investigations on Radiowave Propagation*, V. A. Fock, Ed., pt. 2, pp. 5–12. Printing House of the Academy of Sciences, Moscow, 1957, Translation: V. A. Fock, *Diffraction refraction and reflection of radio waves*, Appendix, Air Force Cambridge Res. Center TN-57-102.
- [3] Z. Godzinski, "The surface impedance concept and the structure of radio waves over real earth", *Proc. IEE*, vol. 108C, pp. 362–373, March 1961.

- [4] T. B. A. Senior, "Impedance boundary conditions for imperfectly conducting surfaces", *Appl. Sci. Res. B*, vol. 8, pp. 418-436, 1960.
- [5] T. B. A. Senior, "Impedance boundary conditions for statistically rough surfaces", *Appl. Sci. Res. B*, vol. 8, pp. 437, 1960.
- [6] S. N. Karp and Jr. F. C. Karal, "Generalized impedance boundary conditions with applications to surface wave structures", in *Electromagnetic Wave Theory*, J. Brown, Ed., pt. 1, pp. 479-483. Pergamon, New York, 1965.
- [7] J. R. Wait and C. M. Jackson, "Calculations of bistatic scattering cross section of a sphere with an impedance boundary condition", *J. Res. NBS, USNC-RSI*, vol. 69D, no. 2, pp. 298-315, Feb. 1965.
- [8] K. M. Mitzner, "An integral equation approach to scattering from a body of finite conductivity", *Radio Sci.*, vol. 2, no. 12, pp. 1459-1470, Dec. 1967.
- [9] M. Ohkubo, "The surface impedance of a moving medium", *Elect. Comm. in Japan*, vol. 52-B, pp. 125-128, 1969.
- [10] A. L. Weinstein, *The Theory of Diffraction and the Factorization Method*, Golem, Boulder, CO, 1969.
- [11] N. G. Alexopoulos and G. A. Tadler, "Accuracy of the Leontovich boundary condition for continuous and discontinuous surface impedances", *J. Appl. Phys.*, vol. 46, no. 8, pp. 3326-3332, August 1975.
- [12] J. R. Wait, "Exact surface impedance for a cylindrical conductor", *Elec. Lett.*, vol. 15, no. 20, pp. 659-660, Sept. 1979.
- [13] J. R. Wait, "Exact surface impedance for a spherical conductor", *Proc. IEEE*, vol. 68, pp. 279-281, Feb. 1980.
- [14] T. B. A. Senior and J. L. Volakis, "Sheet simulation of a thin dielectric layer", *Radio Sci.*, vol. 22, pp. 1261-1272, 1987.
- [15] D. Wang, "Limits and validity of the impedance boundary condition on penetrable surfaces", *IEEE Trans. Antennas Propagat.*, vol. AP-35, pp. 453-457, April 1987.
- [16] T. B. A. Senior and J. L. Volakis, "Derivation and application of a class of generalized boundary conditions", *IEEE Trans. Antennas Propagat.*, vol. 37, no. 12, pp. 1566-1572, Dec. 1989.
- [17] J. L. Volakis and T. B. A. Senior, "Applications of a class of generalized boundary conditions to scattering by a metal-backed dielectric half-plane", *Proc. IEEE*, vol. 77, pp. 796-805, May 1989.
- [18] K. W. White and R. Mittra, "A systematic study of the impedance boundary condition", in *Proc. 1990 IEEE Antennas Propagat. Int. Symp.*, Dallas, TX, May 6-11 1990, pp. 870-873.
- [19] F. M. Tesche, "On the inclusion of loss in time-domain solutions of electromagnetic interaction problems", *IEEE Trans. Electromagn. Compat.*, vol. EMC-32, pp. 1-4, Feb. 1990.
- [20] J. G. Maloney and G. S. Smith, "Implementation of surface impedance concepts in the finite-difference Time-domain (FD-TD) technique", in *IEEE Antennas and Propagat. Soc. Int. Symposium*, Dallas, TX, May 1990, vol. 4, pp. 1628-1631.
- [21] D. J. Riley and C. D. Turner, "The inclusion of wall loss in finite-difference time-domain thin-slot algorithms", *IEEE Trans. Electromagn. Compat.*, vol. 33, no. 4, pp. 304-311, 1991.
- [22] J. G. Maloney and G. S. Smith, "The use of surface impedance concepts in the finite-difference time-domain method", *IEEE Trans. Antennas Propagat.*, vol. 40, no. 1, pp. 38-48, 1992.
- [23] J. H. Beggs, R. J. Luebbers, K. S. Yee, and K. S. Kunz, "Finite-difference time-domain implementation of surface impedance boundary conditions", *IEEE Trans. Antennas Propagat.*, vol. 40, no. 1, pp. 49-56, 1992.
- [24] C. F. Lee, R. T. Shin, and J. A. Kong, "Time domain modeling of impedance boundary condition", *IEEE Trans. Microwave Theory Tech.*, vol. 40, no. 9, pp. 1847-1850, 1992.
- [25] T. Kashiwa, O. Chiba, and I. Fukai, "A formulation for surface impedance boundary conditions using the finite-difference time-domain method", *Microwave Opt. Technol. Lett.*, vol. 5, no. 10, pp. 486-490, 1992.
- [26] K. S. Yee, K. Shlager, and A. H. Chang, "An algorithm to implement a surface impedance boundary condition for FDTD", *IEEE Trans. Antennas Propagat.*, vol. 40, no. 7, pp. 833-837, 1992.
- [27] J. H. Beggs, *Finite-Difference Time-Domain Implementation of Surface Impedance Boundary Conditions in One, Two, and Three Dimensions*, PhD thesis, The Pennsylvania State University, University Park, PA, 1993.

- [28] J. H. Beggs and R. J. Luebbers, "Corrections to "Finite-difference time-domain implementation of surface impedance boundary conditions"", *IEEE Trans. Antennas Propagat.*, vol. 41, no. 1, pp. 118, 1993.
- [29] S. Kellali, B. Jecko, and A. Reineix, "Implementation of a surface impedance formalism at oblique incidence in FDTD method", *IEEE Trans. Electromagn. Compat.*, vol. 35, no. 3, pp. 347-356, 1993.
- [30] S. Kellali, B. Jecko, and A. Reineix, "Surface impedance boundary conditions at oblique incidence in FDTD", *Annales des Télécommunications*, vol. 48, no. 5/6, pp. 268-276, 1993.
- [31] S. Kellali, B. Jecko, and A. Reineix, "Absorbing surface impedances of lossy layers in the finite difference time-domain method", *Annales des Télécommunications*, vol. 49, no. 3/4, pp. 154-158, 1994.
- [32] B. Z. Wang, "Time-domain modeling of the impedance boundary condition for an oblique incident parallel-polarization plane wave", *Microwave Opt. Technol. Lett.*, vol. 7, no. 1, pp. 19-22, 1994.
- [33] B. Z. Wang, "Time-domain modeling of the impedance boundary condition for an oblique incident perpendicular-polarization plane wave", *Microwave Opt. Technol. Lett.*, vol. 7, no. 8, pp. 355-359, 1994.
- [34] S. Kellali, A. Reineix, P. Leveque, and B. Jecko, "Time-domain surface impedances of lossless debye media", *Annales des Télécommunications*, vol. 50, no. 7/8, pp. 705-710, 1995.
- [35] C. W. Penney, R. J. Luebbers, and J. W. Schuster, "Scattering from coated targets using a frequency-dependent, surface impedance boundary condition in FDTD", in *11th Annual Review of Progress in Applied Computational Electromagnetics*, Monterey, CA, Mar. 1995, vol. 1, pp. 445-452.
- [36] C. W. Penney, R. J. Luebbers, and J. W. Schuster, "A frequency dependent FDTD surface impedance for scattering", in *IEEE Antennas and Propagat. Soc. Int. Symposium*, Newport Beach, CA, June 1995, vol. 1, pp. 628-631.
- [37] K. S. Oh and J. E. Schutt-Aine, "An efficient implementation of surface impedance boundary conditions for the finite-difference time-domain method", *IEEE Trans. Antennas Propagat.*, vol. 43, no. 7, pp. 660-666, 1995.
- [38] C. Penney, R. J. Luebbers, and J. W. Schuster, "Scattering from coated targets using a frequency-dependent, surface impedance boundary condition in FDTD", *IEEE Trans. Antennas Propagat.*, vol. 44, no. 4, pp. 434-443, 1996.
- [39] J.H. Beggs, "A brief summary of surface impedance boundary conditions for FDTD", in preparation.
- [40] D. M. Sullivan, "Frequency-dependent FDTD methods using Z transforms", *IEEE Trans. Antennas Propagat.*, vol. 40, no. 10, pp. 1223-1230, 1992.
- [41] D. M. Sullivan, "Z-transform theory and the FDTD method", *IEEE Trans. Antennas Propagat.*, vol. 44, no. 1, pp. 28-34, 1996.
- [42] A. V. Oppenheim and R. W. Schaffer, *Digital Signal Processing*, Prentice-Hall, 1975.
- [43] C. Hulse and A. Knoesen, "Dispersive models for the finite-difference time-domain method: Design, analysis, and implementation", *J. Opt. Soc. Am., A Optics Image Sci. Vision*, vol. 11, no. 6, pp. 1802-1811, 1994.
- [44] Z. P. Liao, H. L. Wong, B.-P. Yang, and Y.-F. Yuan, "A transmitting boundary for transient wave analysis", *Sci. Sin., Ser. A*, vol. 27, no. 10, pp. 1063-1076, 1984.

SHIPBOARD HFDF SYSTEM SIMULATION

Jeffrey B. Knorr
Department of Electrical and Computer Engineering
Naval Postgraduate School
Monterey, CA 93943

Abstract - NEC 4.1 has been used to compute the responses of the antennas in a shipboard high frequency direction finding system which employs the CIDF algorithm to derive bearing estimates. This paper discusses the computational results as well as the performance of the simulation in which the results were utilized.

1. INTRODUCTION

1.1. Background

The requirement to carry out high frequency direction finding (HFDF) from both shore stations and ships arose during WWII. As recounted by Price [1] and Redgment [2], [3], it provided a means for countering the German submarine threat to allied merchant ship convoys. The anti-submarine mission, as well as other modern day missions, continue to make shipboard HFDF an important consideration in the design of electromagnetic systems for many ships.

Direction finding from a ship at high frequencies (HF) is a challenging problem because in the HF band, antennas may interact strongly with the ship's superstructure and their in-situ phase and amplitude responses can deviate significantly from their free space responses. The bearing errors observed using simple systems can be 10° - 20° and in some cases, error curves may even be multivalued or discontinuous, as reported by Crampton et al. [4], and Travers et al. [5]. As a result, direction finding (DF) techniques which can be utilized at higher frequencies do not work well aboard ship at HF. At HF, one must use a technique which accounts for the interaction of the antennas with the ship's superstructure. One approach to shipboard HFDF is to use the correlation interferometry direction finding (CIDF) algorithm described by Saucier and Struckman [6]. This algorithm will yield accurate bearing estimates if a sufficiently robust array is used. The algorithm is used to compute the correlation between the complex antenna voltages for an incoming plane wave, and the complex antenna voltages stored in a data base for discrete azimuth angles at the same frequency. The angle of maximum

correlation is used as the bearing estimate.

Implementation of a CIDF system aboard ship requires that the ship be calibrated to create the required database of complex receive antenna voltages for frequencies over the range of interest. This is not a problem as a ship can be calibrated after a DF system is installed. Ships, however, are often reconfigured as new systems are added and old systems are removed or upgraded. The effect of associated topside modifications on the complex receive antenna voltages is generally unknown. If the voltages are perturbed, however, DF system accuracy will be degraded. The problem, is that one does not know if topside modifications will cause unacceptable bearing errors.

1.2 Problem

At present, there is no quantitative method for predicting the effect of topside reconfiguration on the bearing accuracy of a shipboard high frequency direction finding system utilizing the CIDF algorithm. One can recalibrate with each reconfiguration, but this is time consuming, expensive, and wasteful of ship operating time. The objective of the work described here was to determine if state-of-the-art hardware and software would support development of a computer based recalibration decision support system.

In general, one is interested in both HF groundwave and skywave signals, and therefore signals which may be elliptically polarized. However, when HF signals are transmitted from ships and submarines at sea, vertically polarized groundwaves can produce useful signal levels at large distances. To simplify the problem, the scope of this initial investigation was therefore limited to

vertically polarized ground waves.

1.3 Approach

A simulation of a high frequency CIDEF system was constructed using real ship CIDEF software to maintain high fidelity. This software was modified to produce output files containing correlation and bearing estimate values for signals tested against the database. The required calibration database was created by computing the responses of the antennas in the DF array using the Numerical Electromagnetics Code (NEC), version 4.1 [7]. Wire grid models of DD963 Spruance Class destroyers with two different topside configurations were constructed for use with NEC. One ship model had an Anti-Submarine Rocket (ASROC) Launcher in front of the deckhouse, and the other was one where the ASROC launcher was removed and replaced with a Vertical Launch System (VLS). The ASROC launcher was a large rectangular box which was elevated above the deck, whereas the VLS was recessed into the deck and had a much lower profile. These two configurations represented a situation for which the change would raise the recalibration question; a question which at present, cannot be satisfactorily answered. In order to interpret the large correlation and bearing estimate data sets, several programs were written to create 2 and 3-dimensional interactive displays of correlation and bearing error on a Silicon Graphics workstation.

NEC 4.1 was run on both a Silicon Graphics Power Onyx workstation and a CRAY J90 mini supercomputer with 4 processors and 128 MWords (1 GB) of memory. Input and output files were moved over the School's network between these machines and the Silicon Graphics workstation on which the DF system simulation was implemented.

Validation was an important aspect of the work described here. Data for validation were collected in a measurement program in which 1/48th scale brass models of the DD963 were used to measure the amplitude and phase responses of each antenna in the direction finding array. Data were collected for both the ASROC and VLS configurations at 20 frequencies over the range 88.8-1172.64 MHz (1.85-24.43 MHz scaled by the factor 48). Data

were also collected for a single DF antenna mounted on a metal box.

The outdoor measurement facility at which the experimental data were collected was located in San Diego, CA. The 11 foot (3.35 meter) long DD963 models were placed on a lead ($\sigma=5 \times 10^6$ S/m) turntable and illuminated using a log periodic transmit antenna. This antenna was located at a distance of 79 feet (24.08 meters) from the center of the turntable and was mounted on an arch which permitted the elevation angle to be varied. A signal source and a vector receiver were located in a control room adjacent to the turntable. A sample of the signal from the source was fed to the receiver for use as a phase reference. Amplitude measurements were referenced to a $\lambda/4$ monopole which was used for calibration prior to recording data. Data were collected in 1° steps over the 360° azimuth range.

2. Computation of DF Antenna Responses

The antennas used in the DF array on the 1/48th scale brass model of the DD963 were semi-loops with a 230 mil (0.584 cm.) radius. These were constructed from 0.085 inch (0.216 cm), outside diameter, semi-rigid coaxial cable. The feed was a 15 mil (.38 mm.) slit cut in the outer conductor of the coax at the center of the semi-loop (highest point above the mounting plate). At one end of the semi-loop, the coax was shorted to the mounting plate, and at the other end, the coax passed through the mounting plate to provide an output line.

Accurate computation of the responses of the antennas in the DF array was the most critical element of the work described here. Before computing the response of many antennas arrayed on a ship, the response of a single antenna mounted on a metal box, situated on a ground plane, was investigated.

2.1 Response of a Semi-loop Antenna on a Metal Box

A single semi-loop antenna was mounted on one face of a metal cube, midway between its sides and 8 inches above a ground plane. The metal cube was one foot on a side and the semi-loop was contained in a vertical plane normal

to the face of the box on which it was mounted. The semi-loop was therefore responsive to theta polarized signals, which includes the case of vertically polarized ground waves which were of interest in this study. A wire grid computer model of the structure is shown in Fig. 1, where it can be seen that the semi-loop was modeled numerically using 5 segments (the center segment, #3, is the feed). Measurements and computations were carried out over the scaled frequency range 96-1440 MHz (2-30 MHz unscaled) and the numerical and experimental data were compared. In each case, the excitation was a theta polarized plane wave, incident at an elevation angle of 10 degrees. Fig. 2 shows the amplitude and phase response at 96 MHz where results obtained using NEC are seen to be in good agreement with experimental results. Note that the pattern amplitude is plotted in dB on a relative scale (maximum response = 0 dB). Also shown, are numerical results obtained using the code PATCH [8]. It should be noted that measurements and computations were made for a range of elevation angles with good agreement observed in all cases. A more detailed discussion of this structure, and the results obtained appears in Ref. [9]. Obtaining successful numerical results for a single semi-loop mounted on a box gave confidence that the response of the same antenna could be successfully computed when located on a ship.

2.2 Responses of the Semi-loop Antennas in the Shipboard DF Array

The amplitude and phase responses of semi-loop antennas in a shipboard DF array were computed at four frequencies, 1.85, 6.34, 9.25, and 20.075 MHz, and compared with measurement data at the scaled values of these frequencies (88.80, 304.32, 444.00, 963.60 MHz). Again, the excitation was a theta polarized plane wave, but for the ship, the elevation angle was set at 5 degrees. An elevation angle of 0 degrees could not be used for measurements because the measurement range employed a log periodic dipole array which was mounted on an arch and it could not be lowered into the ground. ASROC and VLS configurations of the DD963 with identical 24 element DF arrays were studied. The DF antennas were

deployed around the periphery of the ship, some on the edge of the deck, and some on bulkheads, in approximately mirror image port and starboard locations. Fig. 3a shows a visualization of the numerical model (ASROC configuration), and Fig. 3b shows the 1/48th scale brass model (VLS configuration).

The numerical models of the DD963 consisted of approximately 4000 wires and 7000 segments. Maximum segment length was 1 meter, or 0.1λ at 30 MHz. Some areas of the ship were meshed using a 1 m^2 grid while other areas such as the sides of the ship, were represented using vertical wires spaced by 1 meter. This was considered acceptable since interest here was focused on vertically polarized signals incident over the surface of the sea. For convenience, and to minimize the number of segments in the numerical model, the DF antennas were modeled as 1 m^2 loops in exactly the same locations as the semi-loop antennas in the DF array on the 1/48th scale brass model. The outboard segment of each loop was used as the feed. Although the scaled area of the square loops was about 4 times greater than the area of the semi-loops, both were electrically small, so the difference was of no consequence. There were several areas along the sides of the ship (Fig. 3a) between the deck and the waterline, however, where there were openings as large as 15 meters. As will be shown later, these areas appear to have caused error in the numerical results at the higher frequencies.

Numerical and experimental values of amplitude and phase were generated for each of the 24 antennas in the DF array at the four frequencies mentioned earlier. This resulted in far more data than can be presented here, so only representative results will be shown. The discussion which follows refers to specific antennas in the DF array. The antennas are numbered 1 through 12 going from bow to stern and are designated as port (P) or starboard (S).

To facilitate comparison of data, the results have been displayed for port and starboard antenna pairs, with results for both ASROC and VLS configurations shown on the same plot.

Pattern amplitudes have been normalized (maximum response = 0 dB) to make it easier to compare differences between the configurations. The phase reference is arbitrary both numerically and experimentally, and no attempt was made to match the references. The numerical model of the DD963 is oriented along the x axis in a polar spherical coordinate system. Azimuth is determined by the angle ϕ , which is measured in the x-y plane, in the counter-clockwise direction from the x axis, in accordance with mathematical convention. For measured data, angle is measured clockwise from the bow in accordance with nautical convention. In each case, however, 0 degrees corresponds to the bow of the ship, and the antenna patterns relative to the bow of the ship are correctly depicted, with the port antenna on the left and the starboard antenna on the right. Thus numerical and experimental patterns can be easily compared and their spatial responses are correctly depicted. In the following discussion, the term "azimuth" means relative azimuth in the nautical sense.

Antennas P-3 and S-3 are located on the front of the deckhouse, just behind the ASROC launcher (Fig. 3a). Since these antennas are closest to the ASROC launcher, it was anticipated that they would be most affected by its removal. The surfaces on which these two antennas are mounted are angled outboard by about 20 degrees. Thus, these antennas "look" 20 degrees to port and starboard of the bow, respectively.

Figs. 4a and 4b show the numerical and experimental patterns for antennas P-3 and S-3 at 1.85 MHz. Results for the ASROC configuration appear as a solid curve and results for the VLS configuration appear as a dashed curve. Because the curves are reproduced here in black and white rather than color, the two patterns are indistinguishable in some cases. In this case, the patterns for the two configurations are the same, indicating that the removal of the ASROC launcher had little effect on the patterns of these antennas at this frequency. Both numerical and experimental results show the patterns are approximately omnidirectional with a maximum response about 20 degrees

off the bow. The agreement is quite good.

Figs. 5a and 5b show the numerical and experimental phases for antennas P-3 and S-3 at 1.85 MHz. Again, there is essentially no difference between the results for the ASROC and VLS configurations. Phase is plotted within a 360 degree range, so where phase switching occurs, one must visualize an $n2\pi$ (n =integer) translation which would create a continuous curve. Also, when comparing numerical and experimental results, the fact that the phase references are arbitrary, and different, must be taken into account. Thus, numerical and experimental curves must be overlaid and shifted vertically to achieve alignment so they can be compared. This can be done easily at low frequencies, as in the case of Figs. 5, but visual comparison is difficult at higher frequencies where phase varies rapidly and there are many 360 degree discontinuities.

The numerical and experimental phase responses shown in Figs. 5a and 5b are in reasonable agreement. Numerically, the total phase variation is about 175 degrees. Experimentally, it is about 135 degrees. Most of the phase change which occurs for a DF antenna is due to the offset of the antenna from the center of rotation, which is the center of the ship. Experimentally, for example, when the ship is rotated on the turntable, a given DF antenna will move toward or away from the source as the ship rotates. This will cause phase to advance or retard relative to a reference of fixed phase. Antennas P-3 and S-3, for example, are located a full scale distance of 39.56 meters from the center of rotation. Thus, the distance of these antennas from the source changes by 79.1 meters or 0.49λ at 1.85 MHz. This change in position corresponds to a phase change of 175 degrees, which is in good agreement with the numerical result.

The experimental results for P-3 and S-3 are offset from one another by 180 degrees. The phase curve for P-3 starts at about 155 degrees, while that for S-3 starts at about 335 degrees. These results indicate that on the brass model, antenna P-3 was mounted upside down (rotated 180

degrees) with respect to S-3. This is interesting, but has no effect on the correlation and bearing error results presented later. It would have an impact, however, if numerical and experimental results were cross-correlated.

Figs. 6a and 6b show the numerical and experimental patterns for DF antennas P-3 and S-3 at 9.25 MHz. At this frequency, the numerical results show the port antenna looking about 20 degrees to starboard and the starboard antenna looking about 15 degrees to port (the ship is not symmetric about the keel). The experimental patterns show some scalloping in these directions and maxima to either side. The numerical patterns show a lower response in the stern sector than the experimental patterns. The experimental results show more difference between the ASROC and VLS configurations. The agreement between numerical and experimental results at this frequency is still reasonable, although less satisfying than at 1.85 MHz, probably due to deteriorating fidelity of the numerical model.

As a last example, Figs. 7a and 7b show the patterns of DF antennas P-12 and S-12 at 20.075 MHz. These antennas are mounted on the stern, looking aft. At this frequency, the numerical and experimental patterns for some antennas are still in reasonable agreement, but for others there is significant error. For P-12 and S-12, the experimental results show a maximum response at 180 degrees relative azimuth, as one would expect, and response in the bow sector is down 15-30 dB. The numerical results are quite inaccurate for these antennas. The reason for this, it is suspected, is that the several large openings in the side of the hull ($d=\lambda$; see Fig. 3a) resulted in excitation of a field inside the hull at 20.075 MHz.

It is not possible to present all of the numerical and experimental data which were generated in the course of this study, but those data which have been presented above are representative. Related results can be found in Ref. [10]. The conclusion reached, based on inspection of all numerical and experimental results, is that the numerical models of the DD963 produce good results up to about 9 MHz, but need improvement for use at

higher frequencies. The addition of vertical wires to close the openings in the sides of the hull would probably result in significant improvement and will be investigated.

3. Correlation and Bearing Error

Numerical and experimental DF antenna amplitude and phase data were used in the computer simulation of the DD963 DF system to study the impact of topside configuration changes on system performance. As mentioned earlier, the specific configuration change examined in the work described here was the removal of an ASROC launcher (located just in front of the deckhouse) and its replacement with a VLS.

The DF antenna responses (amplitude and phase vs. azimuth) for the ASROC configuration constitute a database for that configuration. The DF antenna responses for the VLS configuration constitute a database for that configuration, and also represent the responses which would be measured if a signal were incident on the ship in that configuration. Thus, if a signal vector (the set of complex DF antenna responses for a given azimuth) for the VLS configuration is cross-correlated with signal vectors for the ASROC configuration over all azimuths, the result is a cross correlation curve, the peak of which may be used to derive an estimate of the signal angle of arrival. This procedure simulates the effect of calibrating the ship in the ASROC configuration, then changing configuration to VLS, and using the ASROC database to DF signals received in the VLS configuration.

Numerical and experimental DF antenna response data were used to create databases for the ASROC and VLS configurations of the DD963 at four frequencies; 1.85, 6.34, 9.25, and 20.075 MHz. The VLS databases were cross-correlated with the ASROC databases to determine the magnitude of the complex cross-correlation coefficient, derive a bearing estimate, and compute bearing error. These data were then used to generate several displays which permitted the results to be interpreted.

3.1 Cross-correlation Surfaces

Figs. 8a and 8b show the numerical and experimental surfaces of cross-correlation for 1.85 MHz. The vertical (z) axis is the magnitude of the complex correlation coefficient ($0 \leq |R| \leq 1$), the horizontal (x) axis is the difference between the azimuth angle, ϕ , of the VLS signal and the azimuth angle, ϕ_i , of the ASROC database signal ($-180^\circ \leq (\phi - \phi_i) \leq +180^\circ$), and the axis receding into the page (y axis) is the azimuth angle of arrival, ϕ , of the VLS signal ($0^\circ \leq \phi \leq 360^\circ$). If the DF system is performing properly, the surface will have low sidelobes, and a central ridge near $(\phi - \phi_i) = 0$ with $|R| = 1$. A configuration change which causes serious bearing errors will result in a surface with maximum correlation at other locations $(\phi - \phi_i) \neq 0$, usually with $|R| < 1$.

Although only 2D pictures can be presented here, in the actual simulation, the computer display of the cross-correlation surface is interactive and can be rotated about any axis to examine its properties. Figs. 8a and 8b show that simulation results using numerical and experimental DF antenna response data for the ASROC and VLS configurations agree quite well at 1.85 MHz.

3.2 Cross-correlation vs. Azimuth

A cut through the cross-correlation surface, perpendicular to the ϕ axis, yields a cross-correlation curve for a fixed signal angle of arrival, ϕ . A polar plot of this curve gives the relative response of the DF array vs. azimuth, in a format similar to that of a normal antenna pattern. Figs. 9a and 9b, show cuts through the numerical and experimental surfaces (Figs. 8a and 8b) for a signal arrival angle of 232 degrees, as indicated by the radial cursor. The numerical and experimental results both show peak correlation near 232 degrees, indicating little bearing error for this angle of arrival.

Again, only a static 2D result can be presented here, but in the actual simulation, the radial cursor, which indicates the angle of arrival on the computer display, can be moved to any azimuth using a mouse. As the cursor moves on the computer screen, the

proper cross-correlation curve is displayed. Thus, a dynamic picture of the array response vs. azimuth can be quickly and easily obtained, and sectors where bearing errors occur can be easily identified.

3.3 Bearing Error vs. Azimuth

Figs. 10a and 10b show bearing error vs. azimuth at 1.85 MHz as determined from the simulation using numerical and experimental DF antenna responses. The curves both show a worst case bearing error of approximately $\pm 2.5^\circ$. In particular, at 232° , both curves show a small negative bearing error. This negative error (bearing estimate less than true bearing) is also evident in Figs. 9a and 9b where the peak correlation can be seen to occur at a bearing slightly less than that of the cursor which indicates the true bearing.

The simulation can also be used to create a display of the 3 dimensional surface of bearing error vs. azimuth and frequency from curves of the type shown in Figs. 10. This surface makes it possible to easily identify areas of high bearing error over the entire domain of azimuth and frequency.

3.4 RMS Bearing Error

The last display which can be created using the simulation is one of RMS bearing error vs. frequency. In this display, the root mean square bearing error is computed over all azimuth angles at each frequency of interest. This provides an integrated measure of DF system performance. Table 1

Freq. (MHz)	1.85	6.34	9.25	20.077
Num.	1.11°	0.86°	2.80°	7.38°
Expt.	1.20°	0.39°	1.51°	6.20°

Table 1. RMS Bearing Error Predicted by the Simulation.

shows the results obtained using numerical and experimental DF antenna data at the four frequencies investigated in this study.

As indicated earlier, the accuracy of the numerical values of DF antenna response degraded with increasing frequency due to (most probably correctable) deficiencies in the wire

grid model of the DD963. This conclusion was reached by comparing numerical and experimental results and noting that the experimental antenna patterns appeared as one would expect based on frequency and location while the numerical patterns at the higher frequencies did not. That is, there is no reason to suspect that any of the experimental data is incorrect. Thus, simulation results (correlation, bearing error) based on numerical and experimental data were also less consistent at the higher frequencies. This was expected as the simulation output depended on the DF antenna data. However, the data in Table 1 shows that even with this degradation, the RMS bearing error results track quite well since this is a performance measure which is integrated over azimuth. One can therefore tentatively conclude that the computer simulation will correctly predict when bearing error will be caused by a topside change of configuration even at frequencies where there is considerable error in the computation of some DF antenna responses.

4. Conclusions

This paper has presented the results of a study to determine if computer simulation could be used to build a decision support system to determine when topside changes in configuration might require recalibration of a ship's CIDF based high frequency direction finding system. A computer simulation of the DF system was constructed, DF antenna responses required to create the system database were computed, and measurements were made for validation purposes.

The most critical aspect of this work was the use of NEC 4.1 to compute the DF antenna responses. Satisfying results were obtained at the lower frequencies, but computed antenna patterns became less accurate with increasing frequency. This appears to be due to ship numerical modeling deficiencies which are believed to be correctable. Thus, the approach seems quite promising.

The need for additional work on several enabling technologies quickly became clear during the course of this investigation. First, methods which have previously been used to create numerical models of complex structures

are laborious and time consuming. For a computer simulation such as that described in this paper to be realistically implemented, it must be possible to create and modify numerical models quickly and easily. Ideally, one would like to go seamlessly from a ship CAD file to the input file for a CEM code. Presently, one must use software to mesh a structure of interest, fix the result manually, and then translate the output to obtain an input file for the CEM code. When the code is run, errors will likely occur and again, manual work will be required to fix these. More work is needed here.

Good pre-processors and post-processors for NEC (or any other code) are also needed. There is a need to be able to quickly and easily find wires and segments identified in CEM code error and warning messages and to eliminate the conditions causing the problems. Model visualization and file editing capabilities are being developed but have not reached the point where this is a straight forward task for a large file. Lastly, additional work is needed on post processor display capabilities. The processor used for this work, for example, did not permit display of receive antenna amplitude and phase data from the NEC output file, and it was therefore necessary to develop separate software for this purpose.

Lastly, difficulties were encountered using NEC to determine the receiving patterns of multiple antennas. For this, one needs the antenna feedpoint currents. To print only the 24 antenna feedpoint currents, it was necessary to place the feedpoint segments at the beginning of the file, so they appeared in sequence and the NEC print command (PT) could be used to obtain all 24 currents in one run. This required breaking up the input file which is undesirable. It would be much more desirable to be able to reuse the PT command to force printing of the current for each segment desired in a given run.

Acknowledgements

The work reported here represents a significant effort which could not have been accomplished without the support and participation of a number of individuals and organizations.

First and foremost, the author wishes to acknowledge the role of CAPT Charles Ristorcelli, Space and Naval Warfare Systems Command (SPAWAR), who had the foresight to recognize the potential of this research and to support it. John Lovegrove and Gary Wang, also of SPAWAR, helped, particularly in the early phases of the project. John Lovegrove organized a Ship Calibration Workshop which was held at the Naval Command Control and Ocean Surveillance Center RDT&E Division (NRaD) in San Diego in March 1994. Presentations and discussions included a review of previous modeling efforts and led to the decision to develop the computer simulation described in this paper. The wire grid numerical models of the DD963 were created for the author under subcontract with NRaD by Mr. Lance Koyama. At the Naval Postgraduate School (NPS), Prof. Beny Neta of the Mathematics Department assisted with the installation of NEC 4.1 on several platforms, including the School's CRAY J90, and parallelized the code to reduce run time (see Ref. [11]). Helpful discussions regarding the use of NEC in this application were held with Gerald Burke at Lawrence Livermore Laboratory, Dr. Jay Rockway at NRaD, and Prof. Dick Adler at NPS. A NEC processor, used primarily for visualization, was developed at NRaD by Linda Russell, and was ported, under subcontract to NRaD, to the Silicon Graphics workstation used in this project. Without the visualization capability provided by this software, it would have been extremely difficult, if not impossible to work with a structure as complex as the DD963. In the initial stages of the project, Dr. Ashok Das, under subcontract with Rolands & Associates, assisted with computer runs, developed MatLab programs to display the numerical and experimental DF antenna receive responses, and installed, debugged, and modified a number of programs required in the simulation. The DD 963 brass model measurement program conducted at NRaD was planned with the assistance of Mr. Bill Kordela, and was executed by Mr. Carl Firman. Invaluable assistance was also provided by Mr. Roy Overstreet, Naval In-Service Support Engineering (West), who was able to answer numerous important questions based on his experience with the DF system, and also provided a number of the system

software programs which were used in the simulation. The graphic display programs essential to the interpretation of simulation results were developed by LT Steve Robey, USN, for his MSEE thesis. Lastly, support was also provided by the Naval Postgraduate School Direct Funded Research Program which provided funds for cost sharing with the sponsor on this project. The project described in this paper could not have been carried to a successful conclusion without the contributions of these individuals and organizations.

References

- [1] A. Price, *The History of US Electronic Warfare*. Alexandria, VA: Association of Old Crows, 1984, Ch. 3, pp.35-36, Ch. 5, pp. 68.
- [2] P. G. Redgment, "High frequency direction finding in the Royal Navy - Development of equipment for use against U-boats, Part 1", *Journal of Naval Science*, Vol. 8, No. 1, pp. 32-43, 1982.
- [3] P. G. Redgment, "High frequency direction finding in the Royal Navy - Development of equipment for use against U-boats, Part 2", *Journal of Naval Science*, Vol. 8, No. 2, pp. 93-103, 1982.
- [4] C. Crampton, et al., "The performance of high-frequency direction-finders in various types of H.M. ships", *Journal of the Institution of Electrical Engineers*, Vol. 94:3A, Part No. 15, pp. 798-814, 1947.
- [5] D. N. Travers, et al., "Multiloop antenna arrays for high-frequency shipboard direction finding", *IEEE Trans. Ant. and Prop.*, Vol. AP-13, pp. 665-671, 1965.
- [6] N. Saucier and K. Struckman, "Direction finding using correlation techniques," *Proc. IEEE Intl. Symp. on Antennas and Propagation*, pp. 260-263, June 1975.
- [7] G. J. Burke, "Numerical Electromagnetics Code - NEC-4 Method of Moments, Part I: User's Manual", Report UCRL-MA-109338, Lawrence Livermore National Laboratory, Livermore, CA, January 1992.

[8] W. Johnson, et al., "Patch Code Users' Manual", Report SAN87-2991, Sandia National Laboratories, Albuquerque, NM, May 1988.

[9] J. B. Knorr and D. C. Jenn, "A numerical and experimental investigation of a semi-loop antenna on a metal box," *Proc. 12th Annual Review of Progress in Applied Computational Electromagnetics*, Monterey, CA, pp. 832-839, March 18-22, 1996.

[10] J. B. Knorr, "A numerical and experimental investigation of a shipboard DF antenna array," *Proc. 12th Annual Review of Progress in Applied Computational Electromagnetics*, Monterey, CA, pp. 792-801, March 18-22, 1996.

[11] B. Neta and J. B. Knorr, "Running NEC4 on the Cray at NPS," *Applied Computational Electromagnetics Society Newsletter*, Vol. 11, No. 3, pp. 12-15, November 1996.

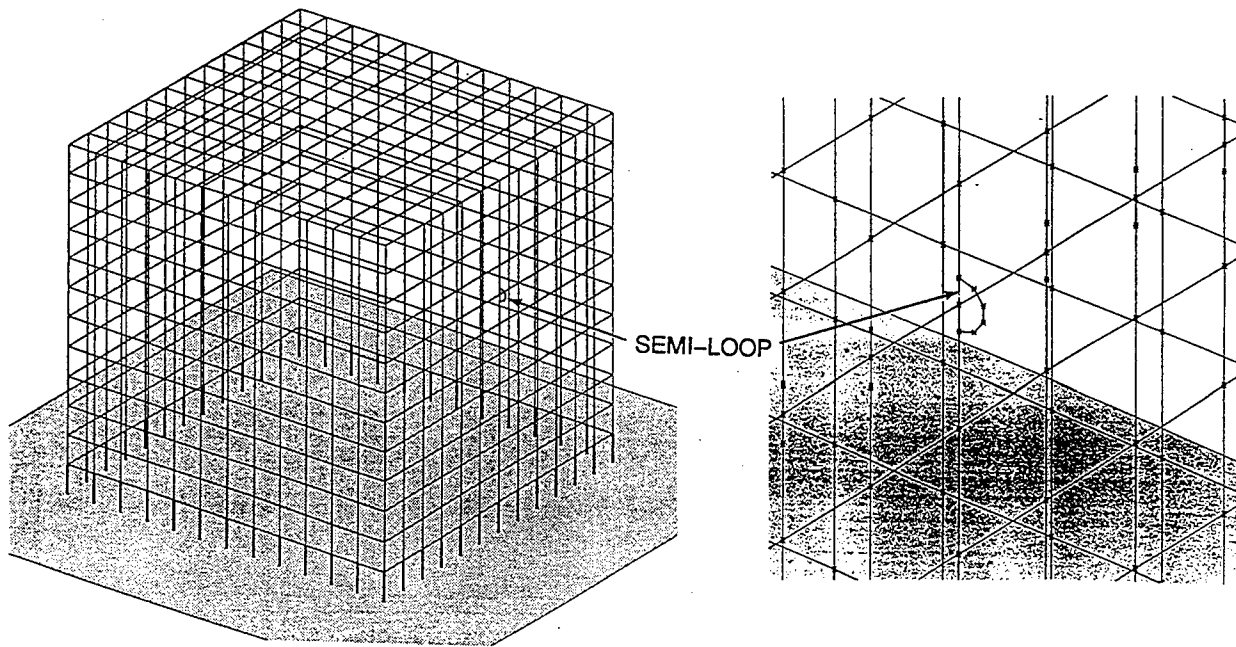


Figure 1. NEC model of the semi-loop antenna on a metal cube.

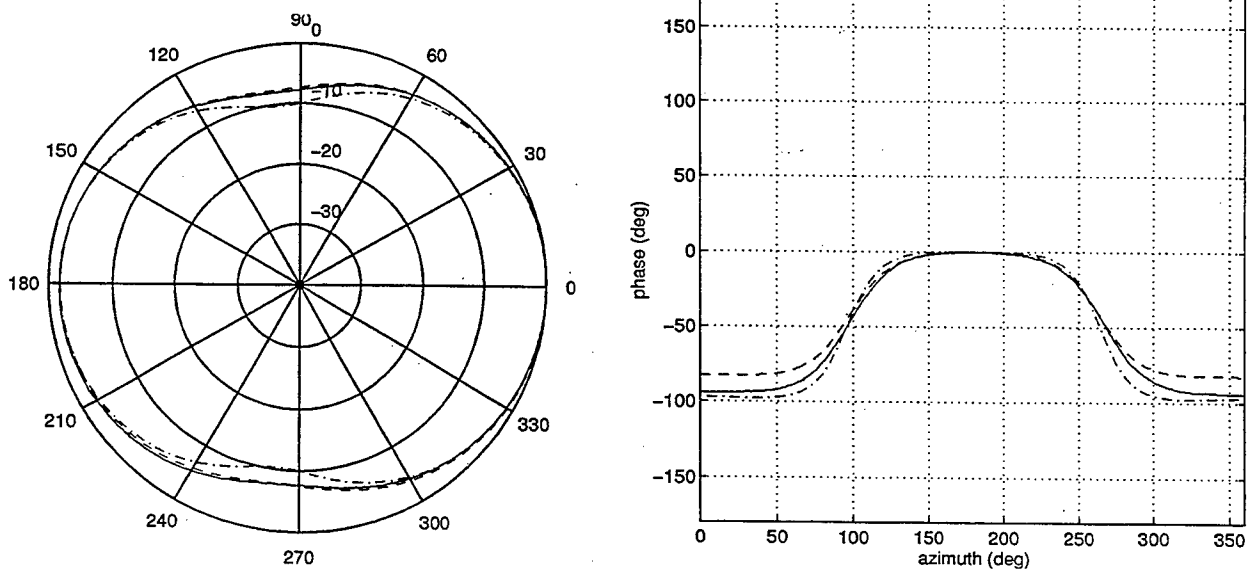


Figure 2. Numerical and experimental amplitude and phase responses for semi-loop antenna on a metal box. Frequency is 96 MHz (2 MHz scaled X48). (___ = measured, -- = PATCH, _._. = NEC)

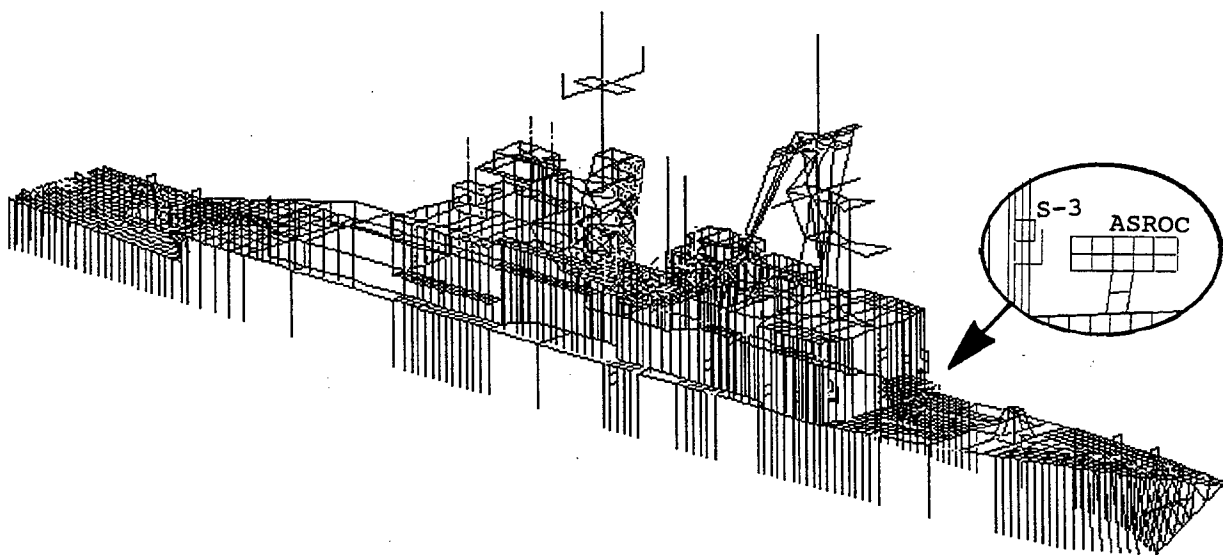


Figure 3a. Visualization of numerical model of DD963 in ASROC configuration.

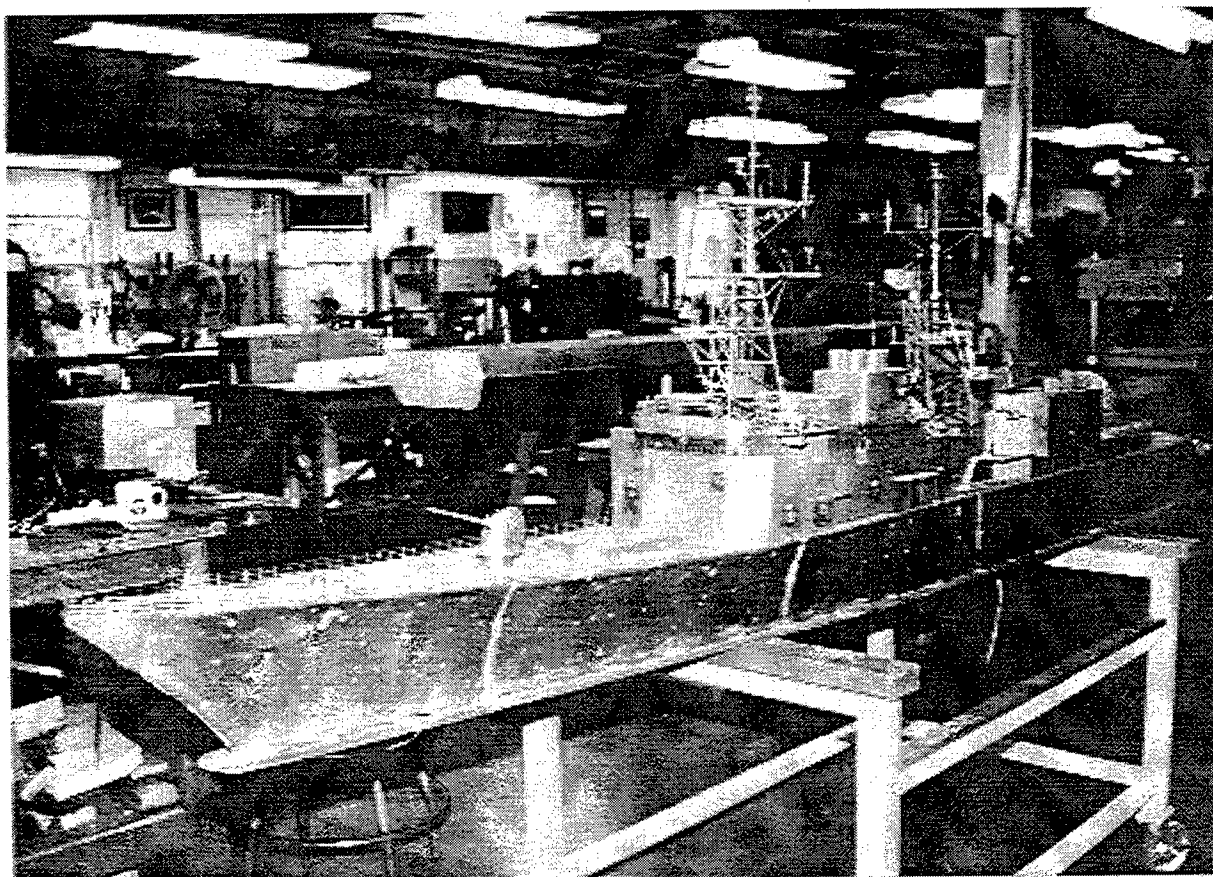


Figure 3b. Brass (experimental) model of DD963 in VLS configuration.

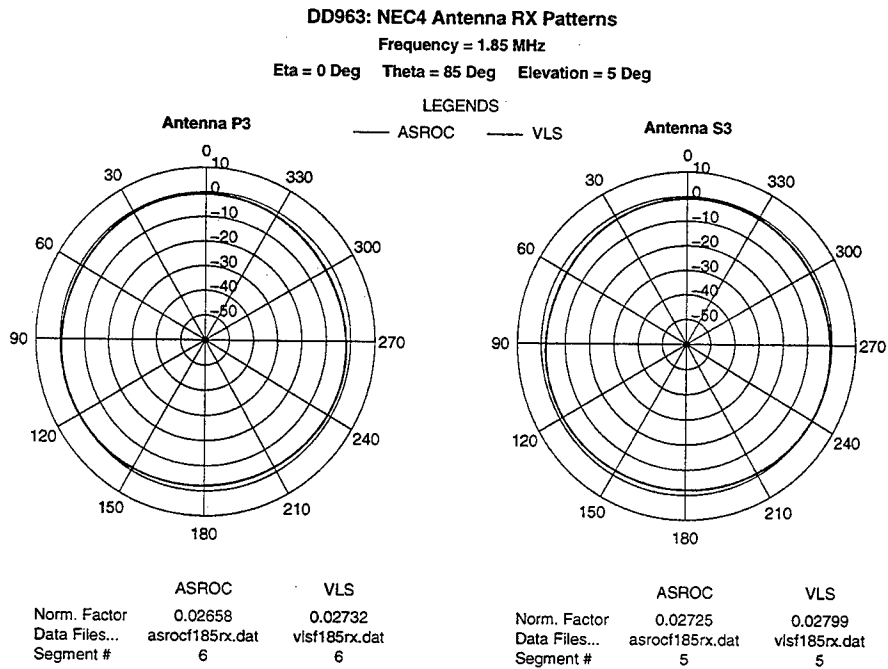


Figure 4a. Numerical patterns of DF antennas P-3 and S-3 for ASROC and VLS configurations of DD963. Elevation angle is 5 degrees, frequency is 1.85 MHz.

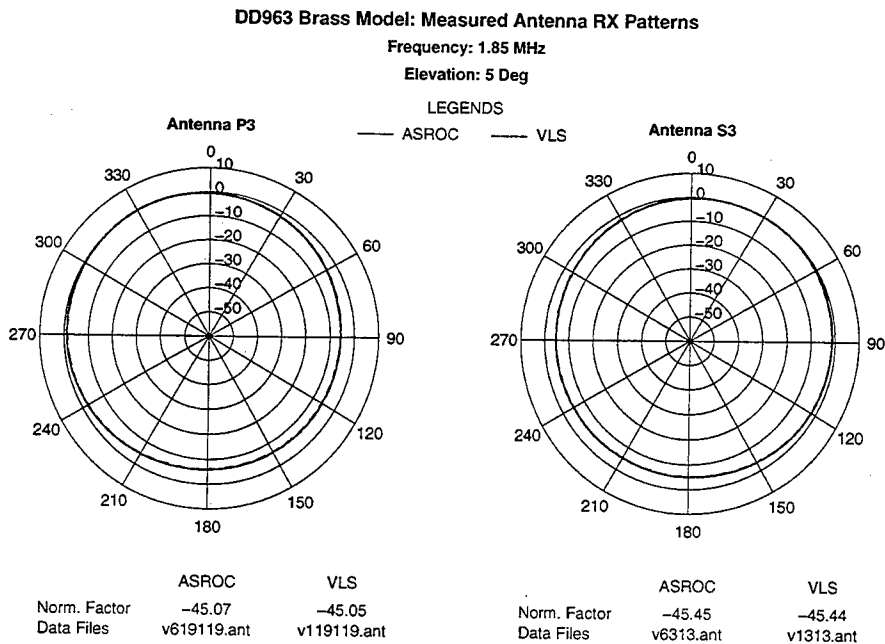


Figure 4b. Experimental patterns of DF antennas P-3 and S-3 for ASROC and VLS configurations of DD963. Elevation angle is 5 degrees, scaled frequency is 1.85 MHz.

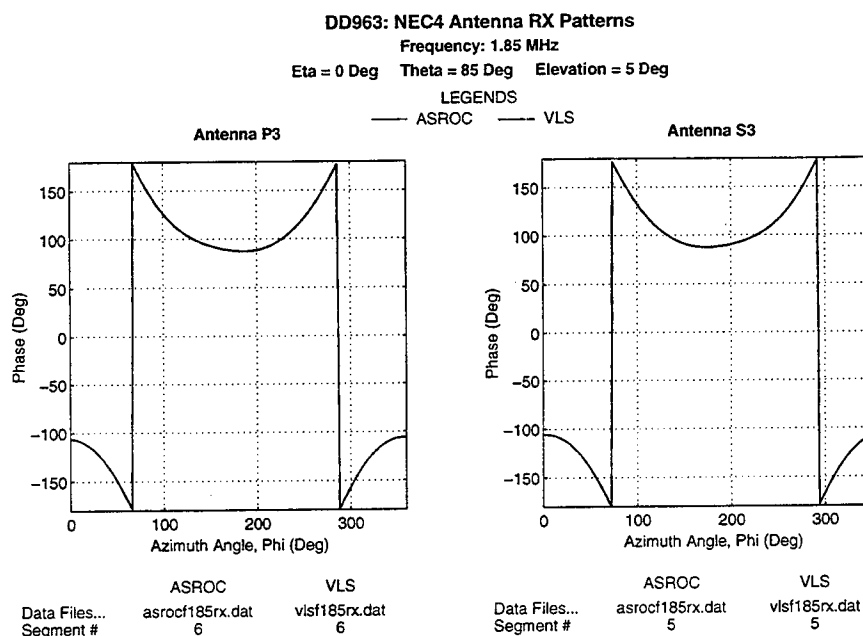


Figure 5a. Numerical phase of DF antennas P-3 and S-3 for ASROC and VLS configurations of DD963. Elevation angle is 5 degrees, frequency is 1.85 MHz.

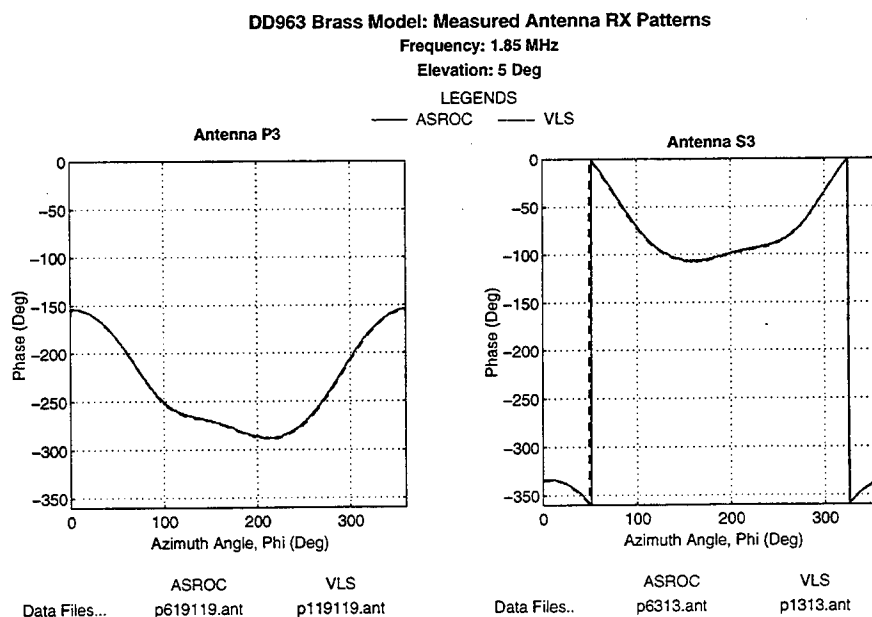


Figure 5b. Experimental phase of antennas P-3 and S-3 for ASROC and VLS configurations of DD963. Elevation angle is 5 degrees, scaled frequency is 1.85 MHz.

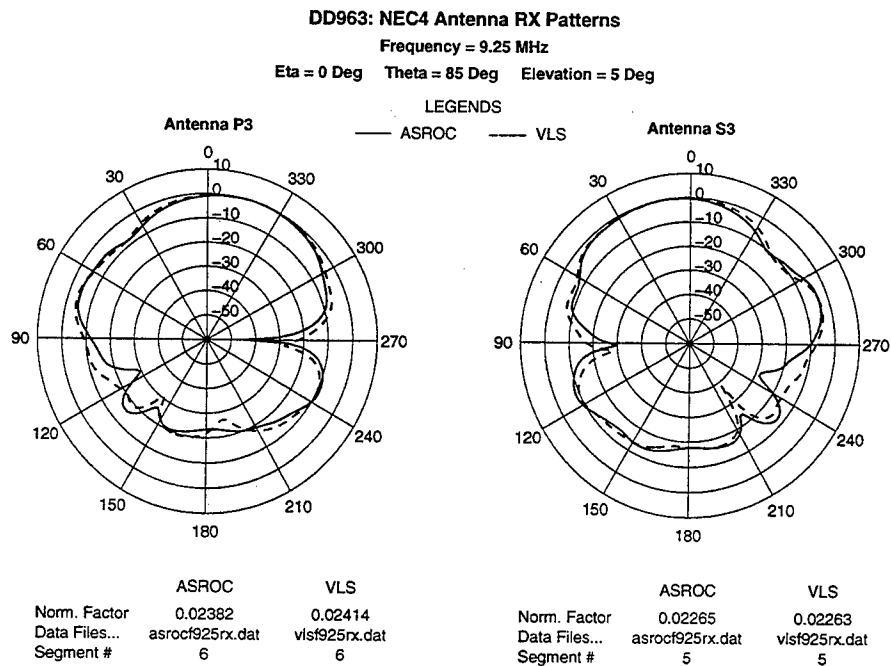


Figure 6a. Numerical patterns of antennas P-3 and S-3 for ASROC and VLS configurations of DD963. Elevation angle is 5 degrees, frequency is 9.25 MHz.

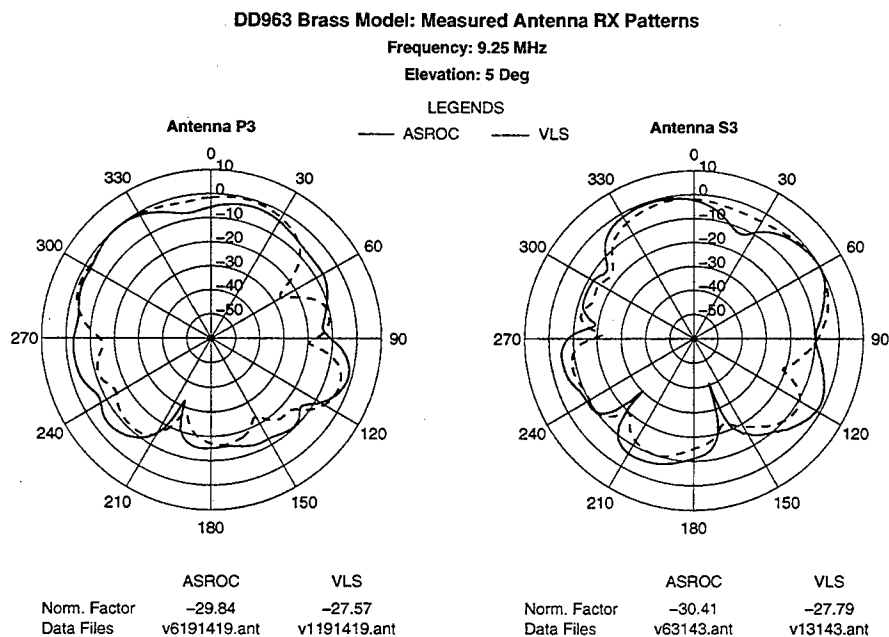


Figure 6b. Experimental patterns of antennas P-3 and S-3 for ASROC and VLS configurations of DD963. Elevation angle is 5 degrees, scaled frequency is 9.25 MHz.

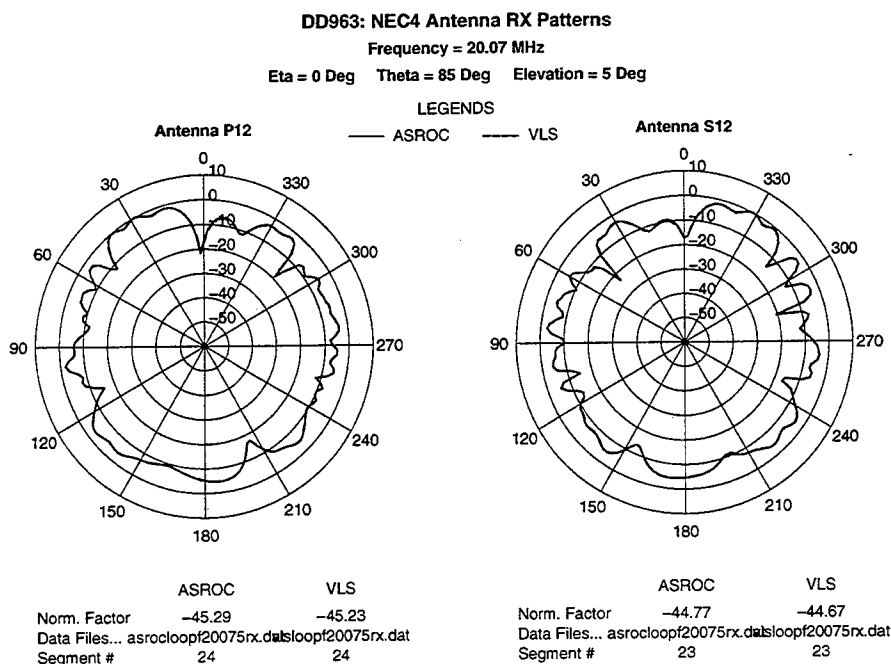


Figure 7a. Numerical patterns of DF antennas P-12 and S-12 for ASROC and VLS configurations of DD963. Elevation angle is 5 degrees, frequency is 20.075 MHz.

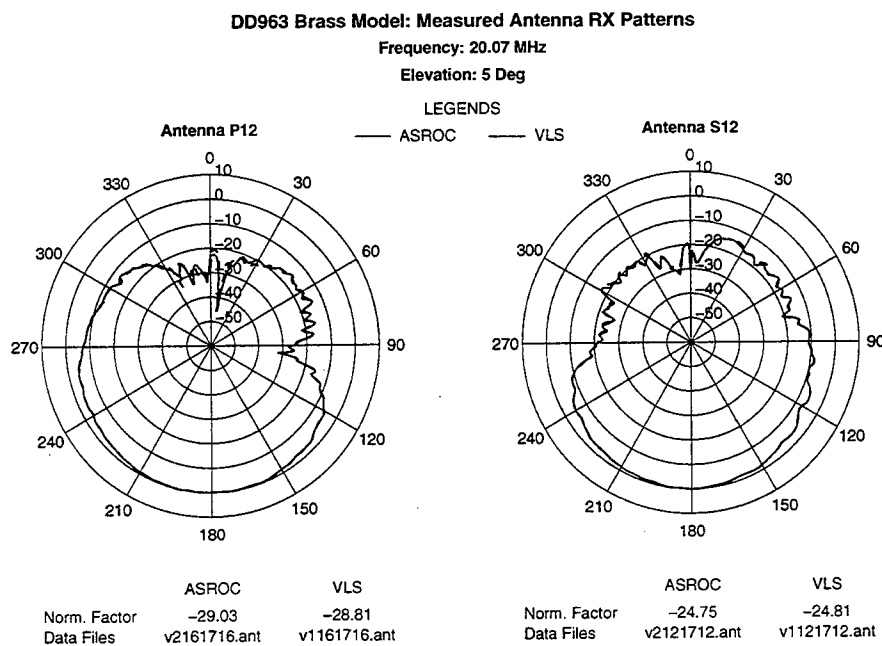


Figure 7b. Experimental patterns for DF antennas P-12 and S-12 for ASROC and VLS configurations of DD963. Elevation angle is 5 degrees, scaled frequency is 20.075 MHz.

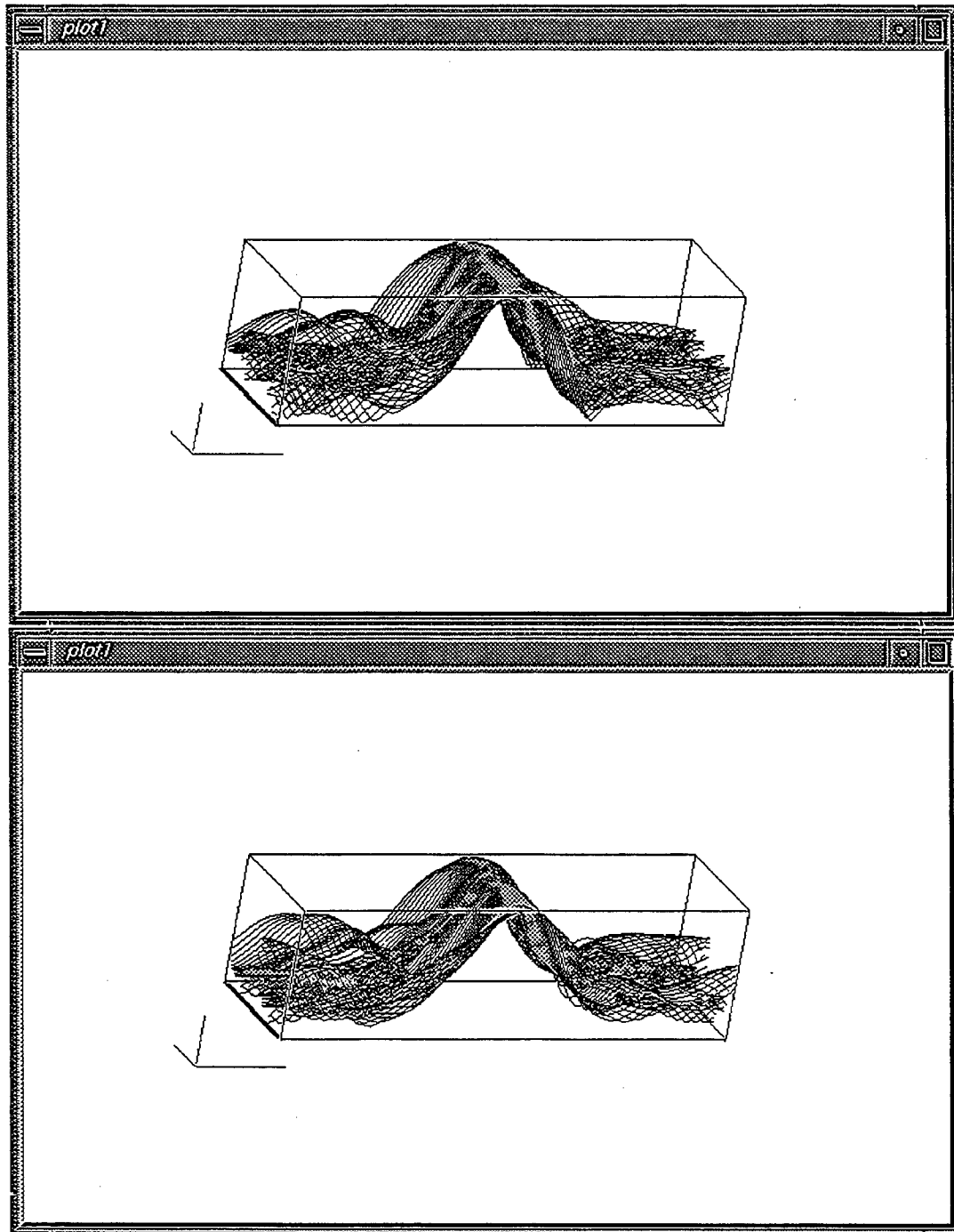


Figure 8. Cross-correlation surface, VLS vs. ASROC configuration of DD963.
(a) Numerical result (top), 1.85 MHz, (b) Experimental result (bottom), 1.85 MHz scaled.

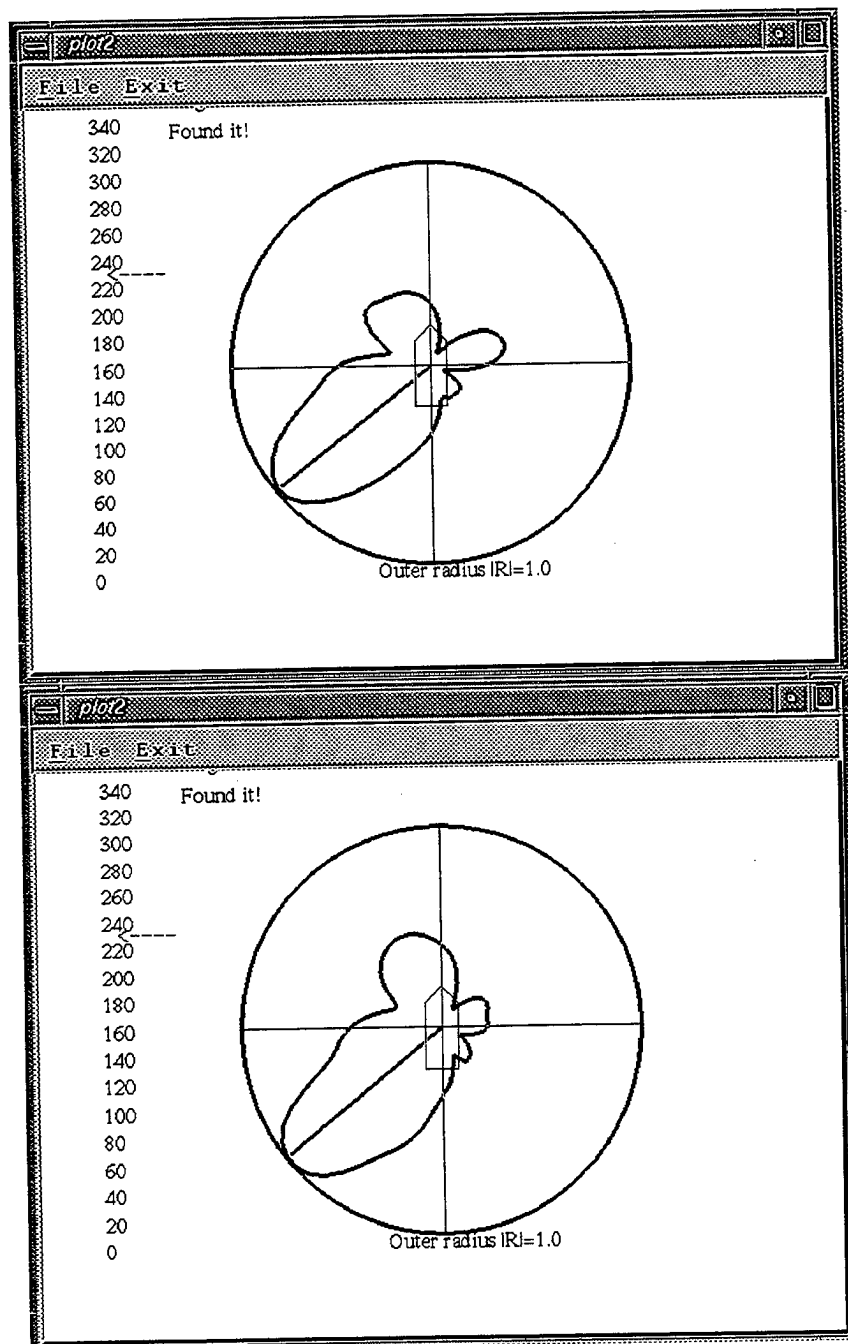


Figure 9. Cross-correlation vs. azimuth, VLS vs. ASROC configuration of DD963. Signal arrival angle is 232 degrees (indicated by cursor). (a) Numerical result (top), 1.85 MHz, (b) Experimental result (bottom), 1.85 MHz scaled.

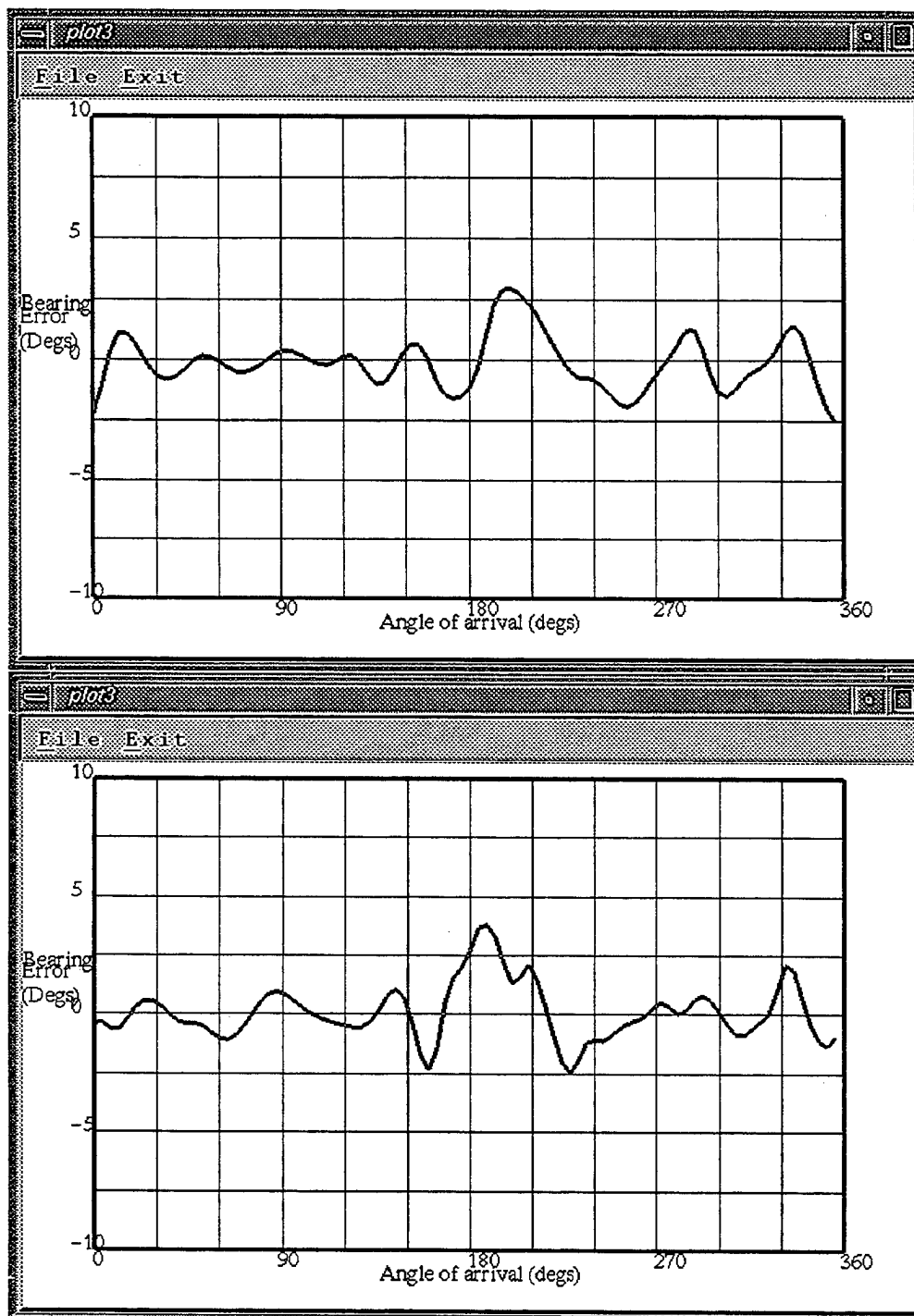


Figure 10. Bearing error vs. azimuth, VLS vs. ASROC configuration of DD963. (a) Numerical result (top), 1.85 MHz, (b) Experimental result (bottom), 1.85 MHz scaled.

Hybrid MoM/SBR Method to Compute Scattering from a Slot Array Antenna in a Complex Geometry

Andrew D. Greenwood* and Jian-Ming Jin
Center for Computational Electromagnetics
Department of Electrical and Computer Engineering
University of Illinois
Urbana, Illinois 61801

*Also affiliated with Air Force Research Laboratory at Rome/IFSB, Rome, NY 13441

Abstract

A method of moments (MoM) code has been developed to compute the scattering from a planar or cylindrically conformal slot array antenna. By hybridizing the MoM with the shooting and bouncing ray (SBR) method, the scattering from a large, complex target with a slot array antenna can be computed. The scattering problem can be decomposed using the field equivalence principle such that the MoM is employed to model the slot array while the SBR method is used to compute the scattering from the large, complex target. Sample results show the utility of the method and the need to include slot array scattering when computing the RCS of a complex target.

1 Introduction

The presence of a slotted waveguide array antenna on a radar target may have a significant contribution to the overall radar cross-section (RCS) of the target. Therefore, the computation of the RCS should include the scattering from the slot array. Recently, a method of moments (MoM) procedure has been introduced to compute the scattering from a cylindrically conformal slotted-waveguide array antenna [1,2]. However, this procedure does not take into account the geometry in which the slot array is located. If the slot array is located in a complex, three-dimensional (3-D) geometry, the MoM cannot efficiently account for the effect of the geometry. A more efficient method to compute the scattering from a large, 3-D body is the high frequency shooting-and-bouncing-ray (SBR) method. However, this method cannot accurately account for the slots, each of which is typically smaller than an electromagnetic wavelength in size. In this paper, the MoM computation of the scattering from a slot array is hybridized with the SBR method to compute the electromagnetic scattering from a large, 3-D target which includes a slot array antenna.

The basis of the hybrid method is the field equivalence principle, which allows the scattering geometry to

be decomposed into separate regions. The MoM is applied to the slotted waveguides, while the SBR method is applied to the region outside the waveguides, which includes the complex, 3-D target. By using the hybrid method, the scattering from a large, 3-D target, which includes a slotted-waveguide array antenna, can be efficiently and accurately computed.

The remainder of this paper is divided into four sections. Section 2 describes the formulation of the problem, including the use of the MoM, the use of the SBR method, and techniques to decouple the computations of the two methods. Section 3 describes briefly how the method has been tested, and Section 4 gives some numerical results which show the capability of the method. The results in Section 4 also demonstrate the need to include the slot array in scattering computations. Finally, Section 5 gives a brief conclusion.

2 Formulation

Consider the example target shown in Figure 1a. The target is complex and 3-D, and it includes a slotted waveguide array antenna on its surface. The slotted waveguide array antenna may be planar, or it may conform to the surface of a cylinder. The first step to compute the scattering from this target is to analyze the slotted waveguides using the MoM. Then, the scattering from the target with the slot apertures covered by perfect electric conductor (PEC) is computed using the SBR method. During the SBR calculation, the incident field on the slot array antenna is computed and stored. This incident field is combined with the MoM analysis to find an equivalent magnetic current on the outer aperture of each slot. Finally, the radiation of these equivalent magnetic currents in the presence of the complex, 3-D target is computed using the reciprocity theorem. This result is added to the previously computed SBR scattering result.

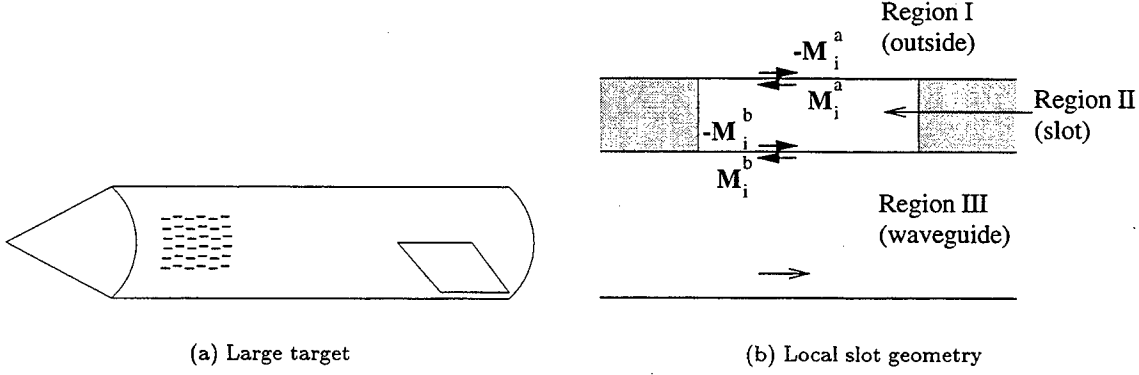


Figure 1: Example of a complex, 3-D target with a slot array antenna and the local slot geometry.

2.1 Use of MoM

The first step in the formulation of the problem is to analyze the slotted waveguides using the MoM. There are two main steps in the application of the MoM. First, the problem must be described in terms of an integral equation. Then, the integral equation is discretized to find a numerical solution. The steps are outlined here, and more detail is given in [1, 2].

To derive the integral equation, the apertures of each slot are first covered with PEC, and equivalent magnetic currents over each aperture are introduced. Figure 1b depicts the situation for the i^{th} slot. The region outside of the antenna is denoted Region I, the region inside the slot is Region II, and the region outside of the slot but inside the waveguide is Region III. An equivalent magnetic current \mathbf{M}_i^a is introduced on the inside of the outer slot aperture (between Regions I and II), and the equivalent current \mathbf{M}_i^b is introduced on the waveguide side of the inner aperture (between Regions II and III). Because the electric field must be continuous across each aperture, $-\mathbf{M}_i^a$ must be introduced on the outside of the outer aperture, and $-\mathbf{M}_i^b$ must be introduced on the slot side of the inner aperture. Note that when the analysis is completed, $-\mathbf{M}_i^a$ are the currents that radiate in the presence of the complex, 3-D body as discussed above.

To derive the integral equation, the continuity of the tangential magnetic field across each aperture is enforced. Denoting the tangential magnetic field in Region III on the i^{th} slot aperture due to the magnetic current on the j^{th} aperture as $\mathbf{H}_{\tau i}^{III}(\mathbf{M}_j^b)$, the following must hold on each inner aperture:

$$\sum_j \mathbf{H}_{\tau i}^{III}(\mathbf{M}_j^b) + \mathbf{H}_{\tau i}^{II}(\mathbf{M}_i^b) - \mathbf{H}_{\tau i}^{II}(\mathbf{M}_i^a) = 0. \quad (1)$$

Further, denoting the tangential incident field on the i^{th}

slot aperture as $\mathbf{H}_{\tau i}^{SBR}$,

$$\sum_j \mathbf{H}_{\tau i}^I(\mathbf{M}_j^a) + \mathbf{H}_{\tau i}^{II}(\mathbf{M}_i^a) - \mathbf{H}_{\tau i}^{II}(\mathbf{M}_i^b) = \mathbf{H}_{\tau i}^{SBR} \quad (2)$$

must hold on each outer slot aperture. Note that the incident fields are calculated using the SBR method, and the magnetic field due to a magnetic current is found from

$$\mathbf{H}^\alpha(\mathbf{M}) = \iint_S \bar{\bar{\mathbf{G}}}^\alpha(\mathbf{r}, \mathbf{r}') \cdot \mathbf{M}(\mathbf{r}') dS' \quad (3)$$

where α is I, II, or III, depending on the region of interest, $\bar{\bar{\mathbf{G}}}^\alpha(\mathbf{r}, \mathbf{r}')$ is the magnetic-source-magnetic-field dyadic Green's function in the appropriate region, and \mathbf{r} corresponds to the point at which the magnetic field is to be evaluated. Combining Equations 1, 2, and 3 gives an integral equation for the magnetic currents.

The second main step in application of the MoM is to discretize the integral equation to find a numerical solution for the currents. To accomplish this step, the currents are expanded in terms of sinusoidal basis functions. Defining $\hat{\xi}$ to be the direction parallel to the lengths of the slots and using a local coordinate system in which $\xi_j = 0$ at one end of the j^{th} slot, the current on the j^{th} slot aperture is expanded as

$$\mathbf{M}_j^\beta = \hat{\xi} \sum_{q=1}^N V_{qj}^\beta \sin\left(\frac{q\pi}{L_j} \xi_j\right) \quad (4)$$

where N is the number of terms in the expansion, and β represents a for the current on the outer aperture or b for the current on the inner aperture. Equation 4 is valid for points on the j^{th} slot aperture; for points outside of the aperture, the expansion is defined to be zero. Assuming the width of a slot is much less than its length, the $\hat{\xi}$ component of the current is the only component of interest.

Substituting the expansion given in Equation 4 into the integral equation allows the integral equation to be converted to a matrix equation which can be solved numerically. For more details about solving the integral equation, the reader is referred to [1,2]. However, one important step that should be mentioned here is the derivation of the dyadic Green's functions for the various regions. The Green's functions given in [1,2] for Regions II and III are applicable to the present problem. For Region I, the dyadic Green's function can be written as

$$\bar{\bar{G}}^I(\mathbf{r}, \mathbf{r}') = \bar{\bar{G}}^{\text{cyl}}(\mathbf{r}, \mathbf{r}') + \bar{\bar{G}}^{\text{diff}}(\mathbf{r}, \mathbf{r}'). \quad (5)$$

The Green's function given in [1,2] for the exterior region corresponds to $\bar{\bar{G}}^{\text{cyl}}(\mathbf{r}, \mathbf{r}')$, and $\bar{\bar{G}}^{\text{diff}}(\mathbf{r}, \mathbf{r}')$ is a perturbation term due to diffraction and reflection by the complex target in which the slot array is embedded. Neglecting $\bar{\bar{G}}^{\text{diff}}(\mathbf{r}, \mathbf{r}')$ neglects fields which are scattered by the slots, diffracted or reflected by the large body back to the slots, and scattered by the slots again [3]. These fields are usually an insignificant part of the scattering, and this term is neglected in the computations. Thus, the Green's function given in [1,2] for Region I is used for the present problem.

2.2 Use of SBR

As previously mentioned, the MoM is used to analyze the slot array antenna while the SBR method is used for the remainder of the problem. Thus, there are three main tasks to be accomplished by the SBR method: to compute the scattering from the complex, 3-D target, to compute the incident magnetic fields on the slot apertures, and to compute the radiation of the equivalent currents on the slot apertures in the presence of the complex, 3-D target. In all of these cases, the slot apertures are covered with PEC.

The details of the SBR method are discussed in [3-6]. For the present problem, the SBR procedure is used to compute the scattering from the complex, 3-D target with the slot apertures closed by PEC. The SBR procedure is implemented using the XPATCH software package [4,5].

The incident magnetic field on the slot apertures is computed using SBR at the same time the scattering from the complex, 3-D target is computed. While tracing the rays to find the scattering, some rays will hit on or near a slot aperture. The field contributions from each of these rays are combined with appropriate phase shifts to find the incident magnetic field on each slot aperture. The incident magnetic fields on the slot apertures are used by the MoM to compute the equivalent magnetic currents on the apertures.

The remaining step in the problem is to compute the radiation of the magnetic currents in the presence of the large body. The SBR method together with the reciprocity theorem is employed for this task [3,6]. Consider an infinitesimal dipole placed at the scattering observation point. If the target containing the slot array is in the far field of the dipole, the dipole launches a plane wave toward this target. Recall that for the SBR method, the grid of rays launched toward the target corresponds to a plane wave. Note also that the reciprocity theorem states

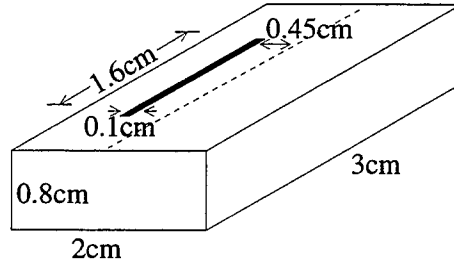
$$\iiint_V \mathbf{E}^{\text{Slot}} \cdot \mathbf{J} dV = \iint_S \mathbf{H}_\tau^{\text{SBR}} \cdot \mathbf{M}^a dS \quad (6)$$

where $\mathbf{H}_\tau^{\text{SBR}}$ is the incident field on the slot apertures due to the dipole at the scattering observation point, \mathbf{M}^a is the current on the outer slot apertures, which is found using the MoM, \mathbf{E}^{Slot} is the radiation due to $-\mathbf{M}^a$, and \mathbf{J} is the dipole current. Thus, if the dipole current (\mathbf{J}) is appropriately chosen and mono-static scattering is being computed, all components to find \mathbf{E}^{Slot} using reciprocity are computed already. If bi-static scattering results are desired, $\mathbf{H}_\tau^{\text{SBR}}$ resulting from a dipole at the scattering observation point must be computed first, then \mathbf{E}^{Slot} can be computed.

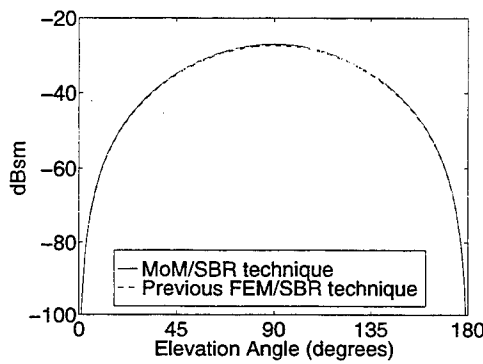
2.3 Decoupling the MoM from the SBR Method

As they are presented in Section 2.1, the MoM computations are coupled to the SBR method computations. This is due to the fact that the incident magnetic field on the slot apertures, which is computed using the SBR method, is required for the MoM computations. To avoid having to repeat the MoM computations in order to analyze the scattering from many different incidence angles, it is desirable to decouple the computations of the two methods. There are two ways of doing this. The first method preserves the coupling interactions between different slots; the second involves an approximation which neglects the coupling between different slots to achieve lower computational complexity.

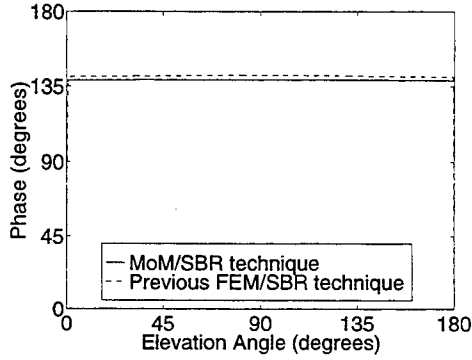
To decouple the MoM computations from the SBR computations while preserving the coupling between the various slots, the incident magnetic field on the slot apertures can be expanded in terms of basis functions. Assuming that the width of a slot is much less than its length, the component of the incident magnetic field along the length of a slot is the only component of interest. A convenient basis set is the set of pulse basis functions, where each function is defined to be one on a portion of a single slot aperture and zero elsewhere. The magnetic currents on each slot aperture are then computed with the incident field on the slot array set equal



(a) Geometry



(b) Magnitude



(c) Phase

Figure 2: Comparison between the proposed MoM/SBR technique and a previously published FEM/SBR technique. The scattering results are computed at a frequency of 8 GHz, and the scattering contribution of the slot only is shown.

to each of the basis functions in turn. A matrix-vector multiply is then carried out during the SBR computations. This matrix-vector multiply converts the incident magnetic fields on the slot apertures to the equivalent currents on the apertures.

The second method of decoupling the MoM computations from the SBR computations neglects the coupling between the individual slots. One slot on the array is chosen, and it is assumed that this slot is the only one present. The MoM computation is carried out with a magnetic field of unit amplitude on the chosen slot, and the result is a magnetic current on the aperture. It is then assumed that all of the slots in the array are equivalent; the magnetic current on each one is set equal to the incident magnetic field times the single magnetic current computed by the MoM. This approximation significantly reduces the computational complexity and the sizes of data files. However, it does not produce accurate results when the frequency is near the working frequency of the slot array. This is demonstrated in Section 4.

3 Testing

Before using any new numerical technique, the technique should be tested against measurements or alternate techniques to ensure its validity. Ideally, measured data is used for comparison, but unfortunately measured data for this problem is unavailable. However, the validity of the MoM computation involving the coupling between the different slots in the array is validated by comparison with previous MoM and finite-element method (FEM) techniques [2, 7]. The SBR method is also validated through extensive, previous testing [4, 5]. The hybrid technique is validated by comparison with a previous hybrid method to compute the scattering from complex targets with cracks and cavities on their surfaces [3]. The comparison is accomplished by considering a waveguide with each end terminated by a (short-circuit) PEC plate and with a single slot on the waveguide surface. The geometry is shown in Figure 2a. The waveguide with a single slot can be modeled both as a slotted cavity for the FEM technique and as a slotted waveguide for the MoM technique. Figures 2b and 2c show a comparison of

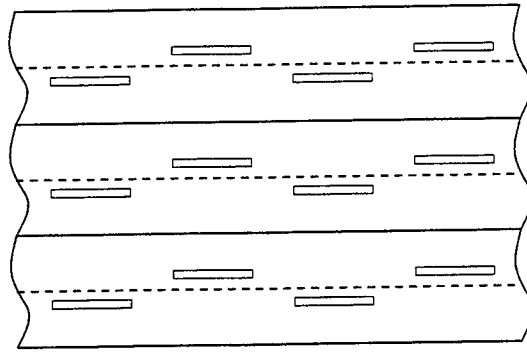


Figure 3: Configuration of the slots on the surface of waveguides.

the magnitude and the phase of the backscattered field from the slot in the presence of the waveguide. There is good agreement both in magnitude and in phase. Both magnitude and phase agreement are important so that when the scattered field from the external geometry is added, correct results are produced.

4 Numerical Examples

To show the capability and utility of the proposed technique, several numerical results are presented. For all of the numerical examples, the slot array contains 16 waveguides with 16 slots on each waveguide, and the array is designed to radiate at 9.1 GHz. In addition, the following parameters apply to all of the examples presented: the upper waveguide wall in which the slots are cut is 0.08 cm thick, the waveguides are separated by walls 0.1 cm thick, each slot is 1.6 cm long and 0.16 cm wide, and the slots are positioned on the waveguide surface as shown in Figure 3, where the offset of each slot from the center of the waveguide is 0.15 cm. Unless otherwise noted, the coupling between individual slots in the array is included in the results.

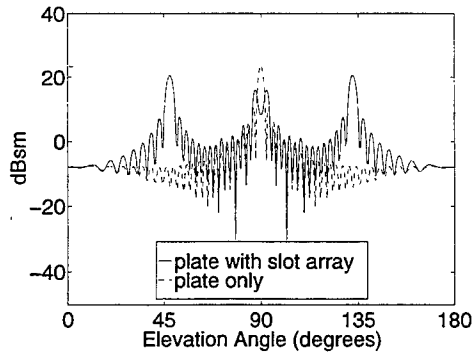
The first example is a planar slot array sitting on a simple ground plane. The waveguides are 2.230 cm wide by 1.016 cm high, the slot centers are 2.444 cm apart, and the first and last slot centers are 1.222 cm from the ends of the waveguides. Thus, the entire slot array and the ground plate are 37.3 cm wide by 39.1 cm long. In Figure 4, the RCS of the plate with the slots is superimposed on the scattering from the plate alone. The scattering frequency is 9.1 GHz, which is the working frequency of the slot array. Figure 4 shows results in both the H -plane and the E -plane and for waveguides which are terminated both with matched loads and with short circuits. For matched waveguide loads, each waveguide is terminated with an impedance sheet which is matched to the characteristic impedance of the guide. In the case of short circuit waveguide loads, each waveguide is ter-

minated with a PEC plate. For some incidence angles, the slot array has a dominant effect on the scattering.

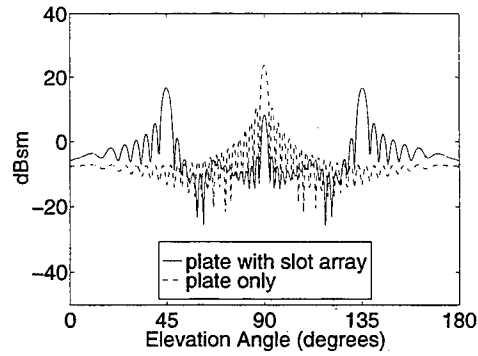
The second example is a slot array on a cylinder with a nose cone. The radius of the cylinder is 16.096 cm, and the length without the nose cone is 100 cm. The nose cone is 30 cm long. The waveguide cross-sections are sectoral in shape and are 1.016 cm thick. Along the slotted surface, the waveguides are 2.230 cm wide. The slots are 2.573 cm apart, and the first and last slots are 1.287 cm from the ends of the waveguides. The entire slot array is 37.3 cm along the circumference of the cylinder and 41.2 cm along the axis of the cylinder. In Figure 5, the H -plane RCS of the cylinder alone and the RCS of the cylinder with the slot array are compared. The scattering frequency is 9.1 GHz, the working frequency of the slot array, and again, there are scattering directions for which the slot array dominates the return.

The next example is intended to show the effect of the uncoupled slot approximation which was discussed in Section 2.3. Figure 6 shows the RCS of the same geometry considered in the second example, but as a function of frequency. The incident direction is 40° in the H -plane. The RCS computed considering the coupling between individual slots is plotted with the RCS computed by neglecting the slot coupling. The approximation neglecting slot coupling is reasonably accurate away from the working frequency of the slot array antenna, but there is significant error near the working frequency. Thus, this approximation must be applied with care.

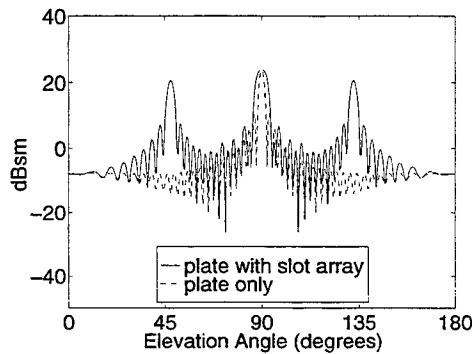
The final example shows the usefulness of the method. The planar slot array antenna from the first example is mounted in the nose cone of an aircraft. Figure 7a shows the aircraft, and Figures 7b and 7c show the HH-polarized range profile of the airplane both with and without the slot array. The range profile is the time domain response to an incident sinc pulse. The sinc pulse in this example has a center frequency of 10 GHz and a bandwidth of 4 GHz, and the slot array has shorted waveguide loads. The slot scattering has an impact on



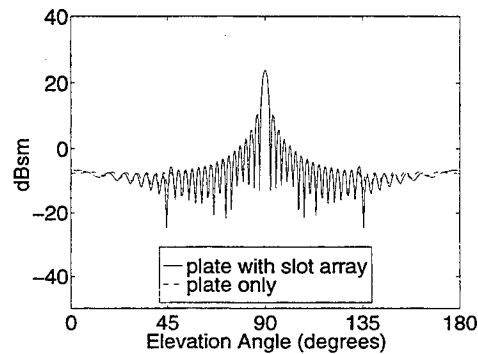
(a) *H*-plane, matched waveguide loads



(b) *E*-plane, matched waveguide loads



(c) *H*-plane, short-circuit waveguide loads



(d) *E*-plane, short-circuit waveguide loads

Figure 4: RCS of a planar slot array on a ground plate at 9.1 GHz, the working frequency of the slot array.

the range profile.

5 Conclusion

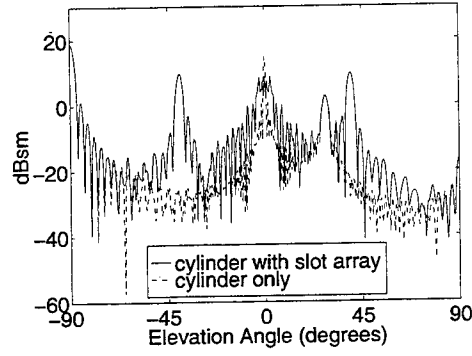
A hybrid MoM/SBR method is developed to compute the scattering from a complex, 3-D target with a slotted waveguide array antenna. Because the target is large and 3-D, the MoM alone cannot efficiently compute the scattering, and because the slots on the waveguides are small features, the SBR method alone is not accurate. The hybrid method combines the two individual methods in such a manner that the scattering can be efficiently and accurately computed. In the hybrid method, the MoM is used to model the details of the slot array, and the SBR method is used to model the electromagnetic interactions with the large, complex target. The method is validated by comparison to previously published methods. Numerical examples show the need to include a slot array model when computing the scattering from a complex target with a slotted waveguide array. The

examples also illustrate the capability of the method.

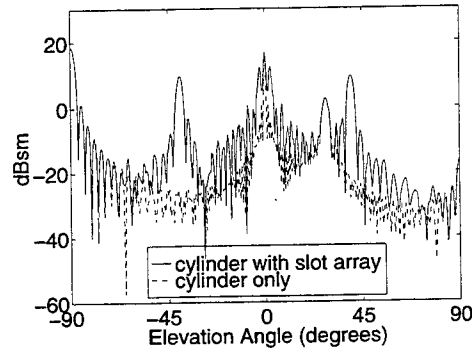
Acknowledgments: This work was supported by the Office of Naval Research under grant N00014-95-1-0848 and by NASA under grant NAG3-1474. Dr. G. X. Fan's contribution to the development of the computer code for slot array scattering is acknowledged.

References

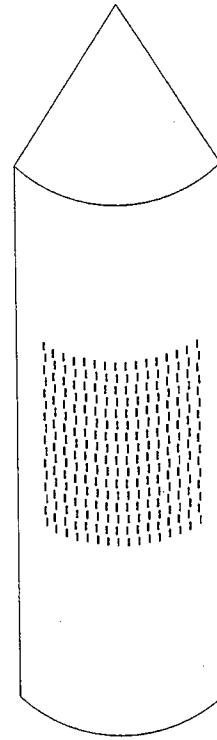
- [1] G. X. Fan and J. M. Jin, "Scattering from a cylindrically conformal slotted-waveguide array antenna," *IEEE Antennas and Propagation Society International Symposium Digest*, pp. 1394-1397, 1996.
- [2] G. X. Fan and J. M. Jin, "Scattering from a cylindrically conformal slotted-waveguide array antenna," *IEEE Trans. Antennas Propagat.*, vol. 45, no. 7, pp. 1150-1159, Jul. 1997.



(a) Matched waveguide loads

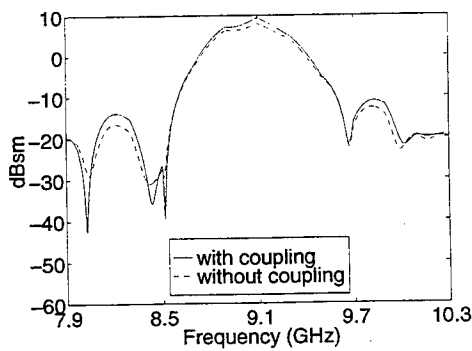


(b) Short-circuit waveguide loads

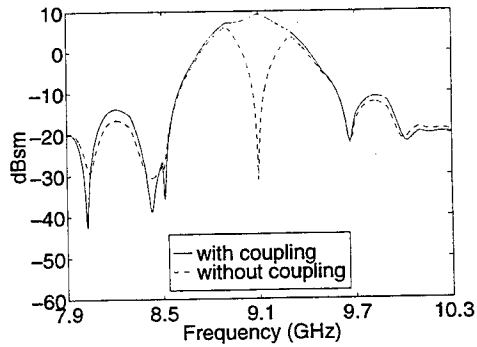


(c) Geometry

Figure 5: RCS of a conformal slot array on a cylinder with a nose cone at 9.1 GHz, the working frequency of the slot array.

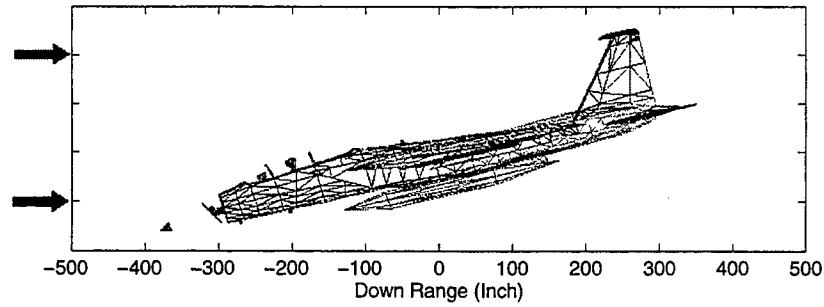


(a) Matched waveguide loads

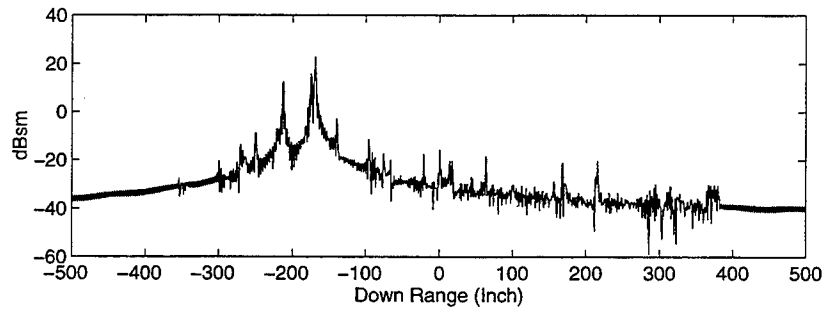


(b) Short-circuit waveguide loads

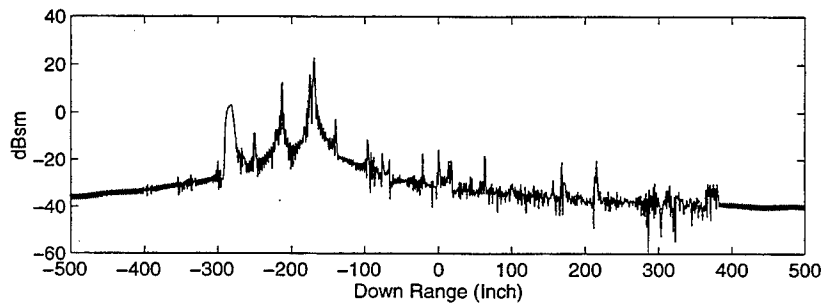
Figure 6: RCS of a conformal slot array on a cylinder with a nose cone. The scattering is computed with and without including the coupling between individual slots. Near the working frequency of the slot array (9.1 GHz), the slot coupling has a significant effect.



(a) Aircraft geometry.



(b) Range profile without slot array.



(c) Range profile with slot array.

Figure 7: Range profile of an aircraft, 15° elevation, 0° azimuth, HH-polarization, 10 GHz center frequency, 4 GHz bandwidth. The slot array has shorted waveguide loads.

- [3] J. M. Jin, S. S. Ni, and S. W. Lee, "Hybridization of SBR and FEM for scattering by large bodies with cracks and cavities," *IEEE Trans. Antennas Propagat.*, vol. 43, no. 10, pp. 1130-1139, Oct. 1995.
- [4] S. W. Lee, D. J. Andersh, D. D. Reeves, S. K. Jeng, H. Ling, Y. Chu, D. P. Sullivan, and C. L. Yu, "User manual for XPATCH," DEMACO, Inc., Champaign, IL, 1993.
- [5] D. J. Andersh, M. Hazlett, S. W. Lee, D. D. Reeves, D. P. Sullivan, and Y. Chu, "XPATCH: A high-frequency electromagnetic-scattering prediction code and environment for complex three-dimensional objects," *IEEE Antennas Propagat. Mag.*, vol. 36, no. 1, pp. 65-69, Feb. 1994.
- [6] A. D. Greenwood, S. S. Ni, J. M. Jin, and S. W. Lee, "Hybrid FEM/SBR method to compute the radiation pattern from a microstrip patch antenna in a complex geometry," *Microwave and Optical Technology Letters*, vol. 13, no. 2, pp. 84-87, Oct. 1996.
- [7] J. Chen and J. M. Jin, "Electromagnetic scattering from slot antennas on waveguides with arbitrary terminations," *Microwave and Optical Technology Letters*, vol. 10, no. 5, pp. 286-291, Dec. 1995.

Effects of Gaps Among Panels in Radio Astronomy Reflector Antennas

Giuseppe Pelosi, Roberto Coccioli, Alessio Gaggelli

Abstract— The main reflector of antennas used for radio astronomy consists of hundreds of panels among which, for various reasons, small gaps are left. In this paper, the effects of these gaps on the field scattered by the reflector are analyzed by means of an hybrid numerical technique which combines the Finite Element Method (FEM) and the Method of Moments (MoM). Numerical results pertaining to the case of an incident plane wave are presented, and the effects of the introduction of corrugations inside the gaps to minimize the power flowing through the gaps themselves are discussed.

I. INTRODUCTION

THE construction of the main reflector is the most difficult mechanical problem encountered in the realization of both radio telescope and large antennas such as those used for telecommunications in deep space. The main reflector is realized as a collection of conductive panels whose shapes are usually trapezoidal or hexagonal. The panels are left separated by a small gap to account for thermal expansion, deformations due to gravity, and to ease the construction of the reflector itself. For radio astronomy applications, the main issues are the antenna maneuverability (from a mechanical point of view) and the antenna gain over a wide frequency band (from an electromagnetic point of view).

The reflector for these antennas is usually designed assuming its surface as smoothly curved and continuous and using high frequency techniques. This approach is most useful, but unfortunately it is not able to account for the presence of gaps whose effects in the antenna performance are usually neglected [1]. More flexible and accurate numerical methods, such as the Finite Element Method (FEM) [2]-[3], can be used to simulate the presence of the gaps. Electromagnetic scattering from gaps in perfectly conducting planes has been analyzed by Gedney and Mittra [4] and Jin and Volakis [5] using a hybrid FEM/Method of Moments and FE/Boundary Inte-

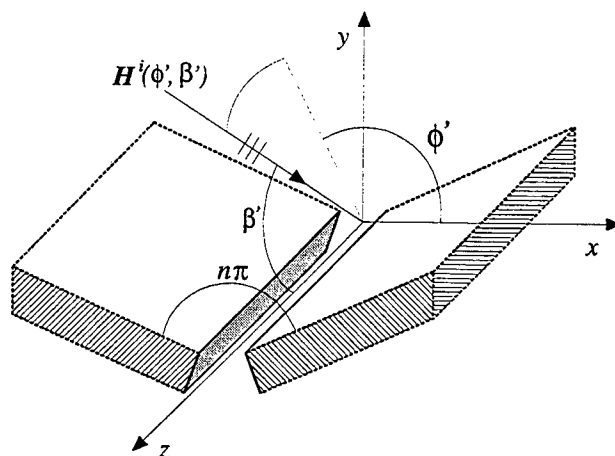


Fig. 1. Geometrical model of a gap between two tilted panels.

gral technique, respectively. The aim of this work is to extend the numerical analysis to the practical problem of gaps among tilted metallic planes as it is the case in reflector antennas.

To develop an efficient analysis tool, the hybrid technique proposed in [6] to analyze electromagnetic scattering from a wedge with cavity-backed apertures in its faces, is modified and applied to this case. Resorting to this hybrid method limits the applications of the FEM to the gap, while using high frequency techniques to simulate the large reflector. Moreover, the flexibility of the FEM allows considering the actual geometric configuration of the problem, in which the angle formed by two panels of the main reflector varies according to their location in the reflector itself, or the panels present corrugation in their edges to reduce transmission through the gap [7].

The hybrid technique employed relies on a particular formulation of the equivalence principle which implies covering the gap apertures with metallic plates. The original configuration is thus subdivided into two exterior problems, each of which is comprised of a perfectly conducting wedge, and an interior problem, consisting of a cavity with the same shape as

G. Pelosi, R. Coccioli and A. Gaggelli are with the Microwave Laboratory, Department of Electrical Engineering, University of Florence, Via C. Lombroso 6/17, I-50134 Florence, Italy.

the gap. The exterior canonical problems are formulated by exploiting the exact perfectly conducting wedge Green's function, while the more involved interior problem is treated by means of the FEM. The solutions are then joined by enforcing the continuity condition of the fields at each gap aperture. This procedure restricts the application of the FEM to the small geometric domain constituted by the gap. Furthermore, using the Finite Element Method to analyze the interior problem allows treating odd shaped gaps, such as those existing between tilted panels, which cannot be easily taken into account with other numerical techniques.

The hybrid technique employed is briefly outlined in Section II. The numerical solution implemented is described in Section III. Finally, numerical results are presented in Section IV to demonstrate both the accuracy of the technique and the effects of the gaps.

II. FORMULATION

Since the wavelength is always much smaller than the panel dimensions, the reflector surface can be locally approximated by a geometric canonical model constituted by two half-planes of finite thickness forming an angle $n\pi$ (Fig. 1). This canonical model is assumed as uniform along the z -axis, which is parallel to the half-plane edges, while ϕ' and β' denote the direction of propagation of the incident field. The following analysis has been carried out by considering the case $\beta' = \pi/2$ and an incident plane wave with unitary magnetic field parallel to the z -axis (TE_{*z*} case, $E_z^{inc} = 0$). Since the evaluation of power losses due to transmission of the field through the gap is the parameter of interest, only this polarization needs to be considered. In fact, since the width of the gap is much smaller than the wavelength over the frequency range of interest, TM_{*z*} waves do not propagate through the gap. The time dependence $\exp(j\omega t)$ has been assumed and suppressed in the following analysis.

The procedure proposed in this paper, which is an extension of that presented in [6], consists of two consecutive steps. In the first step, two fictitious surfaces Γ_1 and Γ_2 are defined by extending in free space the faces of the perfectly conducting panels, so that they intersect at Q and Q' respectively (Fig. 2). Then, the equivalence theorem is applied so as to subdivide the problem into three separate configurations (Fig. 3), simpler than the original one. Accordingly, the surfaces Γ_1 and Γ_2 are closed with a perfectly conducting cover and the three new problems are coupled through the equivalent surface magnetic current densities $M^{ext1,2}$ and $M^{int1,2}$, which are impressed on opposite sides of the

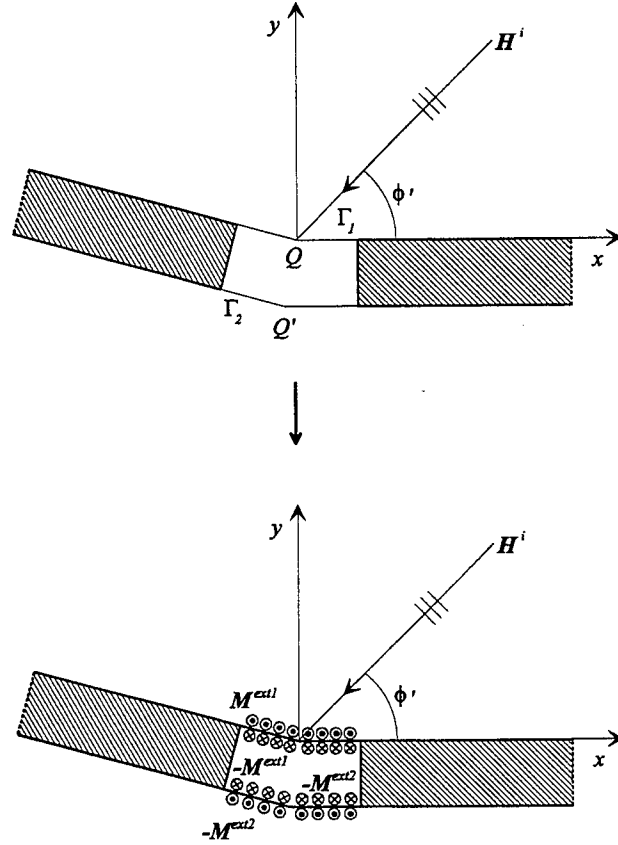


Fig. 2. Surfaces Γ_1 and Γ_2 used for the application of the equivalence principle.

surfaces $\Gamma_{1,2}$. Consequently, the original problem is reduced to: *i*) the analysis of the field in the exterior region of two complementary perfectly conducting wedges (Fig. 3a); *ii*) the analysis of the field inside the equivalent closed cavity (Fig. 3b).

For case *i*), the first exterior problem refers to the front part of the reflector and it is necessary to compute the magnetic field due to the incident plane wave and the unknown exterior magnetic current M^{ext1} at Γ_1 (Fig. 3a), defined as $M^{ext1} = \mathbf{E} \times \hat{\mathbf{n}}$, where $\hat{\mathbf{n}}$ is the outward normal unit vector to Γ_1 and \mathbf{E} is the electric field at the same surface. The second exterior problem, similar to the previous one except for the absence of excitation from the backside of the reflector, consists of the evaluation of the field radiated by the equivalent currents $M^{ext2} = \mathbf{E} \times \hat{\mathbf{n}}$. These latter radiate in the presence of the reconstructed perfectly conducting wedge with its edge in Q' (Fig. 3a). Solution of the problem *ii*) implies the computation of the field radiated by the unknown magnetic currents $M^{int1,2}$ inside the equivalent closed cavity sketched in Fig. 3b.

The second step of the procedure consists of

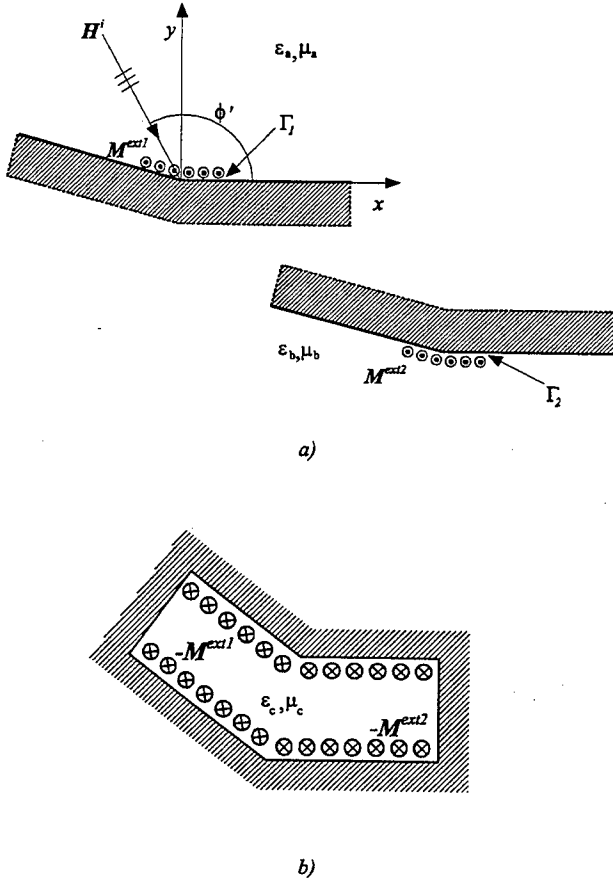


Fig. 3. a) Exterior problems. b) Interior problem. The three problems are coupled through the equivalent magnetic currents.

matching the exterior and interior problems. This can be achieved by enforcing the continuity, across the surfaces $\Gamma_{1,2}$, of the tangential component of the total electric and magnetic fields. By choosing the interior current as $M^{int1,2} = -M^{ext1,2}$, the continuity of the tangential component of the electric field is automatically guaranteed, while the boundary condition on the magnetic field must be explicitly enforced:

$$\hat{n} \times H^{ext1} = \hat{n} \times H^{int1}, \quad (1a)$$

$$\hat{n} \times H^{ext2} = \hat{n} \times H^{int2}. \quad (1b)$$

Regardless of the matching procedure adopted, the exterior magnetic field $H^{ext1} = \hat{z}H_z^{ext1}$ in equation (1a), which is defined in problem i), may be expressed as the superposition of three contributions:

$$H_z^{ext1} = H_z^{inc} + H_z^{scat} + H_z^{rad1}(M^{ext1}), \quad (2)$$

where H_z^{inc} is the incident field, H_z^{scat} is the field scattered by the equivalent wedge and $H_z^{rad1}(M^{ext1})$

is the field radiated by the exterior equivalent surface currents impressed on Γ_1 . In the second exterior problem just one term is present, that is the $H_z^{ext2} = H_z^{rad2}(M^{ext2})$. The scattered field H_z^{scat} is evaluated by using the perfectly conducting wedge Green's function expressed in terms of eigenfunctions [8], or its Uniform Geometrical Theory of Diffraction (UTD) approximation [9], depending on the distance between the observation point and the edge Q of the equivalent wedge. The evaluation of the contribution $H_z^{rad1,2}(M^{ext1,2})$, due to the equivalent magnetic current distribution, has been done only with perfectly conducting wedge Green's function because the surfaces $\Gamma_{1,2}$ are always close to the edge of the wedge. The interior magnetic field $H^{int1,2} = \hat{z}H_z^{int1,2}$ in the right hand side of equations (1a) and (1b) is produced by the interior equivalent surface current distribution impressed on $\Gamma_{1,2}$: $H_z^{int1,2} = H_z^{int1,2}(M^{int1}, M^{int2}) = H_z^{int1,2}(-M^{ext1}, -M^{ext2})$ and it is computed via the FEM solving the scalar Helmholtz equation for this field component.

Two different matching techniques, belonging to the inward-looking and outward-looking [10] categories, could be employed. Since the gaps among panels have dimensions much smaller than the wavelength in the frequency range of interest, the continuity condition in equations (1a) and (1b) can be directly solved by a point-matching formulation of the MoM, as suggested in [11]. The use of this scheme makes it necessary to explicitly calculate the contribution arising from the interior problem to the impedance matrix of the MoM. To this end, the FEM is employed to evaluate the magnetic field on $\Gamma_{1,2}$, due to each basis function used to expand the interior magnetic current distribution $M^{int1,2} = -M^{ext1,2}$ on $\Gamma_{1,2}$ itself. This procedure belongs to the inward-looking formulation class, and similarly to all the procedures of this kind, it is numerically efficient. As a matter of fact, it first solves the interior problem, which requires the inversion of a sparse, symmetric, and real (for lossless materials filling the cavity) matrix, and afterwards it matches the interior and the exterior problem. This latter task requires the solution of a system of equations whose coefficient matrix is full, but smaller than that related to the interior problem.

This matching scheme also retains the major shortcoming of inward-looking formulations: it suffers from the possible presence of non-physical resonant solutions, which may arise when solving the closed interior problem in the lossless case. However, due to the dimensions of the interior problem, this is not an issue in this application.

III. NUMERICAL IMPLEMENTATION

The inward-looking formulation for the problem leads to the standard MoM matrix equation

$$[\mathbf{Y}^{int1} + \mathbf{Y}^{ext1} + \mathbf{Y}^{int2} + \mathbf{Y}^{ext2}] \cdot \mathbf{V} = \mathbf{I}, \quad (3)$$

where $\mathbf{Y}^{int1,2}$ and $\mathbf{Y}^{ext1,2}$ account for the contributions to the magnetic field at $\Gamma_{1,2}$ coming from the interior and the exterior problem, respectively. Furthermore, in equation (3), \mathbf{I} is the excitation column vector, due to the incident plus scattered fields at the aperture opening Γ_1 , while \mathbf{V} is the column vector of the unknown coefficients of the basis functions used to expand the equivalent magnetic current distribution. Careful attention must be paid in choosing this set of basis functions. As a matter of fact, the transverse components of the electric field are singular [12], [13] at the two edges of each of the thick panels delimiting the gap and this singularity is apparently also present in the equivalent magnetic current. For this reason, the four basis functions centered at the ends of the fictitious surfaces Γ_1 and Γ_2 have been chosen with a singular behavior of the kind $-1/(2\sqrt{\rho})$, where ρ is the distance from the edge of the wedge. Indeed, this is the kind of singularity that the transverse component of the electric field exhibits at the proximity of a 90° perfectly conducting wedge [13]. These four basis functions, as well as all the other, span a subsection of Γ_1 and Γ_2 and are built in such a way that they vanish at all the other nodal points on Γ_1 and Γ_2 belonging to the same subsection. All the other basis functions are polynomials which, on the surfaces Γ_1 or Γ_2 , coincide with the shape functions used for the FEM discretization of the interior problem.

The magnetic field required to calculate each entry of the matrix $\mathbf{Y}^{int1,2}$ is obtained by applying the finite element method with second order nodal elements to the interior region. The FEM has been chosen because it allows rather general equivalent cavity configurations, such as those arising in case of arbitrarily tilted panels, corrugations in the thick side of the panels, the presence of dielectric material, and so on. It is important to remark that the construction of this $(N \times N)$ matrix, which needs the solution of N interior problems (where N is the number of basis functions used to expand all the magnetic equivalent currents on Γ_1 and Γ_2), can be done just once for each gap configuration, regardless the direction of the incident wave.

$\mathbf{Y}^{ext1,2}$ in equation (3) results from the term $\mathbf{H}_z^{rad1,2}(\mathbf{M}^{ext1,2})$, and is evaluated by referring to the equivalent problem of a wedge illuminated by a magnetic line source. Also the construction of this matrix

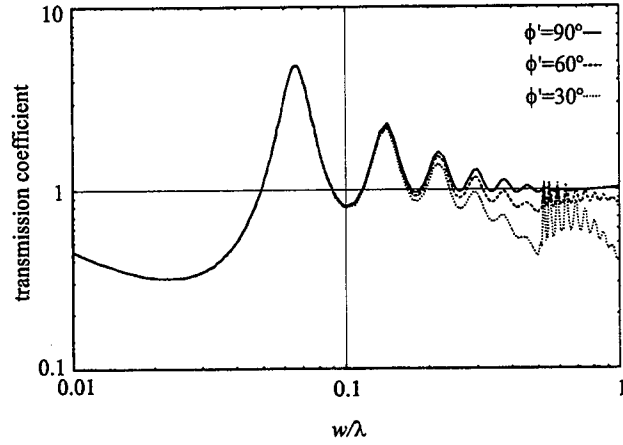


Fig. 4. Transmission coefficient through a 0.05 cm wide gap in a 0.3 cm thick conducting panel for different angles of incidence.

can be done just once for a gap with a specified aperture, and subsequently used for any direction of the incident electromagnetic field.

IV. NUMERICAL RESULTS

To validate the code, previously published results and measurements have been considered. Fig. 4 shows the transmission coefficient through a slot with width $w = 0.05$ cm in a 0.3 cm thick conducting sheet. Computations have been performed for three different values of the incidence angle, and results agree very well with those reported in [4]. It should be noted that the transmission coefficient has been defined as the ratio between the power flowing through the gap and that through the same surface located in the free space due to a plane wave impinging at $\phi' = 90^\circ$, and this accounts for the values above unity in Fig. 4.

A second comparison has been made analyzing a more involved configuration, for which measured results are available in the literature [14]. It is comprised of a gap with length 3.6 mm between two perfectly conducting panels 5 mm thick. Each panel has a corrugation 3 mm wide and 7.5 mm deep. Fig. 5 shows, for a such configuration, the transmission coefficient versus frequency, where the transmission coefficient is defined as the ratio of the power flowing through the gap with the corrugation and without. When the panels are aligned ($n = 1$), the measured transmission coefficient from reference [14] (dots) agrees well with the computed one (dashed line). It can be seen that, at a frequency close to the resonant frequency of the corrugations, the transmission coefficient becomes quite low, increasing the antenna performance. Fig. 5 also shows the transmis-

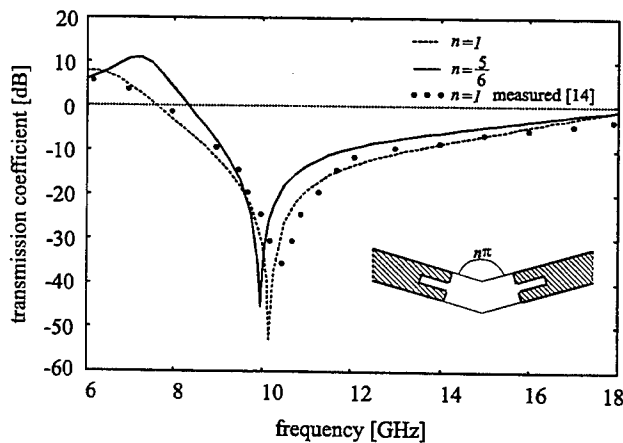


Fig. 5. Transmission coefficient through a slit between two panels 5 mm thick. Each panel presents a corrugation 7.5 mm deep and 3 mm wide. $\phi' = 75^\circ$. Dashed line: $n = 1$, computed results; dots: $n = 1$, measured results [14]; continuous line: $n = 5/6$, computed results.

sion coefficient versus frequency when the two panels are tilted of an angle equal to 150° ($n = 5/6$, continuous line). The length of the gap Γ_1 is kept constant to 3.6 mm, but since the opposite faces of the panels are moved farther from each other, the resonance frequency of the corrugated gap decrease, as shown by the computed results.

Fig. 6 shows the amplitude of the magnetic field longitudinal component H_z inside the gap relative to the case $n = 5/6$ of Fig. 5. The incident field has a frequency of 10 GHz and for such value the corrugation depth is equal to $\lambda/4$. Hence, the corrugations create an equivalent magnetic wall along the thick side of the panels, which act as a short circuit on the magnetic field. As matter of fact, Fig. 6 shows maxima of magnetic field at the end of the corrugations and minima at their entrance. The low level of the magnetic field at the surface Γ_2 accounts for the minimum in the transmission coefficient through the aperture. Although introducing the corrugation is effective only in a narrow band, and thus it is not possible to optimize the radio astronomy reflector antenna performance in the whole frequency band of interest, corrugations may be used to optimize the antenna in specific relatively narrow bands as, for instance, those also used for telecommunication purposes.

The third configuration considered is comprised of a 6 mm wide gap between 2 mm thick panels tilted at an angle of 170° . These parameters have been measured directly on the parabolic radio astronomy reflector antenna of the Italian National Research Council located at Medicina (Bologna, Italy).

In Fig. 7, the equivalent magnetic currents at the

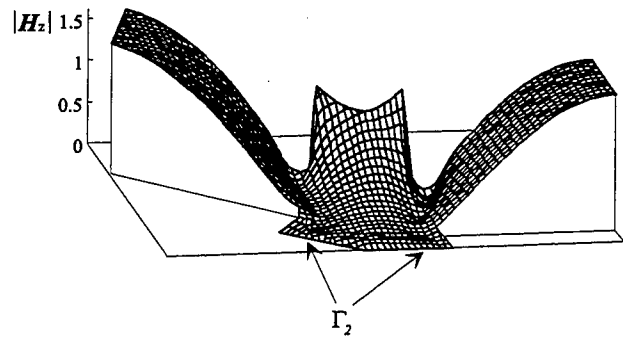


Fig. 6. Amplitude of the magnetic field longitudinal component inside a corrugated gap between two panels 5 mm thick and tilted at 150° . Each panel presents a corrugation 7.5 mm deep and 3 mm wide. $\phi' = 75^\circ$, $f = 10$ GHz.

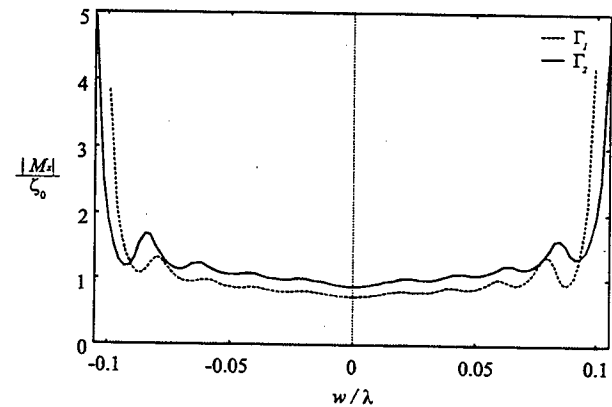


Fig. 7. Normalized amplitude of equivalent magnetic current distributions at surfaces Γ_1 and Γ_2 for a slit 6 mm wide and 2 mm deep between two panels tilted at 170° . The incident plane wave impinges at an angle $\phi' = 85^\circ$ and has a frequency equal to 10 GHz.

apertures Γ_1 and Γ_2 are plotted. The incident plane wave has a frequency equal to 10 GHz and impinges at an angle of $\phi' = 85^\circ$. At both the apertures, the equivalent current distribution is almost uniform in the central part, while it exhibits the expected singularity near the edges of the panels. These equivalent magnetic currents provide an almost isotropic radiation pattern. This means that radiation incoming from the backside of the reflector is received through the gap, thus increasing the antenna noise temperature.

Further interesting results pertains to the field scattered by the two panels. Fig. 8 shows the normalized amplitude of the scattered field at a distance of $\rho = 10\lambda$ from the reconstructed wedge Q versus the observation angle. The two panels are illuminated by a plane wave impinging again at $\phi' = 85^\circ$ but with a frequency equal to 50 GHz. The dotted

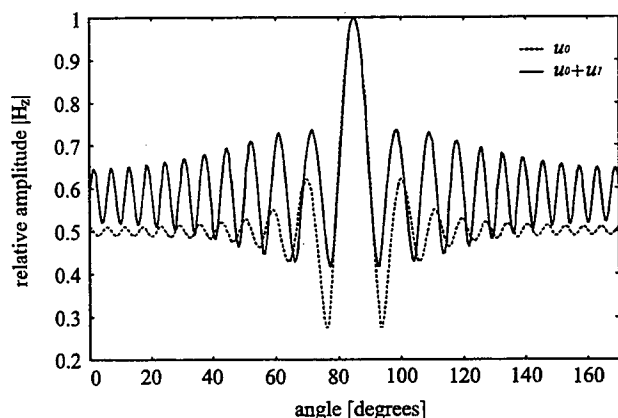


Fig. 8. Normalized amplitude of the magnetic field at a distance $\rho = 10\lambda$ from the reconstructed wedge Q of two panels tilted at 170° . $\phi' = 85^\circ$; $f = 50$ GHz. Dots: continuous panels, the presence of the gap is neglected. Continuous line: the presence of a slit 6 mm wide and 2 mm deep is considered.

line refers to the field computed by neglecting the presence of the gap. This field, denoted as u_0 , represents a zero-th order solution. The first order additive contribution u_1 is given by the field radiated by the equivalent magnetic current computed with the technique proposed. The field $u_0 + u_1$ is shown in Fig. 8 with a continuous line. It is seen that in the backscattering direction there are no differences between the two patterns, while the contribution u_1 of the gap strongly affects the radiation pattern in the other directions, and this effect increases with frequency.

V. CONCLUSION

The effects of gaps among panels comprising the main reflector of large antennas used for radio astronomy have been studied by means of a hybrid numerical technique which combines the FEM and the MoM. The technique is based on a particular application of the equivalence principle which allows the reduction of the original configuration to three simpler problems: two exterior canonical problems and one interior problem. The first two can be treated by exploiting the exact Green's function or its approximation in the framework of the Uniform Geometrical Theory of Diffraction, the latter can be efficiently solved using the FEM. Due to the flexibility of the FEM, it is possible to analyze arbitrary configurations in an attempt to find optimized gap configurations able to improve the antenna performance.

The code realized in this work represents a first step toward a more sophisticated tools able to evaluate the contribution to the phase error at the antenna opening due to the presence of gaps between panels.

This contribution, as shown by the results presented, may be significant.

ACKNOWLEDGMENT

The authors wish to thank Dr. E. Paoletti of the University of Florence for useful discussions and help with computations.

REFERENCES

- [1] G. Cortés Medellín, P. F. Goldsmith, "Analysis of active surface reflector antenna for a large millimeter wave radio telescope," *IEEE Trans. Antennas Propagat.*, vol. 42, no. 2, pp. 176–183, 1994.
- [2] P. P. Silvester, G. Pelosi, *Finite Elements for Wave Electromagnetics*. IEEE Press, New York, 1994.
- [3] P. P. Silvester, R. L. Ferrari, *Finite elements for electrical engineers*. 3rd edition. Cambridge, U.K.: Cambridge University Press, Cambridge, 1996.
- [4] S. D. Gedney, R. Mittra, "Electromagnetic transmission through inhomogeneously filled slots in a thick conducting plane - arbitrary incidence," *IEEE Trans. Electromagn. Compat.*, vol. 34, no. 4, pp. 404–415, 1992.
- [5] J. M. Jin, J. L. Volakis, "Electromagnetic scattering by and transmission through a three-dimensional slot in a thick conducting plane," *IEEE Trans. Antennas Propagat.*, vol. 39, no. 4, pp. 543–550, 1991.
- [6] G. Pelosi, R. Coccioli, G. Manara, A. Monorchio, "Scattering from a wedge with cavity backed aperture in its faces and related configurations: TE case," *IEE Proc.-Microw. Antennas Propagat.*, vol. 142, no. 2, pp. 183–188, April 1995.
- [7] P. S. Kildal, L. Steen, P. Napier, "Reduction of scattering from gaps between reflector antennas panels by using artificially soft edges," *Antennas and Propagation Society Symposium 1991 Digest*, London, Ont., Canada, 24–28 June 1991, vol. 3, pp. 1316–1319, 1991.
- [8] R. F. Harrington, *Time Harmonic Electromagnetic Fields*. McGraw-Hill, New York, 1961.
- [9] R. G. Kouyoumjian, P. H. Pathak, "A uniform geometrical theory of diffraction for an edge in a perfectly conducting surface," *Proc. IEEE*, vol. 62, pp. 1448–1461, 1974.
- [10] L. W. Pearson, A. F. Peterson, L. J. Bahrmassel, R. A. Whitaker, "Inward-looking and outward-looking formulations for scattering from penetrable objects," *IEEE Trans. Antennas Propagat.*, vol. 40, no. 6, pp. 714–720, 1992.
- [11] X. Yuan, D. R. Lynch, J. W. Strohbehn, "Coupling of finite element and moment methods for electromagnetics scattering from inhomogeneous objects," *IEEE Trans. Antennas Propagat.*, vol. 38, no. 3, pp. 386–393, 1990.
- [12] J. Meixner, "The behavior of electromagnetic fields at edges," *IEEE Trans. Antennas Propagat.*, vol. 20, no. 4, pp. 442–446, 1972.
- [13] J. Van Bladel, "Field singularities at metal-dielectric metal wedges," *IEEE Trans. Antennas Propagat.*, vol. 33, no. 4, pp. 450–455, 1985.
- [14] J. Carlsson, P. S. Kildal, "Transmission through corrugated slots," *IEEE Trans. Electromagn. Compat.*, vol. 37, no. 1, pp. 114–121, 1995.

Some Experiences in using NEC2 to Simulate Radiation from Slots on Cylinders

S. H. H. Lim, H. E. Green and C. E. Brander

Institute for Telecommunications Research

University of South Australia

The Levels, South Australia 5095, Australia

stanley@spri.levels.unisa.edu.au

ABSTRACT

A numerical method based on use of the NEC2 code has been used to study radiation from a slot in the surface of a conducting cylinder and the results used in a comparison with the eigenfunction series solution. The two cases of an axial and circumferential slot have been taken as representative between them of the more general case of an inclined slot. In the case of a circumferential slot, truncation of the cylinder to finite length has been found in all cases to lead to numerical and analytic results which are in poor agreement and this has been accounted for with an argument based on the geometrical theory of diffraction. However this alone is not enough to explain what is observed with axial slots where, for small cylinders, agreement of the two approaches is good but fails for larger cylinders. It is postulated that this is due to excitation of waveguide modes on the inside of the larger cylinders and the result confirmed by closing the ends of the cylinder in the NEC2 model with a system of radial wires, when agreement is again restored.

1. INTRODUCTION

Analytical studies of radiation from slots in infinite conducting cylinders have been made by a number of authors [1], [2], [3], [4], [5]. However, when as must necessarily be the case in practice, the cylinder in which the slot is cut is of finite length, to find the radiation pattern, resort has to be made to either numerical methods or some approximate technique of which, for a sufficiently large cylinder, the geometric theory of diffraction might be an example.

This paper presents some experiences with a numerical means of determining the radiation pattern of a narrow slot cut in the (assumed infinitesimally thin) wall of a hollow, perfectly conducting, finite, circular cylinder. The application which we have in mind is personal satellite wireless mobile communications and our interest will be with narrow slots, the length of which are no more than comparable with the half wavelength (resonant or near resonant slots).

The paper is arranged as follows. Section 2 reproduces the eigenfunction expansion of the electric field radiated by an arbitrarily oriented slot cut in an infinite cylinder. Next the radiation pattern of a slot cut in an otherwise similar finite cylinder is generated using the NEC2 package and compared with the eigenfunction solution and in the following section there is a discussion of the notable points of difference and the reasons for them. The paper concludes with a summary of its findings.

2. AN ARBITRARILY ORIENTED SLOT ON AN INFINITE CYLINDER

When the cylinder is of infinite length, an analytical solution for radiation from an arbitrarily oriented slot is possible in terms of cylindrical wave functions and has been known for a considerable time [4]. Figure 1 shows a coordinate system in terms of which it is convenient to write down the eigenfunction series expansion. The centre of the slot lies in the XOZ coordinate plane with OX passing through its centre, which is at $(a, 0, 0)$, a being the radius of the cylinder. The slot is excited by a voltage V applied across it.

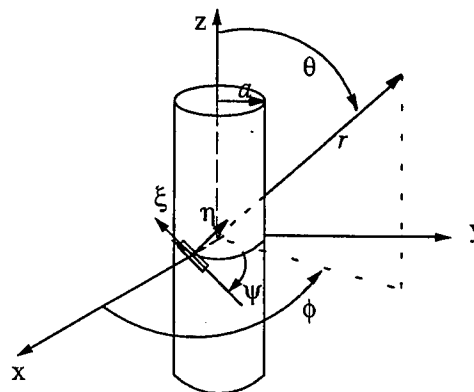


Figure 1 Geometrical parameters

With respect to local coordinates (η, ξ) drawn along the centrelines of the slot, it is assumed that its electric field distribution is oriented parallel to the η direction, in

which it is also uniform, while in ξ it is sinusoidal. For this configuration, the series solutions for the two spherical components of the radiation field are

$$E_\theta = \frac{-V_0 \cos \psi e^{-jkr}}{2\pi^2 r \sin \theta} \sum_{n=-\infty}^{\infty} \frac{j^{n+1} e^{-jn\phi} I_n P_n}{H_n^{(2)}(ka \sin \theta)} \quad (1)$$

$$E_\phi = \frac{V_0 e^{-jkr}}{2\pi^2 r} \sum_{n=-\infty}^{\infty} \frac{j^n e^{-jn\phi} I_n P_n}{H_n^{(2)}(ka \sin \theta)} \times \left[-\sin \psi + \frac{n \cos \psi \cos \theta}{ka \sin^2 \theta} \right] \quad (2)$$

where

$$I_n = \frac{2\pi a \cos \frac{Kn l}{2a}}{\left(\frac{\pi a}{l}\right)^2 - K_n^2}$$

$$P_n = \frac{\sin\left(\frac{(ka \cos \psi \cos \theta - n \sin \psi)w}{2a}\right)}{\left(\frac{(ka \cos \psi \cos \theta - n \sin \psi)w}{2a}\right)}$$

$$K_n = ka \sin \psi \cos \theta + n \cos \psi$$

ψ is the inclination angle, l is the slot length, w is the slot width and k is the free space wavenumber.

Getting to the essentials of the problem is best facilitated by considering the two special cases $\psi = 0$ and $\psi = 90^\circ$, when the slot is respectively circumferential and axial. Calculations for the radiation pattern in the $\theta = 90^\circ$ plane (the XOY plane) for these two cases are shown in Figures 2, 3 and 4.

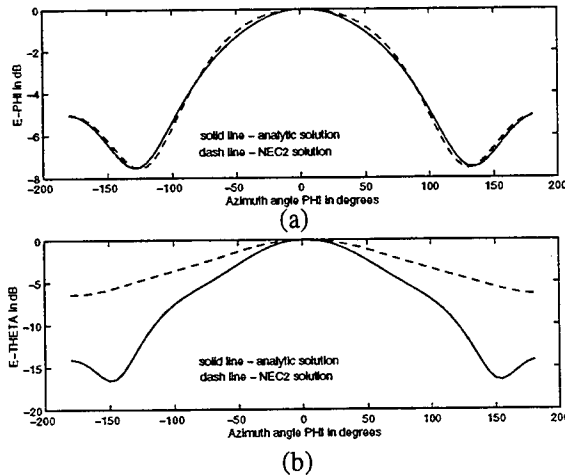


Figure 2. Comparison of normalised far-field pattern in the $\theta=90^\circ$ plane obtained using an analytic solution and NEC2 for $f=2\text{GHz}$, $ka=0.8$, $w=0.05\lambda$, $L=\lambda$ and (a) an axial with $l=0.5\lambda$ and (b) a circumferential slot with 0.3λ .

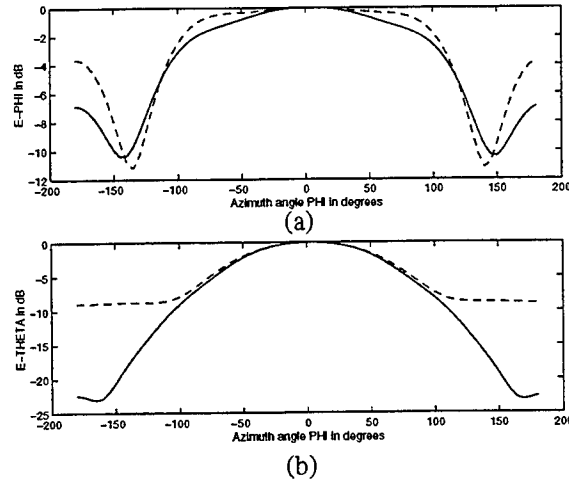


Figure 3. Comparison of normalised far-field pattern in the $\theta=90^\circ$ plane obtained using an analytic solution and NEC2 for $f=2\text{GHz}$, $ka=1.5$, $w=0.05\lambda$, $L=\lambda$ and (a) an axial with $l=0.5\lambda$ and (b) a circumferential slot with $l=0.3\lambda$.

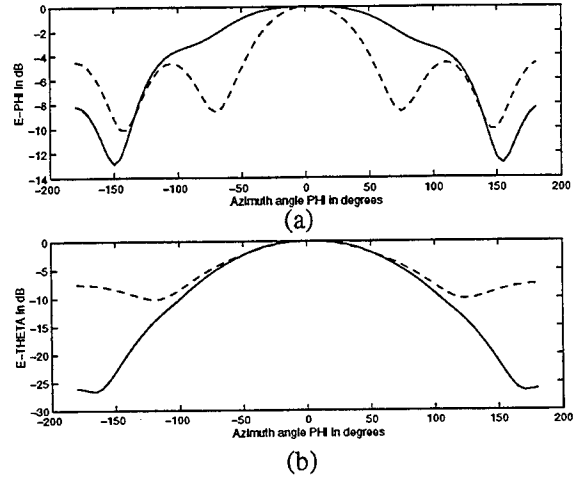


Figure 4. Comparison of normalised far-field pattern in the $\theta=90^\circ$ plane obtained using an analytic solution and NEC2 for $f=2\text{GHz}$, $ka=2$, $w=0.05\lambda$, $L=\lambda$ and $l=0.5\lambda$ for (a) an axial and (b) a circumferential slot respectively.

3. NUMERICAL SOLUTION OF THE FINITE CYLINDER

The NEC2 package has been used to solve the same problems for a finite cylinder. NEC2 uses a wire grid approximation for the cylinder which, when cut and unfolded into a developed view, is the simple rectangular mesh shown in Figure 5. In modelling the axial slot, the spacing between the vertical wires is chosen to be the desired slot width. The same is done for the horizontal wires in the case of the circumferential slot.

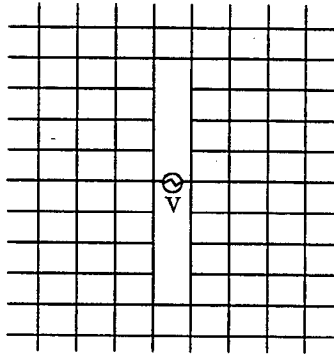


Figure 5. NEC2 Wire Grid Model

Three different cylinder sizes were considered for each slot orientation. These were $ka = 0.8, 1.5$ and 2.0 . In each case the cylinder length was chosen as one wavelength. Figures 2, 3 and 4 superimpose the normalised (for each pattern, to its own maximum) NEC-derived and analytic solutions. The choice to compare normalised patterns was made as it renders differences between the two most easily apparent. However, it is to be remarked that where there is strong agreement, as in Figures 2a and 3a for example, at maximum, there is less than 0.5 dB displacement between the two absolute patterns. Not surprisingly, where the correlation is poor, as in Figures 2b and 3b, differences between maxima of up to 3 dB are in evidence. It is interesting to compare the normalised patterns to seek reasons for observed discrepancies.

4. DISCUSSION

The geometric theory of diffraction [6] provides a good paradigm in which to look for the answers. Especially for the $ka = 0.8$ case, the cylinders which we have chosen would lie at the lower end of the range for which this theory can be expected to give accurate answers but, at least for the purposes of qualitative reasoning, that is not of great account.

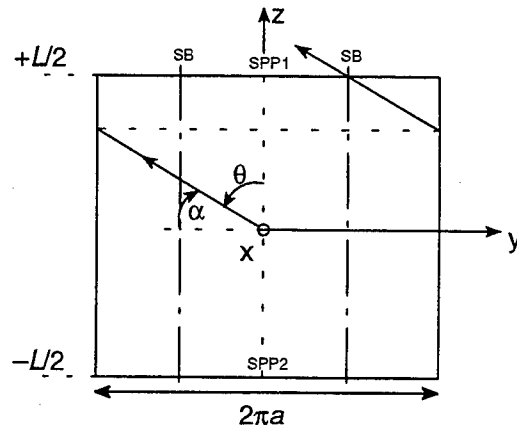
In addition to direct radiation from the slot, on the surface of the cylinder it will also give rise to a family of creeping waves which will travel over helical paths (straight lines on a developed view), shedding tangential rays as they progress. Thus, for example, contributions to the radiation in the XOZ plane will emanate from the shadow boundaries formed by the lines of intersection of the plane YOZ with the cylinder.

When the cylinder is of finite length, these helical paths will eventually intersect with its open ends, when two things will occur.

One is that creeping rays which would have reached the far field point by being shed from parts of the cylinder now removed by truncation can no longer do so. So far

as radiation in XOZ is concerned, looking at the developed view of the cylinder shown in Figure 6, we see that creeping waves which reach the shadow boundary by making the minimum transit of three quarters of a turn around the cylinder – and these, rather than the more frequently encircling creeping waves which will also be present, are those which make the major contribution to the radiation field – can only be present in $90 - \alpha < \theta <$

$90 + \alpha$, where $\alpha = \text{atan}\left(\frac{L}{(3\pi a)}\right)$, the neighbourhood of the XOY plane. More of these creeping waves will be included by using a longer cylinder.



notes: SB refers to shadow boundary
SPP1 and SPP2 are the stationary phase points

Figure 6. Developed view of the slotted cylinder

The other effect is that there will be an edge diffraction contribution from the open ends of the cylinder, the dominant part of which will come from certain stationary phase points which can be located by use of Fermat's principle [6]. For radiation into the positive XOZ half plane ($\phi = 0^\circ$) these will be the points of intersection of that half plane with the ends of the cylinder, immediately above and below the slot. For other values of ϕ in $\theta = 90^\circ$, the stationary phase points will move circumferentially around the top and bottom edges of the cylinder in sympathy with ϕ (but through an angle which depends on the length of the cylinder and which is always less than ϕ).

The degree to which these perturbations can be expected to bring about significant deviation from the infinite cylinder result will vary markedly in the case of an axial as against a circumferential slot. The reason for this is not hard to see. In both cases the slot will behave like a magnetic dipole laid on the surface of the cylinder and the source pattern of a dipole is maximum transverse to its axis and zero along its length. In the case of an axial slot, this means that not only are the stationary phase points weakly illuminated, the more so for longer cylinders and indeed not at all for $\phi = 0^\circ$, but the part of the family of creeping waves which is truncated off, being launched at angles closer to the dipole axis, is also weak-

er. With the circumferential slot, exactly the opposite is true.

Figure 7 shows the effect of increasing cylinder length for the case of $ka = 2.0$. In the light of the above it is no mystery that there is poor agreement between the eigenfunction series and the NEC2 solution in the case of a circumferential slot.

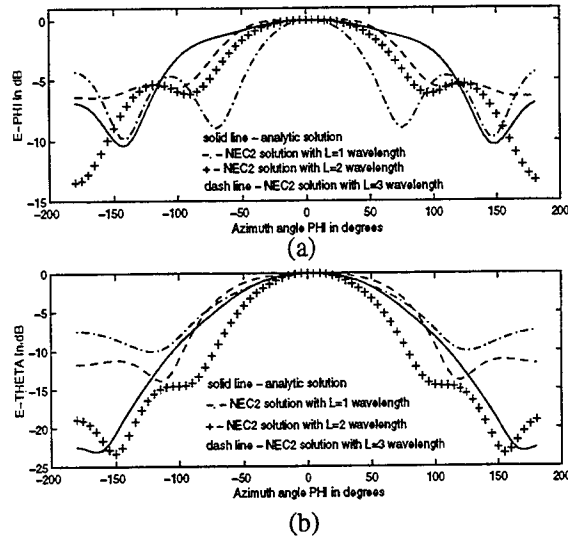


Figure 7. Comparison of normalised far-field pattern in the $\theta=90^\circ$ plane obtained using an analytic solution and NEC2 for $f=2\text{GHz}$, $ka=2$, $w=0.05\lambda$, $l=0.5\lambda$ and $L=1\lambda$, 2λ and 3λ for (a) an axial and (b) a circumferential slot.

The problem, however, is still not entirely solved for the axial slot. It is only with the smallest diameter cylinders that good agreement is obtained. As the cylinder becomes larger, there must be an expectation that both the slot directly and edge diffraction at the ends will excite propagating waveguide modes inside it. Power coupled into these modes will be conveyed without attenuation to the open ends of the cylinder, from where it will be radiated to interfere with the fields produced by the various mechanisms already identified. When this has the possibility of happening can be determined by looking at the cutoffs of the modes in cylindrical waveguide [7].

The TE_{11} mode has the lowest cutoff at $k_c a = 1.841$ and there is no other mode, TE or TM, which has a cutoff below $k_c a = 2.405$. In the case of the $ka = 0.8$ cylinder, we are therefore well away from any possibility of a waveguide mode being present to upset the agreement between the eigenfunction and NEC2 solutions. The opposite, of course, is true with $ka = 2.0$ and is held to explain the disagreement. The $ka = 1.5$ case is more interesting. Taken at face value, the evidence is that the cylinder is below waveguide cutoff, when there should be no problem. However, it is close enough to cutoff that, with a relatively short cylinder, evanescent fields will still reach the open ends of the cylinder, probably in sufficient strength to account for some of the minor discrepancies seen in Figure 3a.

A way of testing these conclusions is to repeat the NEC2 solution with a closed ended cylinder, modelled in this case by a system of radial wires across each end. This will leave nearly everything else in the problem intact (save that diffraction at the ends is now from a right angle wedge rather than a half plane) while eliminating any contribution from waveguide modes. Figure 8a makes the point; directly any possibility of a waveguide contribution is removed, agreement in the axial case between the eigenfunction and NEC2 solutions is much improved.

None of this, of course, is to say that, in the case of the circumferential slot, waveguide modes will not exist or also have the possibility of contributing to discrepancies between the eigenfunction and numerical solutions, but it is to say that in this instance, complete salvation is not to be had simply by their removal. As Figure 8b shows, while the situation is ameliorated, large discrepancies remain.

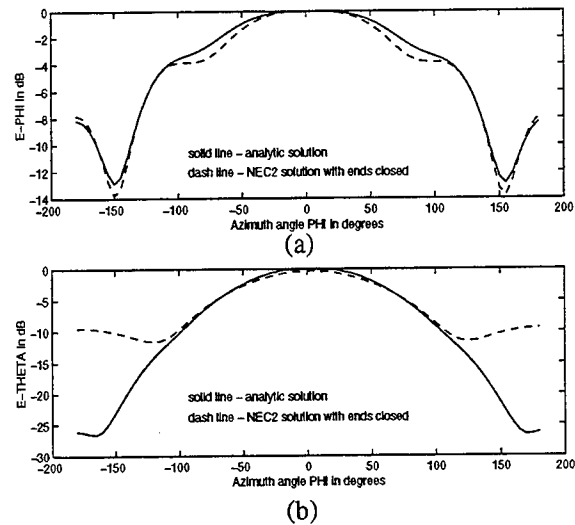


Figure 8. Comparison of normalised far-field pattern in the $\theta=90^\circ$ plane obtained using an analytic solution and NEC2 for $f=2\text{GHz}$, $ka=2$, $w=0.05\lambda$, $l=0.5\lambda$ and $L=1\lambda$ for (a) an axial and (b) a circumferential slot.

5. CONCLUSION

A wire grid model based on the NEC2 code has been developed with which to simulate radiation from near resonant slots cut in the surface of a finite length conducting cylinder and the results compared with those obtained from an associated analytic solution which assumes an infinitely long cylinder. Discrepancies between the two have been explained using an argument based on the geometrical theory of diffraction which lends credibility to the numerical solution and confirms its usefulness for the study of radiation from arbitrarily oriented slots, which are believed to have potential application in the area of personal mobile satellite wireless communications.

An interesting intervention in the final result from waveguide modes propagating within the cylinder but not intended to be part of the model has also been observed. This serves to emphasise a need constantly to be on guard to ensure that a model is chosen which simulates only the problem of interest and nothing more. This observation may also make some contribution to comment which has appeared in NEC user-group e-mail discussions (NEC-LIST) on the apparent inability of NEC2 based solutions to match those obtained analytically for larger diameter cylinders.

6. ACKNOWLEDGMENT

The authors wish to thank Jerry Burke for seminal advice.

REFERENCES

- [1] S. Silver and W. K. Saunders, "The External Field Produced by a Slot in an Infinite Circular Cylinder", *Journal of Applied Physics*, Vol. 21, No. 2, Feb 1950, Pages 153–158.
- [2] O. C. Haycock and F. L. Wiley, "Radiation Patterns and Conductance of Slotted-Cylinder Antennas", *Proceedings of the IRE*, Mar 1952, pages 349–352.
- [3] G. Sinclair, "The Patterns of Slotted-Cylinder Antennas", *Proceedings of the IRE*, Dec 1948, pages 1487–1492.
- [4] H. L. Knudsen, "Antennas on Circular Cylinders", *IRE Transactions on Antennas and Propagation*, Dec 1959, pages S361–370.
- [5] L. L. Bailin, "The Radiation Field Produced by a Slot in a Large Circular Cylinder", *IRE Transactions on Antennas and Propagation*, Jul 1955, pages 128–137.
- [6] R. C. Hansen (ed), *Geometric Theory of Diffraction*, IEEE Press, New York, 1981.
- [7] R. E. Collin, *Foundations for Microwave Engineering*, McGraw-Hill Book Company, New York, 1966.

A Kirchhoff integral approach for decimetric radiowave propagation in urban areas

L. Pisani, F. Rapetti, C. Vittoli

Centro di Ricerca, Sviluppo e Studi Superiori in Sardegna (CRS4)
Via N. Sauro 10, 09123 Cagliari, Italy.

Abstract

We consider a three-dimensional approach based on the Kirchhoff's method in order to predict electromagnetic waves propagation in urban environments. In particular, we are interested here in the evaluation of the electromagnetic field on very large three-dimensional domains (typically with linear dimensions of the order of hundreds of meters) generated by a high frequency source (typically of the order of 1GHz which corresponds to a wavelength of about 30 centimeters). Some numerical tests and comparisons with experimental measurements have been done to validate this approach.

1 Introduction

Efficient planning of mobile communication systems is based on an accurate determination of the coverage region of the antenna. In urban environments, this can be quite complicated, since electromagnetic waves are absorbed, reflected, transmitted and diffracted by buildings. The subject of our research activity is the analysis and development of simulation tools to effectively predict the propagation of the electromagnetic waves and the antenna coverage in three-dimensional urban domains which have huge dimensions with respect to the wavelength.

Techniques used to solve this problem in a reasonably fast way include ray tracing (Ikegami *et al.*, 1991, Rossi *et al.*, 1992, Kürner *et al.*, 1993, Rizk *et al.*, 1994) and two-dimensional Transmission Line Matrix (TLM) (Luthi *et al.*, 1996). We propose a three-dimensional approach based on the Kirchhoff integral method. The presence of multiple reflections has led to implement Kirchhoff's method using an iterative procedure where each iteration corresponds to a reflection on a surface. In addition, a number of approximations have been introduced to limit the computational complexity.

This approach is validated through numerical comparisons with experimental measurements. Further results related to the convergence and time scaling of the method as well as its application to determine the antenna coverage in urban environments are presented and discussed.

2 The vector Kirchhoff integral relation

In this section we review the theoretical basis of the vector Kirchhoff integral relation (Jackson, 1975, pages 432-435).

Suppose that the vector field \mathbf{E} has harmonic time dependence $e^{-i\omega t}$. When the field sources are outside the volume V , the field \mathbf{E} satisfies the vector Helmholtz wave equation inside V ,

$$(\nabla^2 + k^2)\mathbf{E}(\mathbf{x}) = 0 \quad (1)$$

where $k = \frac{\omega}{c}$ and c is the wave propagation velocity. By applying the divergence theorem

$$\oint_V \nabla dV = \oint_{S_V} \mathbf{n} d\sigma \quad (2)$$

it is easy to see that, when equation (1) is verified, the following relation is an identity:

$$\mathbf{E}(\mathbf{x}) = \oint_{S_V} \left[\mathbf{E}(\mathbf{n}' \cdot \nabla') \frac{e^{ikr}}{4\pi r} - \frac{e^{ikr}}{4\pi r} (\mathbf{n}' \cdot \nabla') \mathbf{E} \right] d\mathbf{x}' \quad (3)$$

In (3) $\mathbf{r} = \mathbf{x} - \mathbf{x}'$, the point \mathbf{x} is inside the volume V bounded by the surface S_V and the unit normal \mathbf{n}' is directed into the volume V .

Equation (3), which is known as the Kirchhoff integral, expresses the electric field \mathbf{E} at a point \mathbf{x} inside a

closed volume V in terms of the values of the field and its normal derivative on the boundary surface S_V . By using Maxwell equations, we can rewrite equation (3) in terms of the electric and magnetic fields \mathbf{E} and \mathbf{B} :

$$\mathbf{E}(\mathbf{x}) = \frac{i}{4\pi} \oint_{S_V} \frac{e^{ikr}}{r} \left[\mathbf{k} \times (\mathbf{n}' \times \mathbf{E}) \left(1 + \frac{i}{kr} \right) + k(\mathbf{n}' \times \mathbf{B}) - k(\mathbf{n}' \cdot \mathbf{E}) \left(1 + \frac{i}{kr} \right) \right] dx' \quad (4)$$

For the Helmholtz equation (1) to be satisfied inside V , the medium contained in V must be homogeneous. Therefore, when we need to evaluate the electromagnetic scattering from objects which have a dielectric constant $\epsilon \neq \epsilon_0$, we can identify V with the free space between the scatterers. The boundary surface S_V of V is taken equal to $S \cup S_\infty$ where S is the surface of the scattering objects and S_∞ is the surface "at infinity". It can be proven (Jackson, 1975, pages 433-434) that the integral over S_∞ vanishes; so the integral in (4) can be computed only over S .

It is useful to specialize (4) to a scattering situation and to exhibit a formal expression for the scattering amplitude as an integral of the scattered fields over S . Since the scattering objects are supposed to be outside the volume V , equation (4) holds for the scattered fields $(\mathbf{E}_s, \mathbf{B}_s)$, that is, the total fields (\mathbf{E}, \mathbf{B}) minus the incident fields $(\mathbf{E}_i, \mathbf{B}_i)$ (i.e., the fields generated by active sources such as antennas). In equation (4) $\mathbf{E}(\mathbf{x})$ depends explicitly on the outgoing direction of \mathbf{k} . The dependence on the incident direction is implicit in the scattered fields \mathbf{E} and \mathbf{B} .

3 Description of the model

The evaluation of the field \mathbf{E} through equation (4), requires the knowledge of the fields \mathbf{E}_s and \mathbf{B}_s on the surface S .

3.1 A single scatterer

In the absence of knowledge about the correct fields \mathbf{E}_s and \mathbf{B}_s on the surface S , we must make some approximations.

First, we neglect the field transmitted through the building. This is equivalent to assuming that the building is an "opaque" object. This assumption is reasonable at the frequencies we are dealing with as the part of the wave energy which is not reflected from the surface, is largely dissipated inside the building. Because the wavelength is small with respect to the linear dimensions of the obstacle, the surface S of the building can be divided

approximately into an illuminated region S_i and a shadowed one S_s . In the shadowed region the total field on the surface S_s is nearly zero (the object is opaque). We assume that there the scattered field on S_s is equal and opposite to the incident field. In addition, we suppose that the building's external walls are either flat or with a radius of curvature large with respect to the wavelength. As a result, in the illuminated region, Fresnel coefficients for reflection are used to evaluate the scattered field on S_i . This procedure can be summarized as follows:

- s1) the incident fields \mathbf{E}_i and \mathbf{B}_i (generated by the antenna) are evaluated on the surface S of the scatterer;
- s2) the scattered fields \mathbf{E}_s and \mathbf{B}_s on S are approximated as described above;
- s3) the scattered fields throughout the space V are computed using the Kirchhoff integral method.

This method gives a good estimate of the scattered field around an opaque object. If the diffraction effects on the building wedges are negligible, we can simplify the above procedure by assuming a "Geometrical Optics" shadow for the incident field, i.e. by assuming that both the incident and scattered fields are equal to zero beside the obstacle. When we are dealing with a large number of scatterers, this approximation can allow a sensible reduction in the computational time, because it reduces the number of pair-interactions (only the pairs of scatterers that "see" each other interact). This aspect will be discussed in detail in section 4.1. Later on this paper, we will refer to the first procedure as the "general procedure" and to the second as the "GOS (Geometrical Optics Shadow) procedure".

3.2 More than one scatterer

When dealing with more than one building, the procedure for one scatterer can be extended using an iterative technique where each iteration corresponds to a reflection on a surface.

- a: The incident field produced by all the sources is evaluated on each building surface S_n :
 - at the first iteration, the only source is the antenna;
 - starting from the second iteration, the sources of incident field are the antenna and all the surfaces which have been illuminated during the previous iteration. The second contribution is evaluated by using the Kirchhoff integral.

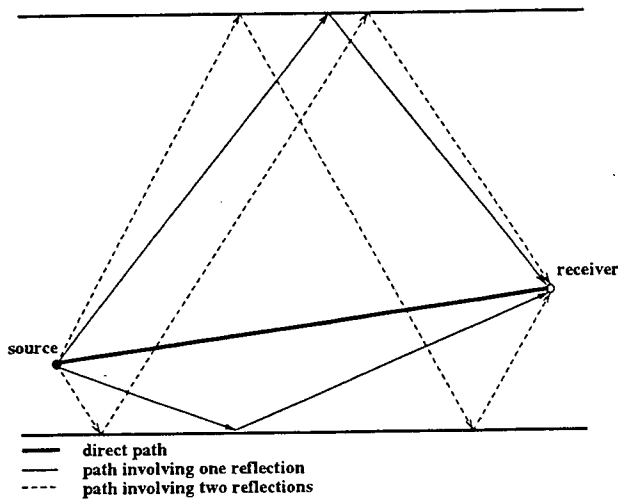


Figure 1: Example of source-receiver paths involving up to two reflections. These paths are accounted for by the method after two iterations

b: When the incident fields \mathbf{E}_i and \mathbf{B}_i are known at each point of the surface S_n , the scattered fields \mathbf{E}_s and \mathbf{B}_s on S_n are evaluated as described in section 3.1. At the frequencies considered, the diffraction fields are small with respect to the Geometrical Optics fields and they can be neglected if the intensity of incident radiation is low. Therefore, we have chosen to evaluate the scattered fields on S_n by using the "general procedure" when the source of the incident fields \mathbf{E}_i and \mathbf{B}_i is the antenna and the "GOS procedure" elsewhere. \mathbf{E}_s and \mathbf{B}_s will be used in the first step of the next iteration to compute the incident field on the other surfaces.

c: When the electromagnetic fields do not significantly change from one iteration to the next one, the procedure ends.

d: At the end of the iterative procedure, we know the electromagnetic fields on all the involved surfaces and we can use, once again, the Kirchhoff integral to evaluate the electromagnetic field throughout the domain V .

The above procedure is sketched in figure 1 in the case of two buildings and up to the second iteration. It is seen that, each iteration is equivalent to include new paths connecting the source to the receiver.

To analyze the convergence of the method, we consider the configuration described in figure 2. A plane wave of wavelength $\lambda = 6.28$ meters and wave vector $\mathbf{k} = (0.89, 0.42, -0.15)$, whose projection onto $z = 0$ is drawn in the picture, has been taken as the incident field. At each iteration, the field values are measured at points

located at a height of 1.8 meters, along the axis shown in the figure.

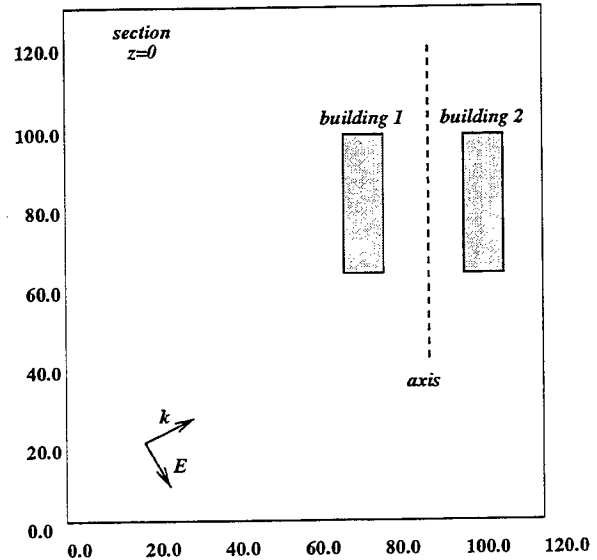


Figure 2: Geometry used to test convergence of the method. Receivers are located along the dashed line between the two buildings (all dimensions are given in meters)

At iteration n , the convergence of the method is checked through the following parameters:

$$\begin{aligned} \text{er}_{E_i}^n &= \max \{ |E_i^n(k) - E_i^{n-1}(k)|, k = 1, N_r \}, \\ &\quad i = 1, 3 \\ \text{er}_E^n &= \max \{ \text{er}_{E_i}^n, i = 1, 3 \} \end{aligned}$$

where N_r is the number of receivers.

Figure 3 reports the values of er_E^n at each iteration. The lines refer to two different simulations where the buildings are considered either metallic or built with material of dielectric constant $\epsilon = 4$. In the second case, the convergence is faster because, at each iteration, part of the incident energy is absorbed by the external walls.

In figure 4 we report the values of two components of the electromagnetic field, computed in the case of metallic buildings. The convergence of the component E_y is much slower than that of the component E_x . This can be intuitively explained by noting that an y -directed electric field can be associated to an x -directed wave, which is reflected between the metallic walls as in a resonating cavity, while the x -directed electric field, related to an y -directed wave, is free to leave the system. So we expect that the y component will keep changing at each iteration (and further reflection) between the buildings (i.e. $65 < y < 100$) more than outside them, and this is confirmed by the results of the simulation shown in figure 4 (bottom).

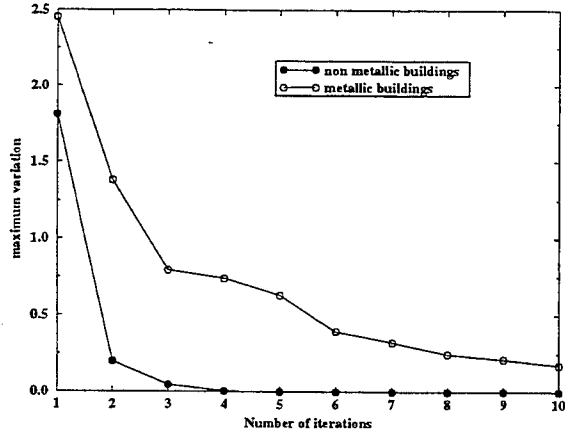


Figure 3: Convergence of the method. White dots refer to perfectly conducting surfaces. Black dots refer to dielectric surfaces ($\epsilon = 4$). The quantity "maximum variation", reported on y axis, is defined as $er_E^n = \max \{er_{E_i}^n, i = 1, 3\}$, where $er_{E_i}^n$ is $er_{E_i}^n = \max \{|E_i^n(k) - E_i^{n-1}(k)|, k = 1, N_r\}$, $i = 1, 3$ and N_r is the number of receivers

4 Computational aspects

In this section we present the main computational features of the model.

4.1 Scaling of the computer time with the dimension of the domain

The model described in section 3 requires, on each surface, the evaluation of the field scattered from the other surfaces. Thus, at first sight, the computational time grows as N^2 with N the number of surface elements and as D^4 with D the diameter of the domain. This behavior is even worse than the one shown by the methods which require the discretization of the whole space (D^3), but, as we will show, can be easily improved.

Consider the situation described in figure 5. S_2 is a region of the surface on which we need to compute the field scattered by a region S_1 of another surface; we can write

$$\mathbf{r} = \mathbf{r}_0 - \mathbf{x}' + \mathbf{x}''$$

and

$$r = [r_0^2 - 2\mathbf{r}_0 \cdot (\mathbf{x}' - \mathbf{x}'') + |\mathbf{x}' - \mathbf{x}''|^2]^{\frac{1}{2}}$$

When r is large compared with x' and x'' , we can rewrite r using a suitable Taylor expansion:

$$r = r_0 - \frac{\mathbf{r}_0 \cdot (\mathbf{x}' - \mathbf{x}'')}{r_0} + T \quad (5)$$

where

$$T = \frac{|\mathbf{x}' - \mathbf{x}''|^2}{2r_0} - \frac{[\mathbf{r}_0 \cdot (\mathbf{x}' - \mathbf{x}'')]^2}{2r_0^3} + \dots \quad (6)$$

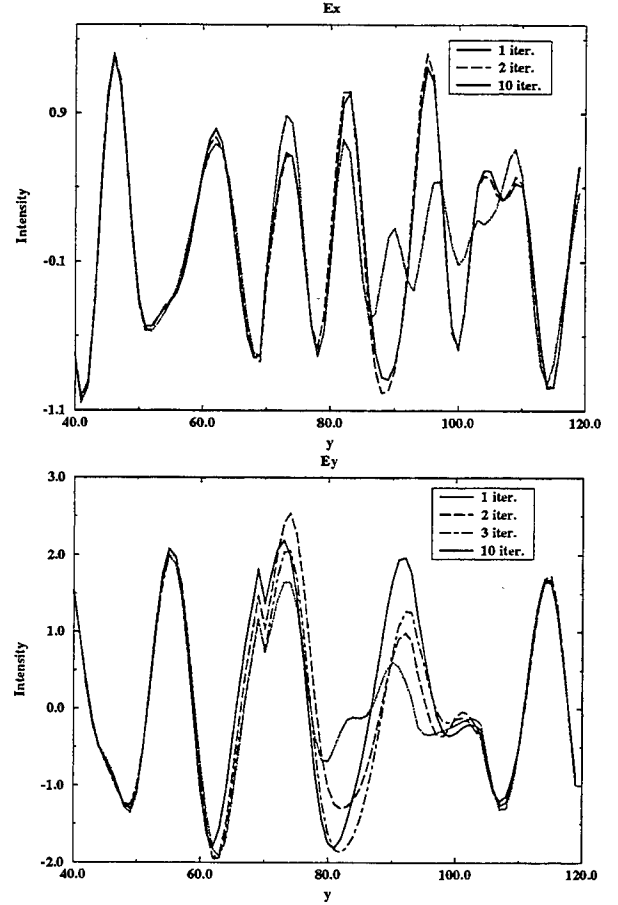


Figure 4: Components E_x (top) and E_y (bottom) at different iterations in the example shown in figure 2. The spatial coordinate along the dashed line is reported on the x axis

Provided that T is negligible, we have:

$$e^{ikr} = e^{ikr_0} e^{-ik \cdot (\mathbf{x}' - \mathbf{x}'')} \quad (7)$$

Let d' and d'' be the diameters of the regions S_1 and S_2 . To get a quantitative estimate, we impose that the error on the phase is bounded by $\frac{\pi}{8}$. Then, looking at equation (6), we can see that T is negligible when

$$\frac{(d' + d'')^2}{8r_0} < \frac{\lambda}{16} \implies (d' + d'') < \sqrt{\frac{\lambda r_0}{2}} \quad (8)$$

which is equivalent to the well-known far field relation. In this approximation, equation (4) becomes:

$$\mathbf{E}_s(\mathbf{x}) = \frac{i}{4\pi} \frac{e^{ikr_0}}{r_0} e^{ik \cdot \mathbf{x}''} \mathbf{F}(\mathbf{k}) \quad (9)$$

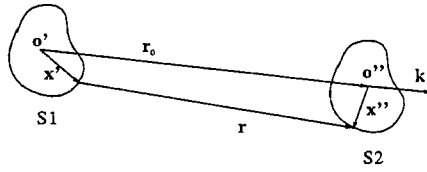


Figure 5: Scattering geometry

$$F(k) = \oint_{S_1} e^{-ik \cdot x'} \{k(n' \times B_s) + [k \times (n' \times E_s) - k(n' \cdot E_s)] \left(1 + \frac{i}{kr}\right)\} dx' \quad (10)$$

In equation (10), the integral does not depend on the coordinate x'' internal to the region S_2 . Therefore, when we decompose the surfaces into regions which are small compared to their relative distance, we need to evaluate the integral only once for each region.

Since the area of the surface regions is proportional to r_0 (see equation (8)), with this approximation the computational time for the evaluation of the interaction between two surfaces is inversely proportional to their relative distance r_0 . Moreover, the probability that one building A_1 "can see another building" A_2 (i.e. there aren't buildings between A_1 and A_2) decreases exponentially with r_0 . Then, it can be demonstrated that the computational time grows as $N^{\frac{3}{2}}$ with the number N of transparent buildings and linearly with the number of opaque ones.

In order to check these results, we have performed some computations on configurations of n^2 buildings with $n = 2, \dots, 6$ illuminated by the field emitted from an antenna. The buildings have been uniformly distributed over a square region (n per direction) and the antenna has been located at the center of the layout. The results are shown in figure 6 where $N = n^2$ represents the number of buildings and the relative computational time is defined as the ratio T_N/T_4 between the computational time required for N buildings and that required for 4 buildings. We can see that the scaling of time is similar to $N^{\frac{3}{2}}$ for a small number of buildings and to N further.

4.2 Reflections on the ground

In the simulation of the radioelectric propagation in urban areas, a numerical treatment of the ground using the Kirchhoff integral is, from a computational point of view, expensive.

We assume therefore that the reflection from the ground can be computed by Geometrical Optics. This

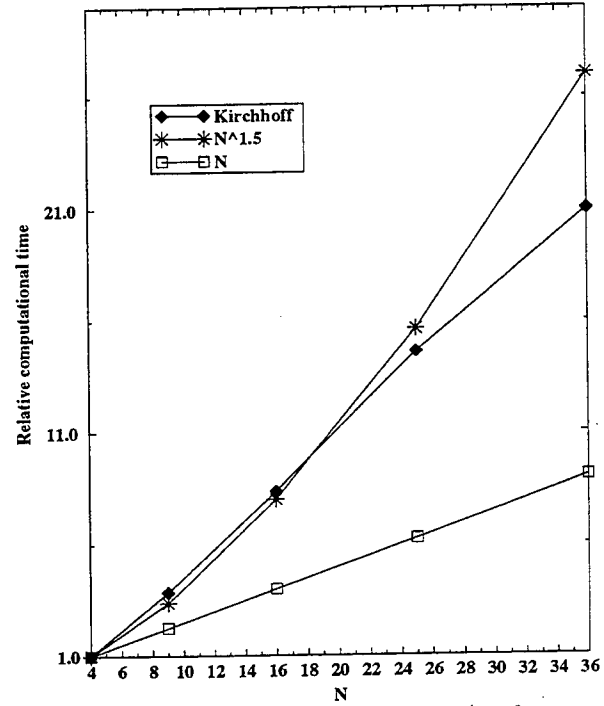


Figure 6: Scaling of the relative time T_N/T_4 for a regular distribution of $\sqrt{N} \times \sqrt{N}$ buildings. Black diamonds correspond to times measured for the Kirchhoff integral method

assumption cannot be done for reflection from the buildings' walls. We refer to figure 7 for a brief explanation. The effects of diffraction, which are neglected by GO, are noticeable only near the light-shadow boundaries of the incident and reflected field. These boundaries exist only when we deal with reflections from the wall. For ground reflections, the incident and reflected fields have no discontinuities.

For the ground-wall double reflection, the discontinuity is inside the domain (see figure 8), but is partially compensated by the discontinuity due to the wall-ground double reflection. Since the wall and the ground form a 90 degree angle, the two discontinuities coincide, and it can be seen that the values of the two contributions are similar.

We notice that in the case of perfectly conducting walls and ground, the effects of diffraction are nonexistent. In fact the two surfaces give only three distinct contributions, two corresponding to single reflections on the walls, one corresponding to a double reflection. Each contribution can be attributed to a different image source and is accounted for by GO.

In figure 9, points A and B represent a source and a receiver respectively. The source can be either the antenna or any point of a scattering surface while the receiver can be either any point of a different scattering

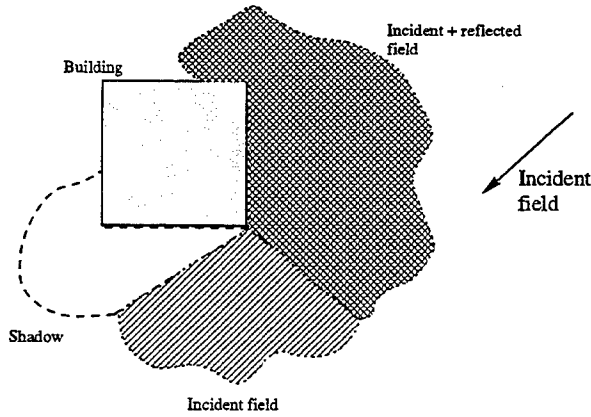


Figure 7: Light-shadow boundaries of the incident and reflected field

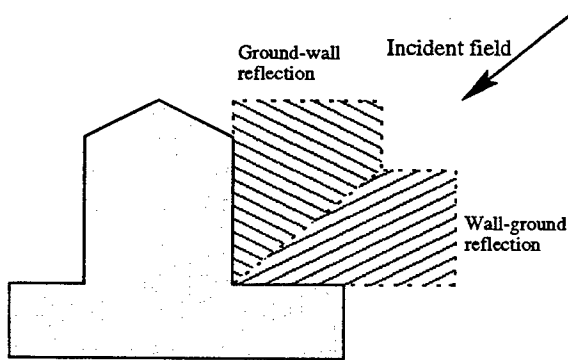


Figure 8: Geometrical description of the ground-wall double reflection paths

surface or any point where we want to compute the field value.

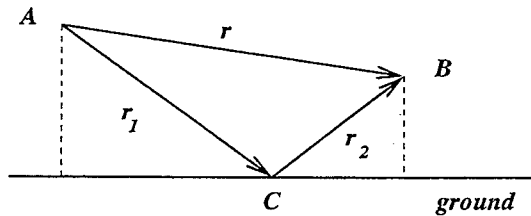


Figure 9: Geometrical scheme to illustrate ground reflections treatment

For each direct path r from A to B, there is another path r_1 and r_2 which involves one reflection on the ground at the point C. The contribution of the reflection in C to the field value in B is computed considering the lengths r_1 , r_2 and by using Fresnel coefficients.

These considerations have been validated by implementing both the explicit (evaluation of the Kirchhoff integral) and implicit (Geometrical Optics) treatments

of reflections on the ground and comparing the results on a test configuration. The layout (position of buildings and observation axis) is schematically described in figure 2. The input data of the simulation are equal to those given in section 3, with $\epsilon = 4$. The implicit treatment of ground reflections brings to numerical results which are similar to those obtained with an explicit one (see figure 10) and it allows, at the same time, a sensible reduction in both the computational time and storage memory. Moreover, it avoids the generation at the ground boundary, of fictitious diffraction terms which decrease the computed field when ground reflections are explicitly considered.

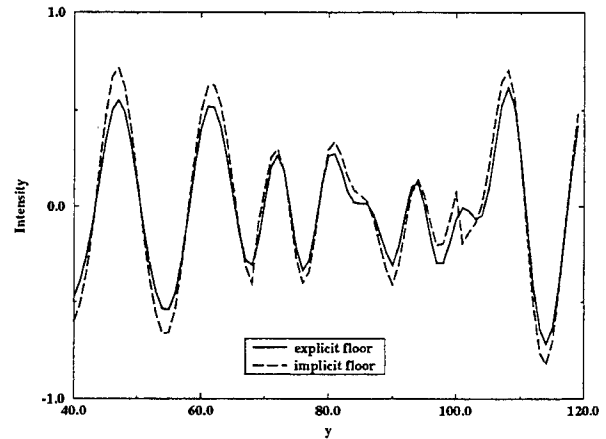


Figure 10: Component E_x of the electromagnetic field. The continuous line represents the field obtained by explicitly computing ground reflections with the Kirchhoff integral; the dashed line represents the field obtained by implicit (purely GO) ground treatment

5 Results

In sections 3 and 4, we have presented some results related to the convergence and time complexity of the method described here. The validation of the approach described in this paper is done by comparing the simulation outcome with a number of experimental measurements. In this section, we are going to present the results of these comparisons.

5.1 Radioelectric coverage in an urban environment

We give here the results of a numerical simulation of the propagation of the field emitted by an antenna throughout an urban environment. In figure 11, the white blocks represent the buildings of a real city and their parameters

(dielectric constant ϵ , height h_b , etc.) have been chosen uniformly over the layout because of the lack of detailed measurements. In particular, we have chosen $\epsilon = 4$ and $h_b = 10$ meters. The frequency of the field emitted by the source (antenna with a nonisotropic radiation pattern) is 1.8 GHz which corresponds to a wavelength of 16.7 centimeters. Input power is 250 mW. The source is located at a height of 4.5 meters and the electric field is computed at a height of 1.6 meters.

The cross in the center of the figure marks the position of the source and the gray scale indicates the simulated field power, decreasing from white to black. For an area of about 300 meters diameter, the whole simulation has taken 24 hours on a RISC/6000 560 IBM.

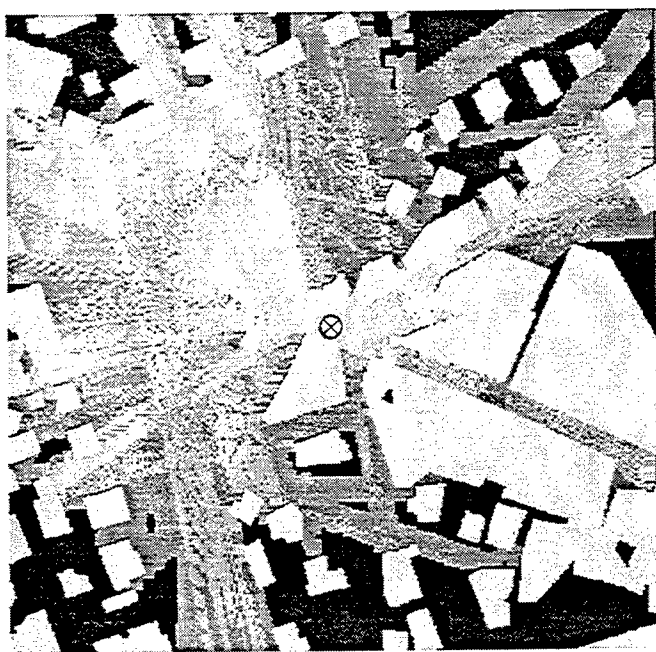


Figure 11: Example of the power emitted by an anisotropic antenna, obtained by the Kirchhoff integral method.

5.2 Comparison with experimental measurements

Comparisons with experimental measurements in realistic conditions are quite difficult because of the absence of accurate data on the computational domain. The dielectric constant of the involved materials and the height of the buildings are not known. Moreover, the map of the town is available with a precision of one meter; therefore, the direction error for shorter walls can be of the order of about ten degrees which doubles when we consider the direction of the reflected field. Further, due to interference phenomena, the field can vary considerably within one meter. Finally, no information is available about

the presence of objects other than buildings; a parked car can easily intercept the ground-reflected field.

In these conditions, the computed power may easily differ by 10 to 20 dbm from the measured one and point-to-point comparisons cannot be used to validate or invalidate the code. On the other hand, the errors are fairly localized and the code can be still used with some confidence to estimate the coverage areas.

In the following figures, the cross marks the position of the antenna, while the numbered dots indicate the positions of the points where measurements have been taken. The light gray defines the area where the computed power is above threshold for both Geometrical Optics and Kirchhoff's method. The dark gray indicates the area where the power values are above threshold only for Kirchhoff's method. The area where the computed power values are below threshold is represented in black. The input data for both simulations (buildings' parameters, source's frequency, area's diameter) are equal to those used in section 5.1. Experimental data were obtained by a DECT system using propagation tester Symbionics SP935.

In figure 12, the computed coverage area of the antenna is represented for a threshold power of -85 dbm. It can be seen that the coverage area evaluated with Geometrical Optics is about 20% less than obtained with Kirchhoff's method. Moreover, two of the points considered ($\{5, 7\}$) lie outside it, while all the measured values and those evaluated with Kirchhoff's method are above threshold. Figure 13 has been obtained by raising the threshold up to -70 dbm. The measured values fall under the threshold in four points $\{1, 2, 3, 4\}$ and three of them are outside or very close to the boundaries of Kirchhoff's coverage area. The only evident discrepancy concerns point $\{4\}$ whose measured value is under the threshold while both Geometrical Optics and Kirchhoff's calculations locate it inside the illuminated region. Therefore, on the one hand, Kirchhoff's estimate of the coverage area clearly improves the Geometrical Optics one; on the other hand, due to the inaccuracy of the input data, the reliability of the results is limited and it is advisable to use a fairly large margin of safety.

6 Conclusions

The starting point for the planning and maintenance of any mobile communication network is based on a prediction of the radio wave attenuation around the source (antenna) in the layout of the buildings. In this paper we have proposed an iterative procedure based on the Kirchhoff integral method. Results have shown that this method is well suited to solve this problem and offers promising prospects of development in this field. The

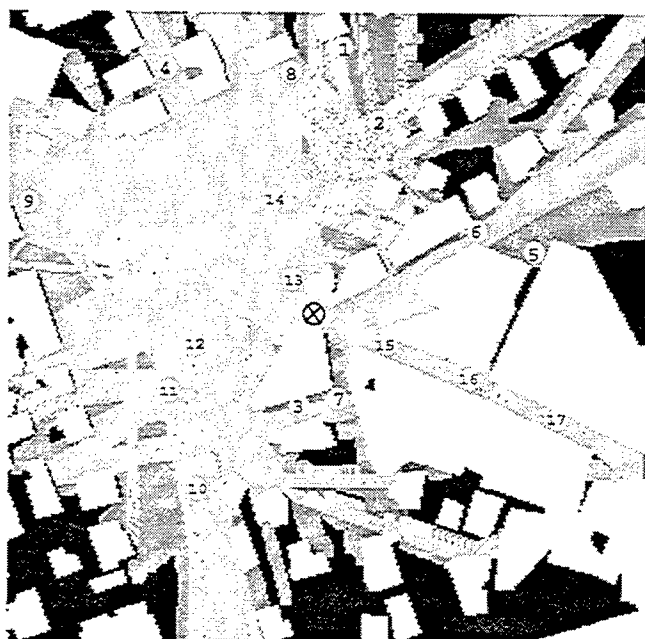


Figure 12: The coverage region of the antenna for a threshold power of -85 dbm. The light gray area defines the zone where both Geometrical Optics and Kirchhoff's method predict a value for the field power above threshold. The dark gray area corresponds to the zone where only the value predicted by Kirchhoff's method is above threshold. The black area defines the zone where both Geometrical Optics and Kirchhoff's method predict values below threshold. The antenna location is indicated by the cross, while the numbered dots indicate the location of receivers for experimental measurements

model is currently under revision to improve its time requirements (Pisani, 1997).

7 Acknowledgements

We would like to thank Prof. G. Mazzarella of the University of Cagliari for helpful discussions and comments on the manuscript. We acknowledge A. Loche for providing us with a graphic interface for the visualization of the radioelectric coverage and Ing. F. Tallone of the Centro Studi e Laboratori Telecomunicazioni (CSELT) of Turin for providing us with experimental measurements. This work has been carried out with the financial support of Telecom Italia and the Sardinia Region Authorities.

References

- F. Ikegami, T. Takeuchi, and S. Yoshida, "Theoretical prediction of mean field strength for urban mobile radio", *IEEE Trans. Antenn. Propagat.*,



Figure 13: The coverage region of the antenna for a threshold power of -70 dbm. The meaning of the symbols and grey scale is the same as figure 12

vol. 39, pp. 299-302, 1991.

- J. D. Jackson, *Classical Electrodynamics*, John Wiley & Sons, New York (1975).
- T. Kürner, D.J. Cichon, and W. Wiesbeck, "Concepts and results for 3D digital terrain-based wave propagation models: an overview", *IEEE J. Select. Areas Commun.*, vol. 11, no. 7, pp. 1002-12, 1993.
- P. O. Luthi, B. Chopard, J-F Wagen, "Wave Propagation in Urban Microcells: a Massively Parallel Approach Using the TML Method", *Lecture Notes in Computer Science*, vol. 1041, pp. 408, 1996.
- L. Pisani, "Dimensionality reduction in the numerical evaluation of electro-magnetic scattering: from the Kirchhoff's integral method to a zero dimensional approach", submitted to *Computer Phys. Commun.*
- K. Rizk, J-F Wagen, F. Gardiol, "Ray tracing based path loss prediction in two microcellular environments", in *Proceedings IEEE PIMRC'94*, pp. 210-4, The Hague, Netherlands, 1994.
- J.P. Rossi, A.J. Levy, "A ray model for decimetric radiowave propagation in an urban area", *Radio Science*, vol. 27, no. 6, pp. 971-9, 1992.

On the Bounded Part of the Kernel in the Cylindrical Antenna Integral Equation

M.P. Ramachandran

Analysis and Facility Division

Space Applications Center

Ahmedabad 380 053, India

Abstract

The kernel in the cylindrical antenna integral equation was partitioned by Schelkunoff into a complete elliptic integral and a bounded integral. This paper gives an exact expression for the bounded part.

1 Introduction

The cylindrical antenna integral equation for total axial current $I(z)$ on perfectly conducting tube of length ' $2h$ ' and radius ' a ' is [1]:

$$j\omega \left(\frac{d^2}{dz^2} + k^2 \right) A_z(z) = k^2 E_z^i(z), \quad (1)$$

where

$$A_z(z) = \frac{\mu}{4\pi} \int_{-h}^h K(z - z') I(z') dz'. \quad (2)$$

The kernel in (2) is:

$$K(z - z') = \frac{1}{2\pi} \int_{-\pi}^{\pi} \frac{e^{-jkR}}{R} d\phi', \quad (3)$$

where

$$R = R(z - z', \phi') = \left[(z - z')^2 + 4a^2 \sin^2 \left(\frac{\phi'}{2} \right) \right]^{1/2}. \quad (4)$$

Here ϵ and μ characterize the medium [1], and k is the wavenumber.

For thin structures ($a \ll h$ and $a \ll \lambda$), $K(z - z')$ is usually substituted by a reduced kernel approximation

$$K \simeq K_r(z - z') = \frac{e^{-jkr}}{r}, \quad (5)$$

where

$$r = r(z - z') = [(z - z')^2 + a^2]^{1/2}. \quad (6)$$

The kernel (3) possesses a logarithmic singularity (see for example [2]). This needs to be included while solving (1). Schelkunoff has partitioned the kernel into two parts.

The first part is a complete elliptic integral and the second part is a bounded integral. By expanding the elliptic integral, Pearson [3] has derived an expression which includes the logarithmic singularity. On the other hand, as the exact expression of the bounded integral is not available,

it is usually evaluated numerically. Karwowski [4] has suggested a closed form approximation; an alternative to the numerical integration. In this presentation we obtain an exact expression for the bounded part. Certain recurrent relations are obtained to simplify its computation. The stability of the recurrence relations is analyzed and checked.

Before we conclude this section we shall briefly review other research accomplishments regarding the kernel (3). Wang [5] has obtained an 'exact' expression for the kernel (3) in terms of spherical Hankel functions. Werner [6] has presented an alternative 'exact' expression replacing the spherical Hankel functions by complex exponential functions. This has an advantage from the point of view of analytical and numerical evaluation of the kernel. Werner has presented 'extended' approximations [7] to the kernel, by truncating the series to a few terms. This is an alternative to the reduced approximation (5). Interestingly, the vector potential in (2) due to the singular part K_E has been worked by Werner, et al [8]. The results of this paper on the bounded part K_B can be useful when combined with the results of Pearson [3] or Werner, et al [8].

2 Kernel

Recall the Schelkunoff partition:

$$K(z - z') = K_E + K_B, \quad (7)$$

where

$$K_E = \frac{1}{2\pi} \int_{-\pi}^{\pi} \frac{1}{R} d\phi' \quad (8)$$

and

$$K_B = -\frac{1}{2\pi} \int_{-\pi}^{\pi} \frac{1 - e^{-jkR}}{R} d\phi'. \quad (9)$$

Expanding the first integral, an elliptic integral, Pearson has obtained the following expression, which we reproduce, with a correction:

$$K_E = -\frac{1}{\pi a} \ln |z - z'| + K_{EB}, \quad (10)$$

where

$$\begin{aligned} K_{EB} = & \frac{1 - \beta}{\pi a} \ln |z - z'| + \frac{\beta}{\pi a} \cdot \\ & \left\{ \ln 8a - \ln \beta + \left(\frac{1}{2}\right)^2 \left[\ln \left(\frac{4}{\beta_1}\right) - \left(\frac{2}{1 \cdot 2}\right) \right] \beta_1^2 \right. \\ & \left. + \left(\frac{1 \cdot 3}{2 \cdot 4}\right)^2 \left[\ln \left(\frac{4}{\beta_1}\right) - \left(\frac{2}{1 \cdot 2}\right) - \left(\frac{2}{3 \cdot 4}\right) \right] \beta_1^4 \dots \right\}. \end{aligned} \quad (11)$$

We have used the following notation

$$\beta = \frac{2a}{[4a^2 + (z - z')^2]^{1/2}}, \quad \beta_1 = (1 - \beta^2)^{1/2}. \quad (12)$$

The series is convergent for $|z - z'| \leq 4a$. The leading term in K_{EB} can be shown to be of the form $(z - z')^2 \ln |z - z'|$. Next, we shall obtain an exact expression for K_B .

3 Expression for K_B

K_B can be written as

$$K_B = K_{Br} + K_{Bi} \quad (13)$$

where K_{Br} is the real part and K_{Bi} is the imaginary part

$$K_{Br} = \frac{-1}{2\pi} \int_{-\pi}^{\pi} \frac{(1 - \cos kR)}{R} d\phi' \quad (14)$$

and

$$K_{Bi} = \frac{-j}{2\pi} \int_{-\pi}^{\pi} \frac{\sin kR}{R} d\phi' \quad (15)$$

Expanding $\sin kR$ in eq. (15) and setting $(z - z') = u$, we get the infinite series:

$$K_{Bi} = -\frac{j}{\pi} \sum_{m=0}^{\infty} \frac{(-1)^m k^{2m+1} A_{m-1}(u, a)}{(2m+1)!} \quad (16)$$

where

$$A_{m-1}(u, a) = \int_0^{\pi} R_1^{2m} d\mu \quad (17)$$

and

$$R_1 = [u^2 + 4a^2 \sin^2 \mu]^{1/2} \quad (18)$$

We find from eqs. (17) and (18) that

$$A_{-1}(u, a) = \pi \quad (19)$$

and

$$A_0(u, a) = \pi (u^2 + 2a^2) \quad (20)$$

In eq. (17), we rewrite $A_{m-1}(u, a)$ as:

$$\begin{aligned} A_{m-1}(u, a) &= \int_0^{\pi} (u^2 + 4a^2 \sin^2 \mu)^{m-1} (u^2 + 4a^2 \sin^2 \mu) d\mu \\ &= (u^2 + 2a^2) A_{m-2}(u, a) - 2a^2 \int_0^{\pi} (u^2 + 4a^2 \sin^2 \mu)^{m-1} \cos 2\mu d\mu. \end{aligned}$$

Apply integration by parts to the integral. After certain algebraic manipulations, we get the recurrence relations:

$$\begin{aligned} [1 + (m-1)] A_{m-1} &= (u^2 + 2a^2) [1 + 2(m-1)] A_{m-2} \\ &\quad - (m-1)u^2 (u^2 + 4a^2) A_{m-3}; \quad m = 2, 3, 4, \dots \end{aligned} \quad (21)$$

Using A_{-1} , A_0 from eqs. (19) and (20) we find A_{m-1} ; $m = 2, 3, 4, \dots$ and then determine K_{Bi} from eq. (16) up to a desired accuracy. The stability of the recurrence relations needs to be examined for a given radius 'a' and length '2h' of the wire. This has been done in the stability section. Now, on similar lines the real part, namely K_{Br} , becomes

$$K_{Br} = -\frac{1}{\pi} \sum_{m=0}^{\infty} \frac{(-1)^m k^{2m+2} B_{m-1}(u, a)}{(2m+2)!} \quad (22)$$

where

$$B_{m-1}(u, a) = \int_0^\pi R_1^{2m+1} d\mu. \quad (23)$$

We discuss the computation of K_{Br} for two distinct cases of $u = z - z'$, namely for $u = 0$ and for $u \neq 0$.

From eq. (23) we find

$$B_{-1}(0, a) = 4a \quad (24)$$

and then obtain recurrence relation

$$B_{m-1}(0, a) = \left[\frac{2m}{(2m+1)} \right] (2a)^2 B_{m-2}(0, a). \quad (25)$$

Computed values of B_{m-1} , $m = 1, 2, 3, \dots$ are substituted in eq. (22). It may be noted that the recurrence relation is stable for $a < 0.5$. This is a dimensionless number.

We obtain the following results using [9]

$$\begin{aligned} B_{-1}(u, a) &= 2u \int_0^{\pi/2} (1 + q^2 \sin^2 \mu)^{1/2} d\mu \\ &= 2usE\left(\frac{q}{s}\right), \end{aligned} \quad (26)$$

where we have used the notation $q = (2a/u)$, $s = (1 + q^2)^{1/2}$. Further,

$$B_0(u, a) = 2u^3 \left[sE\left(\frac{q}{s}\right) + q^2 I(q) \right], \quad (27)$$

where

$$I(q) = \frac{1}{3} \left\{ \left[\frac{(2q^2 + 1)}{q^2} \right] sE\left(\frac{q}{s}\right) - \left(\frac{s}{q^2}\right) F\left(\frac{q}{s}\right) \right\}. \quad (28)$$

E and F are elliptic integrals of second and first kind, respectively, and are evaluated to a desired accuracy using Landen's Transformation [10]. The recurrence relation now is:

$$\begin{aligned} B_{m-1}(u, a) \left[1 + \left(\frac{2m-1}{2} \right) \right] &= (u^2 + 2a^2) B_{m-2}(u, a) [1 + (2m-1)] \\ &\quad - \left[\left(\frac{2m-1}{2} \right) u^2 (u^2 + 4a^2) B_{m-3}(u, a) \right] \\ m &= 2, 3, 4, \dots \end{aligned} \quad (29)$$

Using eqs. (26) and (27) we can obtain B_{m-1} , $m = 2, 3, 4, \dots$ and then evaluate K_{Br} . The stability of eq. (29) is also included in the next section.

4 Stability

The characteristic equation [11] corresponding to eq. (21) is:

$$(1+n)x^2 - \alpha(1+2n)x + n\gamma = 0; \quad n = 1, 2, \dots \quad (30)$$

where $\alpha = (u^2 + 2a^2)$, $\gamma = u^2(u^2 + 4a^2)$. Rewrite eq. (30) as

$$\frac{x(x - \alpha)}{\alpha x - \gamma} = \frac{n}{(1 + n)}. \quad (31)$$

The above equation is useful to seek the stability condition, namely $|x| < 1$. For a given radius 'a' and length of wire '2h', this condition shall depend upon λ .

Denoting

$$\frac{n}{(1 + n)} = p \quad (32)$$

The solution of (31) is

$$x = \frac{\alpha(1 + p) \pm [\alpha^2(1 - p)^2 + 16pa^4]^{1/2}}{2}. \quad (33)$$

The right hand side is a monotonic increasing function for given values of p and a , enabling direct evaluation of the maximum of x . For recurrence relations corresponding to the real part given in eq. (29), the analysis is repeated on similar lines with

$$p = \frac{(2n + 1)}{(2n + 2)}; \quad n = 1, 2, 3, \dots, \quad (34)$$

yet the stability criteria is not altered. Thus, for any wire of known radius 'a' and length '2h', using eq. (33) we can easily establish the condition of stability on λ before computing the recurrence relations and determining K_B .

5 Examples

As a first case we have a dipole of half-wave length in length and whose radius is $(\lambda/8)$. From eq. (21), we note that the value of p varies from $1/2$ to a limit of 1. Then, the maximum of x in eq. (33) is $5\lambda^2/16$, which implies that the condition for stability is $\lambda < 4/\sqrt{5}$, that is approximately 1.7888. This is not a strong condition as only a limiting value could be used. In the first example we set the radius of the wire to be 0.003 and λ to be 1.0. This is a case of thin wire and Karwowski's results are accurate. We have given in Table 1 for various values of $u = z - z'$, the (real, imaginary) values of K_B from (16) and (22). These values are compared with those of Karwowski [4].

Next, we consider a cylindrical wire of a wavelength in length and radius $(\lambda/4)$. The maximum value of x is $(5\lambda^2/4)$. Thus, for $\lambda < 2/\sqrt{5}$ (approximately 0.8944), the recurrence relations in eqs. (21) and (29) are stable. The condition in eq. (25) that $a < 1/2$ is satisfied in this case also. In the second example we have $a = 0.22$ and $\lambda = 0.88$. The corresponding results are given in Table 2. Here, while setting $\lambda = 0.90$, the recurrence relation was verified to be unstable, which agrees with our estimate. The values in the tables are correct up to four decimal places and appropriately rounded up to three decimal places. Only 12 terms in the series were used to obtain this accuracy. The difference between the sets of the values is due to the approximation introduced by Karwowski in replacing $(1/R)$ by $(\sin \phi/R)$ in (9) and thus apparently diminishing the contribution near the ends of the interval.

Table 1: Comparison between this work and that of Karwowski [4] for a thin wire half-wave dipole.

$a = 0.003$ and $\lambda = 1.0$		
u	Present	Karwowski
0.0	(-0.075, -6.282)	(-0.075, -6.282)
0.1	(-1.885, -5.877)	(-1.911, -5.877)
0.2	(-3.433, -4.755)	(-3.455, -4.755)
0.3	(-4.347, -3.170)	(-4.364, -3.170)
0.4	(-4.513, -1.469)	(-4.552, -1.469)
0.5	(-3.997, +0.226)	(-4.000, +0.226)

Table 2: Comparison between this work and that of Karwowski [4] for a thick wavelength long wire.

$a = 0.22$ and $\lambda = 0.88$		
u	Present	Karwowski
0.000	(-4.114, -3.063)	(-4.341, -2.894)
0.176	(-4.500, -2.001)	(-4.584, -1.852)
0.352	(-4.150, +0.150)	(-4.152, +0.250)
0.528	(-2.577, +1.406)	(-2.215, +1.451)
0.704	(-0.884, +0.903)	(-0.431, +0.909)
0.880	(-0.323, -0.371)	(-0.096, -0.380)

6 Conclusion

This paper makes an effort to evaluate the kernel by the definition of Schelkunoff [1]. An exact expression for the bounded part of the kernel K_B is given. This result can be used along with that of Pearson [3] for solving cylindrical antenna integral equations. Examples are considered where K_B is evaluated by the present method and is compared with that of Karwowski [4].

Acknowledgement

The author thanks the reviewers for their suggestions in improving the quality of presentation of this paper.

References

- [1] S.A. Schelkunoff, *Advanced Antenna Theory*, John Wiley, New York, 1952.

- [2] D.S. Jones, "Note on the integral equation for straight wire antenna," *IEE Proc., Microwaves, Antennas, and Propagation*, Vol. 128, pp. 114–116, 1981.
- [3] L.W. Pearson, "A separation of logarithmic singularity in the exact kernel of the cylindrical antenna integral equation," *IEEE Trans. Antennas and Propagation*, Vol. AP23, pp. 256–258, 1975.
- [4] A. Karwowski, "Closed form approximation to the bounded part of the exact kernel of a cylindrical antenna integral equation," *IEE Proc., Microwaves, Antennas, and Propagation*, Vol. 135, pp. 210–212, 1988.
- [5] W. Wang, "The exact kernel for cylindrical antenna," *IEEE Trans. Antennas and Propagation*, Vol. AP30, pp. 434–435, 1991.
- [6] D.H. Werner, "An exact formulation for the vector potential of a cylindrical antenna with uniformly distributed current and arbitrary radius," *IEEE Trans. Antennas and Propagation*, Vol. AP41, pp. 1009–1018, 1993.
- [7] P.L. Werner and D.H. Werner, "Approximations for the cylindrical wire kernel," *Elec. Letters*, Vol. 32, pp. 2108–2109, 1996.
- [8] D.H. Werner, J.A. Huffman, and P.L. Werner, "Techniques for evaluating the uniform current vector potential at the isolated singularity of the cylindrical wire kernel," *IEEE Trans. Antennas and Propagation*, Vol. AP42, pp. 1549–1553, 1994.
- [9] I.S. Gradshteyn and I.M. Ryzhik, *Tables of Integrals, Series and Products*, Academic Press, New York, 1980.
- [10] M. Abramowitz and I.A. Stegun, *Handbook of Mathematical Functions*, Dover, New York, 1972.
- [11] F.B. Hildebrand, *Finite Difference Equations and Simulations*, Prentice-Hall, Englewood Cliffs, NJ, 1968.

LETTER FROM THE EDITOR

Dear colleagues and friends in the ACES Community.

Sadly, life moves on and there comes a time when we shed some responsibilities and take on new challenges. This will be my last issue of the ACES Journal as Editor-in-Chief. Our very able colleagues Allen Glisson and Ahmed Kishk will be at the helm of the ACES Journal for the next few years.

When I initially accepted the responsibility for the Journal, it was with some trepidation because of possible distance and communications problems. On the whole these fears have proved groundless because of the extensive use made of email and fax. Yes, there have been frustrations. Murphy's law dictates that our email servers must crash whenever a printing deadline is in the offing. Believe me, you really do not want to sit with a 15 January deadline over the peak holiday season in South Africa when everything pretty well grinds to a halt. Incredible as it may seem, of all the hundreds of pieces of mail, only a very few disappeared forever en route to reviewers (fortunately never to authors). Airmail delivery from South Africa to North and South America, Europe and other distant parts has also been known to take up to 6 weeks! I have no idea where the problems lie.

Handing over editorial responsibilities is a drawn-out process. Many of the papers currently in the review cycle will be published under Allen's and Ahmed's stewardship. Hopefully they will benefit as much from my efforts as I did from my predecessor David Stein when I started taking over editorship for the Journal in July/August of 1993. At the outset I had the wholehearted support and guidance of the ACES Editor-in-Chief, Perry Wheless, and also the able assistance and support of Bela Konrad, the Journal's Associate Editor-in-Chief. It has been a particular privilege to be able to work so closely with them over the intervening years.

Inevitably a new broom wants to bring in changes and improvements. The ACES Committee supported the decision to move to the double column compact format. This has resulted in significant savings in publications, and allowed us more flexibility as regards limitations on paper lengths. However, the one thing I had hoped to achieve has eluded me. Hopefully my successors will, with your support, succeed in making the Journal a quarterly publication.

Collating the efforts of authors, editors and reviewers would however be a futile exercise without someone to handle the final publication and distribution, not only of the Journal but also the Newsletter. Here we in ACES are particularly fortunate to have the services of the remarkable husband and wife team, Dick and Pat Adler. Dick of course has been Managing Editor for ACES since its earliest days. Not many of our members are aware of the behind the scenes activities and contributions of these two - and that is as it should be in as well run and smooth an operation as theirs. The reader gets a quality product because Dick and Pat set a high standard. On more than one occasion this has required redoing paste-ups for articles, reprinting the master copy from one of many incompatible wordprocessing formats, and more. Pat and Dick, on behalf of our members and myself, "Many thanks." Without your support I would not have coped.

At the end of this letter, I will again be thanking many of our colleagues who are not on the editorial panel shown in the Journal. I acknowledge their willing support and assistance over the years with a great deal of gratitude. The bulk of the reviews were undertaken by our international panel. I thank them for their assistance, their patience and forbearance, and particularly their time. All our reviewers and editors have heavy professional commitments. That they do find and make time for the reviews is a tribute to their commitment to ACES and its members.

The Guest Editors of the various Special Issues are indeed a Special breed. They have taken on an additional volunteer activity on top of other commitments. For their dedication and many hours of hard work and excellent contributions, I thank them on behalf of all ACES members.

As I have said on more than one occasion, the Journal really belongs to our members, and it is the authors who make it possible. I have no doubt that you will give the new editors your wholehearted support, and I look forward to reading many more fascinating articles covering a wide diversity of interests and applications in the field of computational electromagnetics.

Lastly, it is my pleasure to acknowledge the support of the Department of Electrical and Electronic Engineering at the University of Pretoria. Not only has it provided email, mail and fax facilities, but it has also made available the assistance of two of the administrative staff, Ms. Alet van Zyl, and Ms. Cornel Freislich. Alet and Cornel, my sincere thanks to you both.

Editorship of the ACES Journal has been a stimulating and productive part of my professional career. Thank you for the opportunity to be of service to you, the ACES Member. It's been fun.

Duncan C. Baker
Outgoing Editor-in-Chief, ACES Journal
16 January 1998.

ACKNOWLEDGEMENTS TO REVIEWERS OF PAPERS SUBMITTED TO THE ACES JOURNAL

In addition to our regular international panel of editors listed in the current and previous Journals, I have in the recent past called on the following colleagues for assistance with reviews of papers. Their response has been prompt and positive. On behalf of the ACES members I extend to them our sincere thanks for their important contribution in the essential peer review process. I apologize in advance for any errors and/or omissions.

M.J. Archer, ElectroMagnetic Solutions, United Kingdom
L. Black, Microwave on Line, Boulder, USA
J.R. Brauer, Ansoft Corp., USA
G.J. Burke, Lawrence Livermore National Labs., USA
R.J. Burkholder, Ohio State Univ., USA
K.A. Chamberlin, Univ. of New Hampshire, USA
Q. Chen, Brown Technology Inc., Canada
J.C. Coetzee, Univ. of Pretoria, South Africa
K.R. Davey, American Maglev Techn. Inc. Inc., USA
J.P. Donohoe, Mississippi State Univ., USA
P. Excell, Univ. of Bradford, United Kingdom
P. Goggans, Univ. of Mississippi, USA
M. Green, Univ. of New South Wales, Australia
Huang Yi, Univ. of Liverpool, United Kingdom
J.R. Keradec, Lab. d'Electrotechnique de Grenoble, France
A. Kishk, Univ. of Mississippi, USA
J. Kralovec, Government Aerospace Systems Div., USA
P. Leuchtmann, ETH Zentrum, Switzerland
R. Luebbers, Pennsylvania State Univ., USA
Lu Yilong, Nanyang Technological Univ., Singapore
A. McGovern, Univ. College of Swansea, United Kingdom
P.H.F. Morshuis, Delft Univ. of Technology, Netherlands
A. Orlandi, Univ. of L'Aquila, Italy
R. Perez, Jet Propulsion Labs, USA
M. Piket-May, Univ. of Colorado, USA

K. Richter, Technical Univ. of Graz, Austria
S. Sali, Univ. of Newcastle, United Kingdom
N. Simons, Communications Research Center, Canada
E. Tomer, San Francisco, USA
C. Trueman, Concordia Univ., Canada
F.E. Vermeulen, Univ. of Alberta, Canada
M. Vinokur, Ames Research Center, USA
R.W. Ziolkowski, Univ. of Arizona, USA

1998 INSTITUTIONAL MEMBERS

ANDREW CORPORATION
10500 W. 153rd Street
Orland Park, IL 60462

BIN 293 HIGH PERFORMANCE
PO Box 830702
Birmingham, AL 35283-0702

BOEING NORTH AMERICAN SVCS
1745 Jefferson Davis Hwy
Arlington, VA 22202

BRITISH AEROSPACE
FPC 267 PO Box 5
Filton, BRISTOL, UK BS12 7QW

BRITISH BROADCASTING CO R&D
Kingswood Warren
Tadworth, SURREY, UK KT20 6NP

CAMBRIDGE CONSULTANTS, LTD.
Milton Road, Science Park
Cambridge, CAMBS, UK CB5 4DW

COMMUNICATOR CEC AB
Box 1310
Solna, SWEDEN 17125

CSIRO, CTR FOR ADV. TECH.
PO Box 883
Kenmore, QLD, AUSTRALIA 4069

CULHAM LAB
UK Atomic Energy Authority
Abingdon, OXFORD, UK OX14 3DB

DARTMOUTH COLLEGE
Feldberg Library
Hanover, NH 03755-1809

D.L.R. OBERPFAFFENHOFEN
Zentralbibliothek
Wessling, OBB, GERMANY 8031

DEFENCE TECH & PROCUREMENT
NEMP Lab, AC-Zentrum
Spiez, SWITZERLAND CH 3700

DEFENSE RESEARCH ESTAB. LIB.
3701 Carling Avenue
Ottawa, ON, CANADA K1A 0Z4

DEUTSCHE TELEKOM AG
PO Box 10-00-03
Darmstadt, GERMANY D-64 276

DSTO LIBRARY
Box 1500
Salisbury, SA, AUSTRALIA 5108

E.T.S.E. TELECOMUNICACIONES
Campus Lagoas Marcosende
Vigo, SPAIN 36200

ELECTRONICS RESEARCH INC.
7777 Gardner Road
Chandler, IN 47610-9219

ERA TECHNOLOGY LTD.
Cleve Road
Leatherhead, SURREY, UK KT22 7SA

ERICSSON SAAB AVIONICS AB
Electromagnetic Technology
Linköping, SWEDEN SE 58188

ESCUELA TRANSMISS. EJERCITO
Ctr. Extremadura, KM, 10,200
Madrid, SPAIN 28024

FANFIELD LTD.
Braxted Park
Witham, ESSEX, UK CM8 3XB

FIRSTMARK TECHNOLOGIES
85 St. Charles Quest St.
Longueuil, PQ, CANADA J4H 1C5

FOR-ON-TIME/TECHNION
147-24 176TH Street
Jamaica, NY 11434-5410

GEC MARCONI RES. CTR. LIB.
W. Hanningfield Road, Gt. Baddow
Chelmsford, ESSEX, UK CM2 8HN

HARRIS CORPORATION
1680 University Avenue
Rochester, NY 14610-9983

HARRY-YOUNG PUBLICATIONS
6261 Manchester Blvd.
Buena Park, CA 90621

HKUST, UNIVERSITY LIBRARY
Clear Water Bay Road
Kowloon, HONG KONG

HOKKAIDO DAIGAKU
Nishi 8, Kita 13
Sapporo, JAPAN 060

HUGHES RESEARCH LIBRARY
3011 Malibu Canyon Road
Malibu, CA 90265-4737

HUNTING ENGINEERING LTD.
Reddings Wood, Ampthill
Bedford, UK MK45 2HD

HYDRO-QUEBEC INST. OF RES.
1800 Boul. Lionel-Boulet
Varenes, PQ, CANADA J3X 1S1

IABG MBH, TRM
Einsteinstrasse 20
Ottobrunn, GERMANY D 85521

IIT RESEARCH INSTITUTE
185 Admiral Cochrane Drive
Annapolis, MD 21401-7396

IMAGINEERING LTD.
95 Barber Greene Road, Ste. 112
Toronto, ON, CANADA M3C 3E9

INFORMATION CENTRE
A4 Bldg. Ively Road
Farnborough, HAMPS. UK GU14 0LK

IPS RADIO & SPACE SVC/LIBRARY
PO Box 5606
W. Chatswood, AUSTRALIA 2057

LAVOISIER ABONNEMENTS
14 Rue De Provigny
Cachan, Cedex, FRANCE 94236

LICOSA LIBRARY
Via Duca Di Calabria 1/1
Florence, ITALY 50125

LINDA HALL LIBRARY
5109 Cherry Street
Kansas City, MO 64110-2498

MATRA DEFENSE
37 Av. Louis Breguet Bp 1
Velizy Cedex, FRANCE 78590

METAWAVE COMMUNICATIONS
8700 148th Avenue, N.E.
Redmond, WA 98052

MISSISSIPPI STATE UNIV LIBRARY
PO Box 9570
Mississippi State, MS 39762

MITRE CORPORATION LIBRARY
202 Burlington Road
Bedford, MA 01730-1407

MOD(PE) DGSS
Abbey Wood #54, PO Box 702
Bristol, UK BS12 7DU

MOTOROLA
2001 N. Division Street
Harvard, IL 60033

MYERS ENGINEERING INTL, INC.
PO Box 15908, 5425 NW 24th St.
Margate, FL 33063

NATL RADIOLOGICAL PROT. BD.
Chilton
Didcot, OXON, UK OX11 0RG

NAVAL RESEARCH LABORATORY
C. Office
Washington, DC 20375

NGIC
220 7th Street, NE
Charlottesville, VA 22902-5396

NIKSAR
35/45 Gilbey Road
Mt. Waverley, VIC, AUSTRALIA 3149

NNR AIR CARGO SERVICE
Hook Creed Blvd. & 145th Avenue
Valley Stream, NY 11581

NORTEL TECHNOLOGY
London Road
Harlow, ESSEX, UK CM17 9NA

NTT WIRELESS SYSTEMS LABS.
1-1 Hikarinooka Yokosuka-Shi
Kanagawa, JAPAN239

PENN STATE UNIV LIBRARY
Pattee Library
University Park, PA 16802

PHILIPS RESEARCH LAB LIBRARY
Cross Oak Lane, Salfords
Redhill, SURREY. UKRH1 5HA

PHILIPS RESEARCH
Prof. Holstlaan 4
Eindhoven, NETHERLANDS 11172j

QUEEN MARY & WESTFIELD COLL
Mile End Road
London, UK E1 4NS

RAND AFRIKAANS UNIVERSITY
PO Box 524, Aucklandpark
Johannesburg, S AFRICA 2006

RAYTHEON E-SYSTEMS
PO Box 6056
Greenville, TX 75403

SONY CORPORATION
174 Fujitsukacho, Hodogaya Ku
Yokohama MZ, JAPAN 240

SOUTHWEST RESEARCH INST.
6220 Culebra Road
San Antonio, TX 78238

SWETS SUBSCRIPTION SERVICE
440 Creamery Way, Suite A
Exton, PA 19341

TAMPERE UNIVERSITY OF TECH
PO Box 692
Tampere, FINLAND 33101

TASC - LIBRARY
55 Walkers Brook Drive
Reading, MA 01867-3297

TECHNISCHE UNIV. DELFT
Mekelweg 4, Delft
HOLLAND, NETHERLANDS 2628 CD

TELEBRAS - CPQD, LIB.
Rod. Campinas
Campinas, SP BRAZIL 13088-061

TELSTRA LIBRARY
Private Bag 37
Clayton, VIC, AUSTRALIA 3168

TELSTRA RESEARCH LABS
770 Blackburn Road
Clayton, VIC, AUSTRALIA 3168

UNIV OF CENTRAL FLORIDA LIB.
PO Box 162440
Orlando, FL 32816-2440

UNIV OF COLORADO LIBRARY
Campus Box 184
Boulder, CO 80309-0184

UNIV OF MISSOURI-ROLLA LIB.
1870 Miner Circle
Rolla, MO 65409-0001

UNIVERSITAT DER BUNDESWEHR
Werner Heisenberg Weg 39
Neubiberg, GERMANY D-85577

US COAST GUARD ACADEMY
15 Mohegan Avenue
New London, CT 06320-4195

VECTOR FIELDS LTD.
24 Bankside Kidlington
Oxford, UK OX5 1JE

VIT, TECHNICAL RESEARCH. CTR.
PO Box 1202
Espoo, FINLAND FIN-02044

ACES COPYRIGHT FORM

This form is intended for original, previously unpublished manuscripts submitted to ACES periodicals and conference publications. The signed form, appropriately completed, MUST ACCOMPANY any paper in order to be published by ACES. PLEASE READ REVERSE SIDE OF THIS FORM FOR FURTHER DETAILS.

TITLE OF PAPER:

AUTHORS(S)

PUBLICATION TITLE/DATE:

RETURN FORM TO:

Dr. Richard W. Adler
Naval Postgraduate School
Code EC/AB
833 Dyer Road, Room 437
Monterey, CA 93943-5121 USA

PART A - COPYRIGHT TRANSFER FORM

(NOTE: Company or other forms may not be substituted for this form. U.S. Government employees whose work is not subject to copyright may so certify by signing Part B below. Authors whose work is subject to Crown Copyright may sign Part C overleaf).

The undersigned, desiring to publish the above paper in a publication of ACES, hereby transfer their copyrights in the above paper to The Applied Computational Electromagnetics Society (ACES). The undersigned hereby represents and warrants that the paper is original and that he/she is the author of the paper or otherwise has the power and authority to make and execute this assignment.

Returned Rights: In return for these rights, ACES hereby grants to the above authors, and the employers for whom the work was performed, royalty-free permission to:

1. Retain all proprietary rights other than copyright, such as patent rights.
2. Reuse all or portions of the above paper in other works.
3. Reproduce, or have reproduced, the above paper for the author's personal use or for internal company use provided that (a) the source and ACES copyright are indicated, (b) the copies are not used in a way that implies ACES endorsement of a product or service of an employer, and (c) the copies per se are not offered for sale.
4. Make limited distribution of all or portions of the above paper prior to publication.
5. In the case of work performed under U.S. Government contract, ACES grants the U.S. Government royalty-free permission to reproduce all or portions of the above paper, and to authorize others to do so, for U.S. Government purposes only.

ACES Obligations: In exercising its rights under copyright, ACES will make all reasonable efforts to act in the interests of the authors and employers as well as in its own interest. In particular, ACES REQUIRES that:

1. The consent of the first-named author be sought as a condition in granting re-publication permission to others.
2. The consent of the undersigned employer be obtained as a condition in granting permission to others to reuse all or portions of the paper for promotion or marketing purposes.

In the event the above paper is not accepted and published by ACES or is withdrawn by the author(s) before acceptance by ACES, this agreement becomes null and void.

AUTHORIZED SIGNATURE

TITLE (IF NOT AUTHOR)

EMPLOYER FOR WHOM WORK WAS PERFORMED

DATE FORM SIGNED

PART B - U.S. GOVERNMENT EMPLOYEE CERTIFICATION

(NOTE: If your work was performed under Government contract but you are not a Government employee, sign transfer form above and see item 5 under Returned Rights).

This certifies that all authors of the above paper are employees of the U.S. Government and performed this work as part of their employment and that the paper is therefore not subject to U.S. copyright protection.

AUTHORIZED SIGNATURE

TITLE (IF NOT AUTHOR)

NAME OF GOVERNMENT ORGANIZATION

DATE FORM SIGNED

PART C - CROWN COPYRIGHT

(Note: ACES recognizes and will honor Crown Copyright as it does U.S. Copyright. It is understood that, in asserting Crown Copyright, ACES in no way diminishes its rights as publisher. Sign only if ALL authors are subject to Crown Copyright.

This certifies that all authors of the above Paper are subject to Crown Copyright. (Appropriate documentation and instructions regarding form of Crown Copyright notice may be attached).

AUTHORIZED SIGNATURE

TITLE OF SIGNED

NAME OF GOVERNMENT BRANCH

DATE FORM SIGNED

Information to Authors

ACES POLICY

ACES distributes its technical publications throughout the world, and it may be necessary to translate and abstract its publications, and articles contained therein, for inclusion in various compendiums and similar publications, etc. When an article is submitted for publication by ACES, acceptance of the article implies that ACES has the rights to do all of the things it normally does with such an article.

In connection with its publishing activities, it is the policy of ACES to own the copyrights in its technical publications, and to the contributions contained therein, in order to protect the interests of ACES, its authors and their employers, and at the same time to facilitate the appropriate re-use of this material by others.

The new United States copyright law requires that the transfer of copyrights in each contribution from the author to ACES be confirmed in writing. It is therefore necessary that you execute either Part A-Copyright Transfer Form or Part B-U.S. Government Employee Certification or Part C-Crown Copyright on this sheet and return it to the Managing Editor (or person who supplied this sheet) as promptly as possible.

CLEARANCE OF PAPERS

ACES must of necessity assume that materials presented at its meetings or submitted to its publications is properly available for general dissemination to the audiences these activities are organized to serve. It is the responsibility of the authors, not ACES, to determine whether disclosure of their material requires the prior consent of other parties and if so, to obtain it. Furthermore, ACES must assume that, if an author uses within his/her article previously published and/or copyrighted material that permission has been obtained for such use and that any required credit lines, copyright notices, etc. are duly noted.

AUTHOR/COMPANY RIGHTS

If you are employed and you prepared your paper as a part of your job, the rights to your paper initially rest with your employer. In that case, when you sign the copyright form, we assume you are authorized to do so by your employer and that your employer has consented to all of the terms and conditions of this form. If not, it should be signed by someone so authorized.

NOTE RE RETURNED RIGHTS: Just as ACES now requires a signed copyright transfer form in order to do "business as usual", it is the intent of this form to return rights to the author and employer so that they too may do "business as usual". If further clarification is required, please contact: The Managing Editor, R.W. Adler, Naval Postgraduate School, Code EC/AB, Monterey, CA, 93943, USA (408)656-2352.

Please note that, although authors are permitted to re-use all or portions of their ACES copyrighted material in other works, this does not include granting third party requests for reprinting, republishing, or other types of re-use.

JOINT AUTHORSHIP

For jointly authored papers, only one signature is required, but we assume all authors have been advised and have consented to the terms of this form.

U.S. GOVERNMENT EMPLOYEES

Authors who are U.S. Government employees are not required to sign the Copyright Transfer Form (Part A), but any co-authors outside the Government are.

Part B of the form is to be used instead of Part A only if all authors are U.S. Government employees and prepared the paper as part of their job.

NOTE RE GOVERNMENT CONTRACT WORK: Authors whose work was performed under a U.S Government contract but who are not Government employees are required to sign Part A-Copyright Transfer Form. However, item 5 of the form returns reproduction rights to the U.S. Government when required, even though ACES copyright policy is in effect with respect to the reuse of material by the general public.

March 1998

ACES MEMBERSHIP - NEWSLETTER & JOURNAL SUBSCRIPTION FORM

please print

FIRST NAME

MIDDLE INTIAL

DEPARTMENT/MAIL STATION

PLEASE LIST THE ADDRESS YOU WANT USED FOR PUBLICATIONS

MAILING ADDRESS**PROVINCE/STATE****COUNTRY**

ZIP/POSTAL CODE

FAX

AMATEUR RADIO CALL SIGN

E-MAIL ADDRESS CAN BE INCLUDED IN ACES DATABASE

☐ **YES**☐ NO

PERMISSION IS GRANTED TO HAVE MY NAME PLACED ON MAILING LISTS WHICH MAY BE SOLD

☐ YES☐ NO

CURRENT SUBSCRIPTION PRICES

AREA	INDIVIDUAL SURFACE MAIL	INDIVIDUAL AIRMAIL	ORGANIZATIONAL (AIRMAIL ONLY)
U.S. & CANADA	() \$ 65	() \$ 65	() \$115
MEXICO, CENTRAL & SOUTH AMERICA	() \$ 68	() \$ 70	() \$115
EUROPE, FORMER USSR TURKEY, SCANDINAVIA	() \$ 68	() \$ 78	() \$115
ASIA, AFRICA, MIDDLE EAST & PACIFIC RIM	() \$ 68	() \$ 85	() \$115

FULL-TIME STUDENT/RETIRED/UNEMPLOYED RATE IS \$25 FOR ALL COUNTRIES

CREDIT CARD USERS

IF YOU ARE PAYING BY CREDIT CARD & CARD IS YOUR OWN, YOU MUST, (1) PRINT AND SIGN YOUR NAME BELOW; (2) MAKE SURE YOUR COMPLETE ADDRESS IS LISTED ABOVE. * IF THE CARD YOU ARE USING IS NOT YOUR CARD, THE CARD HOLDER MUST, (3) PRINT AND SIGN HIS/HER NAME AND, (4) ENTER HIS/HER COMPLETE ADDRESS BELOW.

PRINT FIRST AND LAST NAME OF CARD HOLDER

SIGNATURE OF CARD HOLDER

MAILING ADDRESS

MAILING ADDRESS (cont)

METHOD OF PAYMENT

- ☐ A bank check for the total amount is enclosed.⁽¹⁾
- ☐ Traveler's checks for the total amount are enclosed.⁽²⁾
- ☐ International Money Order is enclosed.⁽³⁾
- ☐ Charge to: ☐ MasterCard ☐ Visa. ☐ Discover ☐ Amex.⁽⁴⁾

Card
No.

[illegible]**Card Exp. Date:**

Mo. _____ Year _____

**MAKE CHECKS PAYABLE TO "ACES" and send to: RICHARD W. ADLER, EXEC. OFFICER,
NAVAL POSTGRADUATE SCHOOL, ECE DEPT., CODE EC/AB, 833 DYER ROAD, ROOM 437, MONTEREY, CA 93943-5121**

Visit us on line at: www.emclab.umr.edu/aces

Non-USA participants: Prices are in U.S. dollars. All currencies must be converted to U.S. dollars, payable by banks with U.S. affiliates. (1) **Bank Checks**, (2) **Traveler's Checks** (in U.S. \$); (3) **International Money Order** drawn in U.S. funds, payable in U.S.; (4) **Credit Cards**: Visa, Master Card, Discover Card, and Amex.

ADVERTISING RATES

	FEE	PRINTED SIZE
Full page	\$200.	7.5" x 10.0"
1/2 page	\$100.	7.5" x 4.7" or 3.5" x 10.0"
1/4 page	\$ 50	3.5" x 4.7"

All ads must be camera ready copy.

Ad deadlines are same as Newsletter copy deadlines.

Place ads with Ray Perez, Newsletter Editor, Martin Marietta Astronautics,
MS 58700, PO Box 179, Denver, CO 80201, USA. The editor reserves the right to
reject ads.

ACES NEWSLETTER AND JOURNAL COPY INFORMATION

<u>Issue</u>	<u>Copy Deadline</u>
March	January 13
July	May 25
November	September 25

APPLIED COMPUTATIONAL ELECTROMAGNETICS SOCIETY JOURNAL

INFORMATION FOR AUTHORS

PUBLICATION CRITERIA

Each paper is required to manifest some relation to applied computational electromagnetics. **Papers may address general issues in applied computational electromagnetics, or they may focus on specific applications, techniques, codes, or computational issues.** While the following list is not exhaustive, each paper will generally relate to at least one of these areas:

1. Code validation. This is done using internal checks or experimental, analytical or other computational data. Measured data of potential utility to code validation efforts will also be considered for publication.

2. Code performance analysis. This usually involves identification of numerical accuracy or other limitations, solution convergence, numerical and physical modeling error, and parameter tradeoffs. However, it is also permissible to address issues such as ease-of-use, set-up time, run time, special outputs, or other special features.

3. Computational studies of basic physics. This involves using a code, algorithm, or computational technique to simulate reality in such a way that better or new physical insight or understanding is achieved.

4. New computational techniques, or new applications for existing computational techniques or codes.

5. "Tricks of the trade" in selecting and applying codes and techniques.

6. New codes, algorithms, code enhancement, and code fixes. This category is self-explanatory but includes significant changes to existing codes, such as applicability extensions, algorithm optimization, problem correction, limitation removal, or other performance improvement. **Note: Code (or algorithm) capability descriptions are not acceptable, unless they contain sufficient technical material to justify consideration.**

7. Code input/output issues. This normally involves innovations in input (such as input geometry standardization, automatic mesh generation, or computer-aided design) or in output (whether it be tabular, graphical, statistical, Fourier-transformed, or otherwise signal-processed). Material dealing with input/output database management, output interpretation, or other input/output issues will also be considered for publication.

8. Computer hardware issues. This is the category for analysis of hardware capabilities and limitations in meeting

various types of electromagnetics computational requirements. Vector and parallel computational techniques and implementation are of particular interest.

Applications of interest include, but are not limited to, antennas (and their electromagnetic environments), networks, static fields, radar cross section, shielding, radiation hazards, biological effects, electromagnetic pulse (EMP), electromagnetic interference (EMI), electromagnetic compatibility (EMC), power transmission, charge transport, dielectric and magnetic materials, microwave components, MMIC technology, remote sensing and geophysics, communications systems, fiber optics, plasmas, particle accelerators, generators and motors, electromagnetic wave propagation, non-destructive evaluation, eddy currents, and inverse scattering.

Techniques of interest include frequency-domain and time-domain techniques, integral equation and differential equation techniques, diffraction theories, physical optics, moment methods, finite differences and finite element techniques, modal expansions, perturbation methods, and hybrid methods. This list is not exhaustive.

A unique feature of the Journal is the publication of unsuccessful efforts in applied computational electromagnetics. Publication of such material provides a means to discuss problem areas in electromagnetic modeling. Material representing an unsuccessful application or negative results in computational electromagnetics will be considered for publication only if a reasonable expectation of success (and a reasonable effort) are reflected. Moreover, such material must represent a problem area of potential interest to the ACES membership.

Where possible and appropriate, authors are required to provide statements of quantitative accuracy for measured and/or computed data. This issue is discussed in "Accuracy & Publication: Requiring quantitative accuracy statements to accompany data", by E.K. Miller, *ACES Newsletter*, Vol. 9, No. 3, pp. 23-29, 1994, ISBN 1056-9170.

EDITORIAL REVIEW

In order to ensure an appropriate level of quality control, papers are refereed. They are reviewed both for technical correctness and for adherence to the listed guidelines regarding information content. Authors should submit the initial manuscript in draft form so that any suggested changes can be made before the photo-ready copy is prepared for publication.

STYLE FOR CAMERA-READY COPY

The ACES Journal is flexible, within reason, in regard to style. However, certain requirements are in effect:

1. The paper title should NOT be placed on a separate page. The title, author(s), abstract, and (space permitting) beginning of the paper itself should all be on the first page. The title, author(s), and author affiliations should be centered (center-justified) on the first page.
2. An abstract is REQUIRED. The abstract should state the computer codes, computational techniques, and applications discussed in the paper (as applicable) and should otherwise be usable by technical abstracting and indexing services.
3. Either British English or American English spellings may be used, provided that each word is spelled consistently throughout the paper.
4. Any commonly-accepted format for referencing is permitted, provided that internal consistency of format is maintained. As a guideline for authors who have no other preference, we recommend that references be given by author(s) name and year in the body of the paper (with alphabetical listing of all references at the end of the paper). Titles of Journals, monographs, and similar publications should be in boldface or italic font or should be underlined. Titles of papers or articles should be in quotation marks.
5. Internal consistency shall also be maintained for other elements of style, such as equation numbering. As a guideline for authors who have no other preference, we suggest that equation numbers be placed in parentheses at the right column margin.
6. The intent and meaning of all text must be clear. For authors who are NOT masters of the English language, the ACES Editorial Staff will provide assistance with grammar (subject to clarity of intent and meaning).
7. Unused space should be minimized. Sections and subsections should not normally begin on a new page.

MATERIAL, SUBMITTAL FORMAT AND PROCEDURE

The preferred format for submission and subsequent review, is 12 point font or 12 cpi, double line spacing and single column per page. Four copies of all submissions should be sent to the Editor-in-Chief (see inside front cover). Each submission must be accompanied by a covering letter. The letter should include the name, address, and telephone and/or fax number and/or e-mail address of at least one of the authors.

Only camera-ready original copies are accepted for publication. The term "**camera-ready**" means that the **material is neat, legible, and reproducible**. The preferred font style is Times Roman 10 point (or equivalent) such as that used in this text. A double column format similar to that used here is preferred. **No author's work will be turned down once it has been accepted because of an inability to meet the requirements concerning fonts and format.** Full details are sent to the author(s) with the letter of acceptance.

There is NO requirement for India ink or for special paper; any plain white paper may be used. However, faded lines on figures and white streaks along fold lines should be avoided. Original figures - even paste-ups - are preferred over "nth-generation" photocopies. These original figures will be returned if you so request.

While ACES reserves the right to re-type any submitted material, this is not generally done.

PUBLICATION CHARGES

ACES members are allowed 12 pages per paper without charge; non-members are allowed 8 pages per paper without charge. Mandatory page charges of \$75 a page apply to all pages in excess of 12 for members or 8 for non-members. Voluntary page charges are requested for the free (12 or 8) pages, but are NOT mandatory or required for publication. A priority courtesy guideline, which favors members, applies to paper backlogs. Full details are available from the Editor-in-Chief.

COPYRIGHTS AND RELEASES

Each primary author must sign a copyright form and obtain a release from his/her organization vesting the copyright with ACES. Forms will be provided by ACES. Both the author and his/her organization are allowed to use the copyrighted material freely for their own private purposes.

Permission is granted to quote short passages and reproduce figures and tables from an ACES Journal issue provided the source is cited. Copies of ACES Journal articles may be made in accordance with usage permitted by Sections 107 or 108 of the U.S. Copyright Law. This consent does not extend to other kinds of copying, such as for general distribution, for advertising or promotional purposes, for creating new collective works, or for resale. The reproduction of multiple copies and the use of articles or extracts for commercial purposes require the consent of the author and specific permission from ACES. Institutional members are allowed to copy any ACES Journal issue for their internal distribution only.